# Tuned Inerter Damper and Energy Converter for Enhanced Semi-submersible Offshore Wind Turbine

***Final Report***
**Deliverable 5.2**

Prepared for:

**National Offshore Wind Research and Development Consortium**

Mel Schultz, Project Manager

Prepared by:

**Virginia Tech**

Blacksburg, VA

Lei Zuo
Professor Department of Naval Architecture and Marine Engineering, University of Michigan

Oumar Barry
Associate Professor Department of Mechanical Engineering, Virginia Tech

Biao Fang
Principal Engineer, GE Global Research

# Abstract

This report investigates a passive structural-control approach to reduce motions and loads on a semisubmersible floating offshore wind turbine and to modestly harvest wave-induced energy. We consider tuned mass dampers (TMDs) and tuned-inerter dampers (TIDs), with one device installed in each of the three outer columns. The technical program integrates (i) high-fidelity aero-hydro-servo-elastic simulations in OpenFAST using the OC4 DeepCwind platform as the baseline, (ii) a reduced-order model (ROM) for rapid design-space exploration and optimization, and (iii) a 1:50-scale wave-tank campaign evaluating TMD configurations and the enabling spring-and-guide hardware.

Across free-decay and wave excitation cases, both TMD and TID reduce platform heave and pitch relative to the baseline. Near the platform's pitch natural frequency (≈0.2638 Hz), the "natural-frequency tuned" configuration produces the largest attenuation; a "wave-frequency tuned" configuration centered at ≈0.6487 Hz delivers additional reduction around the dominant incident-wave energy. Representative steady-state amplitude reductions of ≈10–30% (natural-frequency tuned) and ≈20–30% (wave-frequency tuned) are demonstrated. Scaled tests confirm the feasibility of low-friction, compliant spring-and-guide mechanisms needed to achieve very low target frequencies.

A techno-economic assessment projects a net LCOE reduction of ~7.8% for a 15-MW semisubmersible when three column-mounted absorbers are deployed, driven primarily by AEP gain (~+4.2%) from reduced pitch motion and by maintenance savings associated with lower fatigue demand. Simulated electrical output from TIDs is modest (order-tens of kilowatts; ~27 kW in the 15-MW case) and not the main value driver. A two-year New Technology Introduction (NTI) plan is outlined, culminating in a full-scale prototype to de-risk compliant springs, guidance, and drivetrain options and to validate performance under integrated wind-wave operation.

# Keywords

Floating offshore wind turbine; Semi-submersible platform; Tuned Mass Damper (TMD); Tuned Inerter Damper (TID); OpenFAST; Wave tank testing; Reduced-order model (ROM); Levelized cost of energy (LCOE).

# Acknowledgements and Disclaimers

This material is based upon work supported by the U.S. Department of Energy's Office of Energy Efficiency and Renewable Energy ("EERE") under the Wind Energy Technologies Office Award Number DE-EE0008390 and by Virginia Commonwealth, through NYSERDA/NOWRDC Project #123/154631.

This report was prepared as an account of work sponsored by an agency of the United States Government, NYSERDA and NOWRDC. Neither the United States Government nor any agency thereof, NYSERDA or NOWRDC nor any of their employees, makes any warranty, express or implied, or assumes any legal liability or responsibility for the accuracy, completeness, or usefulness of any information, apparatus, product, or process disclosed, or represents that its use would not infringe privately owned rights. Reference herein to any specific commercial product, process, or service by trade name, trademark, manufacturer, or otherwise does not necessarily constitute or imply its endorsement, recommendation, or favoring by the United States Government or any agency thereof, NYSERDA or NOWRDC. The views and opinions of authors expressed herein do not necessarily state or reflect those of the United States Government or any agency thereof, NYSERDA or NOWRDC.

# Table of Contents


**1 Background and Introduction ..... 11**

1.1 Offshore Wind: Fixed and Floating Foundation ..... 11

1.2 Dynamics and Loads on Floating Platform ..... 13

1.3 Structural Control for Floating Wind Turbines ..... 13

1.4 Project Approach ..... 14

**2 Offshore Wind Platform Aero-Hydro-Structure Modeling ..... 15**

2.1 High Fidelity Modeling using OpenFAST ..... 15

2.1.1 Modeling Framework and Scope ..... 15

2.1.2 Baseline Model Configuration ..... 16

2.1.3 Structural-Control Formulation in OpenFAST ..... 17

2.1.4 Tuned Mass Dampers (TMDs) in OpenFAST ..... 17

2.1.5 Tuned-Inerter Damper (TID) Integration ..... 19

2.1.6 State-Space Implementation and Outputs ..... 20

2.1.7 Model Validation and Results ..... 20

2.2 Reduced-Order Modeling for Design Optimization ..... 26

2.2.1 Modeling Framework and Scope ..... 26

2.2.2 Calibrating and Verifying the ROM ..... 28

2.2.3 Optimization Overview ..... 30

2.2.4 Free Decay Optimization ..... 31

2.2.5 Regular Wave Optimization and Irregular Wave Analysis ..... 33

**3 Critical Component Validation and Scaled Prototype Wave Tank Testing ..... 35**

3.1 Scaled Semi-submersible Floating Platform ..... 35

3.2 Tuned Mass Damper (TMD) System ..... 35

3.2.1 Critical Components Validation ..... 36

3.3 Scaled Prototype Tank Test ..... 42

3.3.1 Modular Ballasting System ..... 43

3.3.2 Turbine Simulation ..... 45

3.3.3 Mooring System Design ..... 45

3.3.4 Instrumentation ..... 48
3.3.5 Test Matrix ..... 49
3.3.6 Wave Tank Test Results ..... 50
3.3.7 Power Output Considerations of TIDs ..... 57
**4 Techno-Economic Analysis and New Technology Introduction Plan ..... 58**
4.1 Techno-Economic Analysis ..... 58
4.1.1 Scope and Baseline ..... 58
4.1.2 Market Benchmark and LCOE Target ..... 58
4.1.3 Impact on Annual Energy Production (AEP) ..... 60
4.1.4 Impact on Capital and Operating Costs ..... 61
4.1.5 LCOE Outcome ..... 61
4.2 New Technology Introduction Plan ..... 62
4.2.1 Overview of NTI Process ..... 62
4.2.2 Technology Evaluation ..... 63
4.2.3 Risks and Mitigation ..... 68
4.2.4 Sustainability ..... 71
4.2.5 NTI Focus ..... 72
**5 Concluding Remarks ..... 74**
**6 References ..... 76**
**7 Appendix A ..... 78**
7.1 Nonlinear Tuned Inerter Damper (TID) ..... 78
7.2 MMR Mechanism and Engagement ..... 78
7.3 Models ..... 79
7.4 Wave Excitation ..... 80
7.5 Key Results ..... 81

# List of Figures

Figure 1: Growth of the offshore floating wind market through 2027[1]. ....11
Figure 2: Wind resource for the U.S. at 100 m above surface level [1]....12
Figure 3: Different fixed and floating foundation designs, deployed depending on water depths [3]. ....12
Figure 4: Sea to land ratios of ultimate loads for the different floating platform concepts [4]....13
Figure 5: Diagram of a simple TMD [12]....14
Figure 6: Different TID configurations [12]. ....14
Figure 7: Diagram of the OpenFAST modular framework [21]....15
Figure 8: Diagram of the OC4 semisubmersible floating system used as the baseline model for this project [22]. ....16
Figure 9: Diagram of the body-fixed reference frames and position vectors used to define the TMD position in OpenFAST [23]. ....18
Figure 10 Diagram of the Tuned Inerter Damper with labeled system parameters: masses, spring stiffness, and damping coefficients. ....19
Figure 11: (a) Time domain results for the heave free decay test at an 8% mass ratio; (b) Frequency domain results for the heave free decay test at an 8% mass ratio [23]....21
Figure 12: (a) Time domain results for the pitch free decay test at an 8% mass ratio; (b) Frequency domain results for the pitch free decay test at an 8% mass ratio [23]....22
Figure 13: Time domain results for the (a) 2%; (b) 5%; (c) 8% mass ratio cases for the TMD and TID compared to the baseline pitch free decay test. Frequency domain results for the (d) 2%; (e) 5%; (f) 8% mass ratio cases for the baseline, TMD, and TID pitch free decay test [23]....24
Figure 14: Time domain results for the baseline, TMD, and TID using a mass ratio of 3% with a JONSWAP wave with a period of 10 seconds and height of 3 meters [23]....25
Figure 15: Frequency domain results for the baseline, TMD, and TID using a mass ratio of 3% with a JONSWAP wave with a period of 10 seconds and height of 3 meters [23]....25
Figure 16: Baseline platform with no structural control. ....26
Figure 17: Diagrams of the structural control methods (absorbers) implemented into the platform. ....27
Figure 18: Diagram of the semisubmersible platform with (a) TMDs; (b) TIDs [12]. ....28
Figure 19: Snapshots of the WEC-Sim TMD model used to verify the TMD model [12]. ....29
Figure 20: Free decay test comparison between WEC-Sim and the derived model for the baseline configuration [12]. ....29
Figure 21: Free decay test comparison between WEC-Sim and the derived model for the TMD configuration [12]. ....30
Figure 22: Surfaces showing the objective function of the free decay optimizations as a function of the design parameters [12]....31
Figure 23: Optimized free decay time domain response for the overall system with a mass ratio of 5% [12]. ....31
Figure 24: Optimized free decay frequency domain response for the overall system with a mass ratio of 5% [12]....32
Figure 25: Percent reduction vs. mass ratio for both heave and pitch free decay optimization studies [12]. ....32
Figure 26: Optimized heave and pitch time domain response for a representative sea state, using a mass ratio of 3% [12]. ....34

Figure 27: Optimized heave and pitch frequency domain response for a representative sea state, using a mass ratio of 3% [12]. ....34
Figure 28: Pitch time domain response for a representative irregular wave case, using a mass ratio of 3%, ran for an extended period [12]. ....34
Figure 29: Tested 1:50 OC4-DeepCwind semi-submersible floating wind turbine....35
Figure 30: The Tuned Mass Damper (TMD) module designed for platform stabilization. ....36
Figure 31: Compliant mechanism with four inclined fixed-guided beams [25] ....37
Figure 32: CBCM divides the beam into N elements at points O2-ON [26], [27] ....38
Figure 33: Parameter extraction for compliant fixed-guided beams from literature used for validation of the CBCM solver [28] ....38
Figure 34. Comparison of force-displacement results from the CBCM solver against reference literature [28] ....39
Figure 35. Summary of extracted beam parameters for the second fixed-guided beam example from literature [29] ....39
Figure 36. Validation of CBCM solver against reference literature for the second fixed-guided beam example [29] ....39
Figure 37: Optimized force-displacement curve (blue) of the fixed-guided beams compared to the target stiffness curve (green). ....40
Figure 38: Deformation shape of the optimized beam at different displacements. ....41
Figure 39: Deformation profile and elemental stress distribution in the optimized beam. ....42
Figure 40: Schematic for the Davidson laboratory high speed towing tank [30]. ....43
Figure 41: Modular Ballasting System (yellow) and the tuned mass dampers assembly. ....44
Figure 42: Calibrated electric duct fan thrust with respect to the pulse width modulation input. ....45
Figure 43: Evaluation of equivalent mooring line stiffness and mooring angles at the platform's static equilibrium position. ....46
Figure 44: Mechanism of the pulley-guided taut mooring setup with helical spring, used to simulate catenary mooring stiffness behavior [31]. ....47
Figure 45: 4 OptiTrack motion tracking camera and their corresponding camera view. ....48
Figure 46: Fast Fourier transform of the platform pitch free decay. ....50
Figure 47: Two TMD sets to be installed in the pontoon bays: *left, 3 units tuned to the dominant wave frequency (~0.6487 Hz) with a single compliant layer; right, 3 units tuned to the heave natural frequency (~0.3922 Hz) using three compliant layers in series. ....51
Figure 48: Natural-frequency–tuned TMDs (~0.3922 Hz): optimized force–displacement, apparent stiffness, and inferred tuned frequency vs. stroke, achieved with three compliant spring layers to meet low-frequency, stress, and envelope constraints. ....52
Figure 49: Wave-frequency–tuned TMDs (~0.6487 Hz): optimized force–displacement, apparent stiffness, and inferred tuned frequency vs. stroke, achieved with a single compliant spring layer within the same envelope. ....52
Figure 50: Platform pitch RAO under regular waves—baseline vs. TMD configurations. The natural-frequency–tuned set yields ≈10–30% amplitude reduction near 0.2638 Hz; the wave-frequency–tuned set yields ≈20–30% reduction near ~0.6487 Hz. ....53
Figure 51: Natural-frequency–tuned configuration: platform pitch amplitude and TMD stroke amplitudes vs. excitation frequency. Device strokes peak near 0.2638 Hz, coincident with the primary attenuation band. ....54

Figure 52: Wave-frequency–tuned configuration: platform pitch amplitude and TMD stroke amplitudes vs. excitation frequency. Device strokes peak near ~0.6487 Hz, coincident with the secondary attenuation band. ..... 55
Figure 53: Platform pitch—time-domain response in an extreme sea state. Comparison of baseline (TMD locked), TMD tuned to platform pitch natural frequency, and TMD tuned to dominant wave frequency. ..... 56
Figure 54: Platform pitch—time-domain response in an operational sea state. Comparison of baseline (TMD locked), TMD tuned to platform pitch natural frequency, and TMD tuned to dominant wave frequency ..... 56
Figure 55: Power generation of TIDs in a full-scale OC4 semi-submersible platform under 10 s period of irregular wave excitation. ..... 57
Figure 56: Applying TID to a semi-submersible floating wind turbine ..... 58
Figure 57: LCOE breakdown reported by NREL [32]. ..... 59
Figure 58: Floating wind cost reported in [33]. ..... 59
Figure 59: Impact of Floating Platform on Power Curves in [34]. ..... 60
Figure 60: Refined LCOE Flowdown. ..... 62
Figure 61: NTI Timeline and Key Milestones ..... 63
Figure 62: Passive MMR [35]. ..... 64
Figure 63: Schematic of a planetary gear. ..... 65
Figure 64: Schematic of force acting on sun gear/planetary gear. ..... 66
Figure 65: Cost Comparison for Each Column ..... 68
Figure 66: TMD design for 1:50 OC4 semisubmersible floating platform. ..... 70
Figure 67: TMD mass and guiding system in wave tank test. ..... 71
Figure 68: Mechanism of nonlinear TID with alternative types of inerter-spring-damper (W(s)) layout shown in (a) – (c) [36]. ..... 78
Figure 69: 2-D concept diagram of a) Linear TID and Engaged Nonlinear TID and b) Disengaged Nonlinear TID within Center Column of Semi-Submersible[36]. ..... 79
Figure 70: Full semi-submersible model with three nonlinear TIDs [36]. ..... 80
Figure 71: Frequency domain plot for irregular wave (10 s period) with vibration damper tuned to wave frequency [36]. ..... 81

# List of Tables

Table 1: Optimized values from the parametric study to minimize the impact of pitch motion for the pitch free decay test [23]. ..... 23
Table 2: Optimized values from the parametric study to minimize the impact of pitch motion for the JONSWAP wave spectrum [23]. ..... 23
Table 3: Results for pitch free decay test [23]. ..... 24
Table 4: Results of the heave and pitch free decay optimizations for baseline and control configurations [12]. ..... 33
Table 5: Key Parameters and Scaling for the 1:50 OC4 Model. ..... 44
Table 6: Overview of wave conditions: regular waves for RAO analysis and irregular waves for design and operational load cases. ..... 49
Table 7: TID Power and Torque ..... 63
Table 8: Drivetrain Mass and Cost Comparison ..... 68

# Acronyms and Abbreviations

| | |
|---|---|
| AEP | Annual Energy Production |
| BEM | Boundary Element Method |
| CapEX | Capital Expenditure |
| CBCM | Chained Beam-Constraint Model |
| CM | Center of Mass |
| CF | Capacity Factor |
| DAQ | Data Acquisition |
| DEL | Damage Equivalent Load |
| DOF | Degrees of Freedom |
| FOWT | Floating Offshore Wind Turbine |
| GA | Genetic Algorithm |
| GE | General Electric |
| JONSWAP | Joint North Sea Wave Project |
| LCOE | Levelized Cost of Electricity |
| MMR | Mechanical Motion Rectifier |
| NPI | New Product Introduction |
| NREL | National Renewable Energy Laboratory |
| NTI | New Technology Introduction |
| OC4 | Offshore Code Comparison Collaboration, Phase IV (OC4) |
| OD | Outer Diameter |
| OpEX | Operation Expenditure |
| RAO | Response Amplitude Operator |
| RMS | Root Mean Square |
| ROM | Reduced-Order Model |
| StC | Structural Control |
| SWL | Still Water Level |
| TID | Tuned Inerter Damper |
| TMD | Tuned Mass Damper |
| UMaine | University of Maine |
| VT | Virginia Tech |
| WEC-Sim | Wave Energy Converter Simulator |

# 1 Background and Introduction

## 1.1 Offshore Wind: Fixed and Floating Foundation

Offshore wind has expanded rapidly as developers pursue stronger, steadier winds in deeper waters and unlock a much larger siting envelope than is available nearshore. Market snapshots show a steep rise in installed and announced capacity, with floating platforms expected to take an increasing share of new projects as developments migrate to depths beyond the practical range of fixed foundations [1].

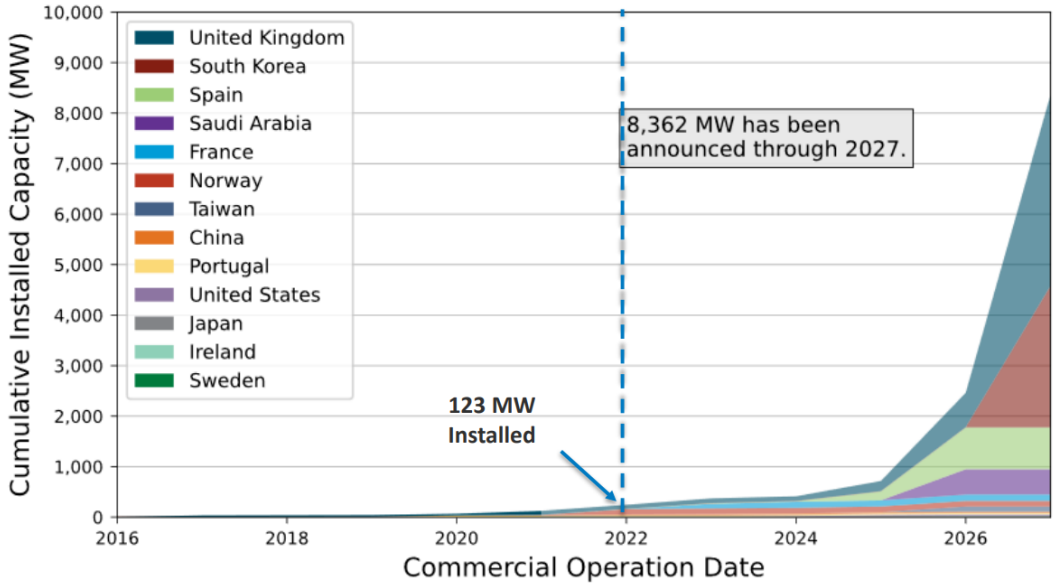


*Figure 1: Growth of the offshore floating wind market through 2027[1].*

A U.S. wind resource map (see **Figure 2**) at 100 m highlights why: the most persistent, energetic winds line the coasts, especially the Northeast and Pacific margins [2]. As demonstrated in **Figure 3**, offshore wind foundation concepts span fixed (monopile, jacket, gravity base) and floating (spar, semisubmersible, tension-leg); the semisubmersible has emerged as a leading option due to its balance of draft, stability, and tow-to-port logistics [3].

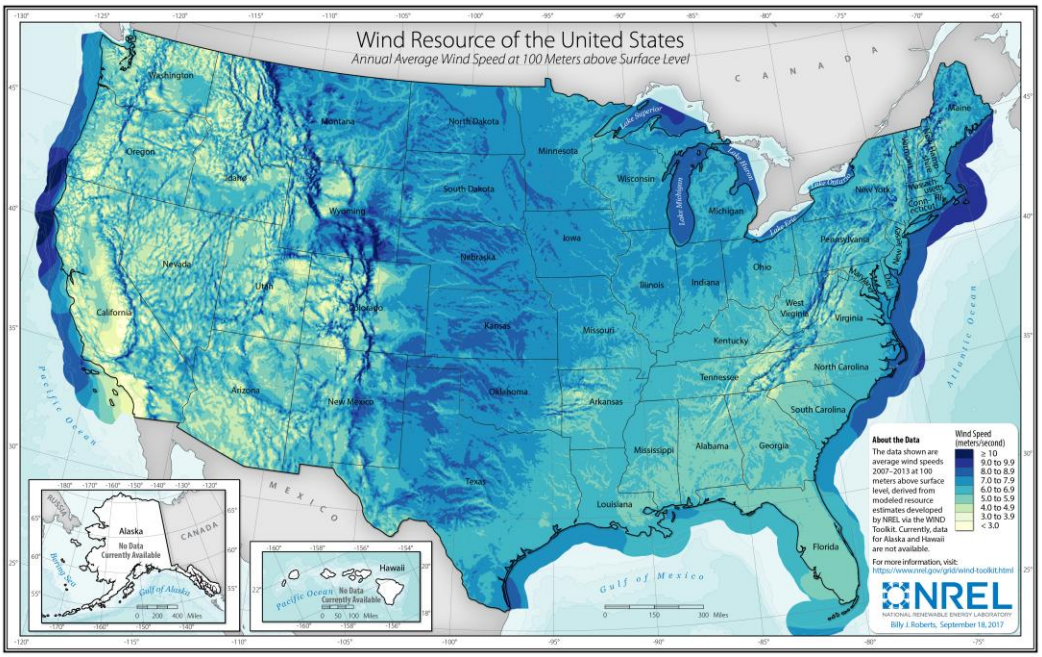


*Figure 2: Wind resource for the U.S. at 100 m above surface level [1].*

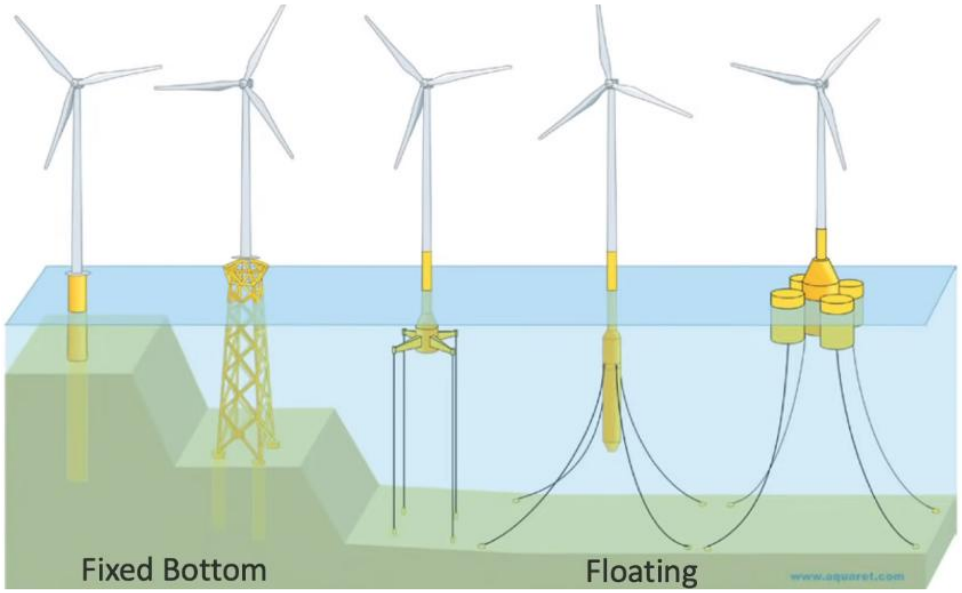


*Figure 3: Different fixed and floating foundation designs, deployed depending on water depths [3].*

## 1.2 Dynamics and Loads on Floating Platform

Moving from fixed to floating changes the structural problem from "hold the tower still" to "control platform motion." Comparative load studies show that floating platforms experience larger ultimate loads than equivalent land-based turbines, driven by the platform's freedom to heave and pitch. According to Figure 4, the sea-to-land ratios of the UMaine/OC4-type semisubmersible are elevated across several critical bending moments, with heave-related yaw-bearing and pitch-related tower-base moments being most consequential [4]. This motivates treatments that directly reduce platform motion, particularly in heave and pitch, so that ultimate and fatigue loads (and the control actions taken to avoid them) do not erode energy capture or shorten service life.

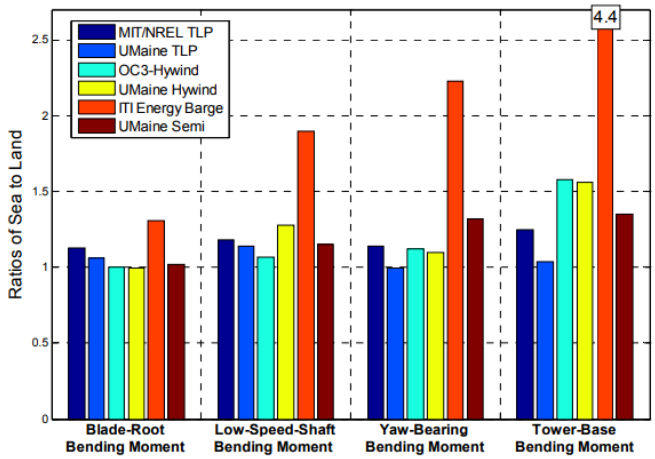


*Figure 4: Sea to land ratios of ultimate loads for the different floating platform concepts [4].*

## 1.3 Structural Control for Floating Wind Turbines

Passive structural control has a century of precedent in civil structures and is attractive offshore because it requires no external power and is robust to harsh conditions. The canonical device is the tuned mass damper (TMD) (see **Figure 5**), a secondary mass on a spring and damper tuned near a target natural frequency to counteract motion [5], [6], [7]. An expanded family of devices adds an inerter, which produces force proportional to relative acceleration rather than displacement or velocity. Adding inertance creates the tuned inerter damper (TID) (see **Figure 6**), which can deliver TMD-like (or better) suppression with much less physical mass and offers several realizations (parallel/series combinations of spring, damper, and inerter) [8], [9], [10], [11].

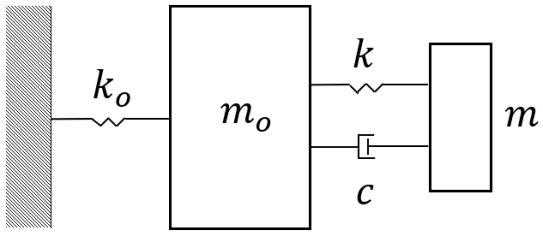


*Figure 5: Diagram of a simple TMD [12].*

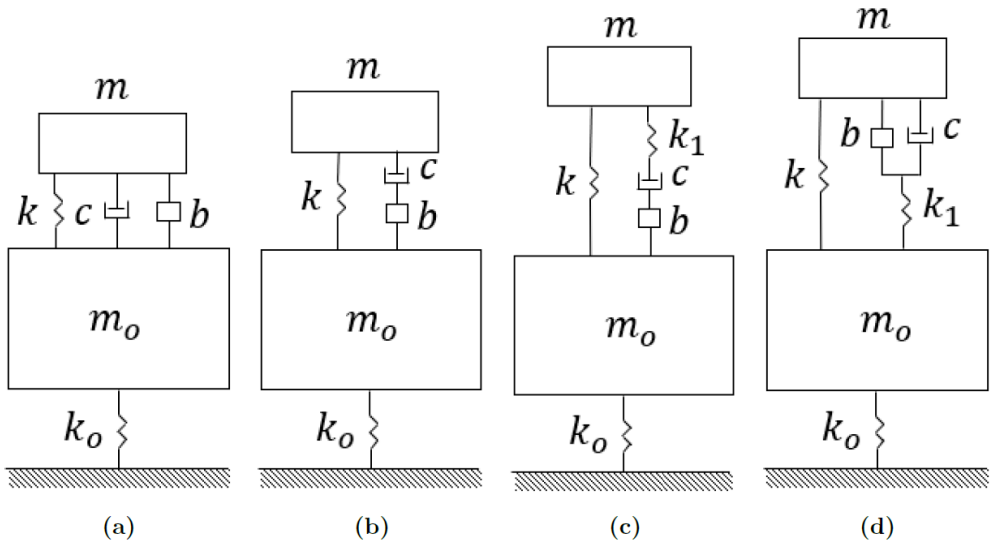


*Figure 6: Different TID configurations [12].*

Prior work has brought structural control into the offshore context: nacelle- or platform-mounted TMDs on monopile, barge, spar, and semisubmersible systems consistently reduce motions and loads; inerter-based concepts further improve performance in several studies [13], [14], [15], [16], [17].

## 1.4 Project Approach

Building on the literatures, this project studies column-integrated absorbers for a semisubmersible: three identical devices placed in the main columns and aligned with the platform's dominant vertical motions. We analyze a baseline (no device), a TMD in each column, and an optimal TID configuration that adds inertance and an auxiliary spring. Models are derived and verified against established hydrodynamics (potential-flow BEM) and benchmark software; parameter studies and optimization runs then quantify heave/pitch reductions under free-decay and wave excitation. A 1:50 semisubmersible platform is built and tested with TMDs component in the wave tank. The central result is consistent with the literature: both TMD and TID reduce motion relative to baseline.

# 2 Offshore Wind Platform Aero-Hydro-Structure Modeling

## 2.1 High Fidelity Modeling using OpenFAST

### 2.1.1 Modeling Framework and Scope

This project models the coupled aero-hydro-servo-elastic behavior of a floating offshore wind turbine (FOWT) using OpenFAST, a modular simulation environment that partitions physics into interoperable components (AeroDyn, HydroDyn, ElastoDyn, ServoDyn, etc.) as shown in **Figure 7** [18], [19], [20]. Each module is configured through its own input file and exchanges states and loads with the others at every time step, enabling consistent, high-fidelity co-simulation across aerodynamics, hydrodynamics, structures, and controls. Within this architecture, ServoDyn serves as the locus for plant controls and structural damping devices.

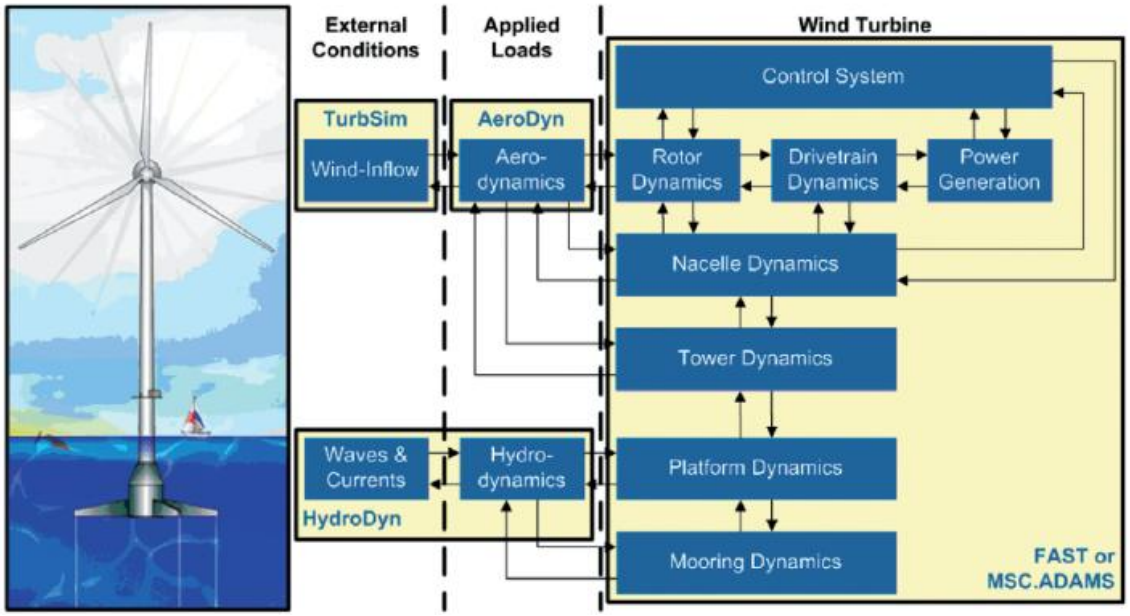


*Figure 7: Diagram of the OpenFAST modular framework [21].*

This project extends ServoDyn's Structural Control (StC) capability to support an inerter-based absorber. StC already hosts tuned mass dampers (TMDs), tuned liquid column dampers, and related options; adding inerter dynamics leverages that existing scaffold rather than altering the aero-elastic or hydrodynamic

solvers. Constraining changes to StC preserves trusted module behavior while making it possible to test alternative absorber concepts in a consistent, high-fidelity loop.

OpenFAST is used not merely as a numerical integrator but as the authoritative definition of plant-controller coupling. The absorber's forces and moments are computed inside StC in the component frame and passed to ServoDyn for transformation and dispatch to the rest of the plant, ensuring that the added device influences turbine response through the same interfaces as existing controllers. This preserves numerical stability and makes the new functionality compatible with standard workflow, post-processing, and certification-style test cases.

### 2.1.2 Baseline Model Configuration

All high-fidelity simulations adopt the OC4 DeepCwind semisubmersible [22] carrying the NREL 5-MW reference turbine as the baseline plant, as shown in **Figure 8**. This choice exploits a configuration already distributed and widely verified in the OpenFAST ecosystem, which allows absorber effects to be isolated from baseline model fidelity concerns. The reference geometry and layout follow the OC4 documentation, providing a realistic mass/inertia and hydrostatics foundation for control evaluation.

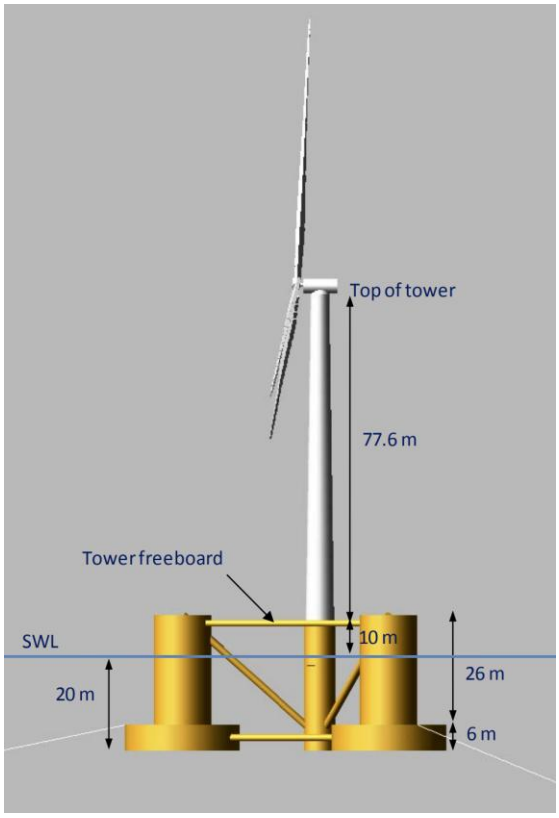


*Figure 8: Diagram of the OC4 semisubmersible floating system used as the baseline model for this project [22].*

Global simulation control adheres to the standard OpenFAST main input for the OC4 case (e.g., total run time, recommended time step, and Jacobian refresh interval). The typical setup activates ElastoDyn, ServoDyn, HydroDyn, and MoorDyn, with module time step and Jacobian cadence taken directly from the certification example to maintain reproducibility across runs. This ensures the absorber comparison is performed within a known and repeatable integration scheme.

### 2.1.3 Structural-Control Formulation in OpenFAST

In StC, the absorber's primary mass is modeled as a particle defined within a hierarchy of reference frames. The device position in the global frame is formed by composing the FOWT component origin (e.g., the platform) with the device's local coordinates; velocities and accelerations follow from time differentiation, which introduces terms associated with platform rotation rates. This kinematic foundation provides the device states needed for the control model and for consistent transformation between local and global frames.

Using this kinematics, the vertical-TMD acceleration expression in StC combines platform inertial terms, device stiffness and damping, gravity, and optional contributions such as stops, preload, and user-prescribed forces. The same formulation furnishes horizontal load components on the platform that arise from coupling with rotations. These relations are written explicitly in acceleration and force form to join with OpenFAST's state-space integrators.

The StC outputs to ServoDyn are a vector of net forces and moments imparted by the structural controls, returned in the global frame after applying the appropriate rotation matrix. By centralizing these transformations, StC ensures that any structural-control device—conventional TMDs or the inerter-based absorber introduced here—interacts with the rest of the plant through a uniform interface, simplifying configuration and verification.

### 2.1.4 Tuned Mass Dampers (TMDs) in OpenFAST

The tuned mass damper's (TMD's) primary hanging mass is modeled as a particle, and the section carefully builds the kinematics used by StC. The TMD position in the global frame is written as the sum of the platform origin's position and the TMD's position relative to the platform; the same relation is expressed in the platform's local frame for computation. Time differentiation gives velocity and then acceleration in the local frame, introducing terms from platform rotations (angular velocity and angular acceleration). These steps define the coordinate frames (global origin **O**, reference frame origin **P**, local

orientation **N**) and establish the reference matrices used to transform between frames as shown in **Figure** 9. In local orientation ***N***, the kinematics are written as $\vec{r}_{TMD/OG} = \vec{r}_{P/OG} + \vec{r}_{TMD/PG}$ and $\vec{r}_{TMD/PG} = \vec{r}_{TMD/OG} - \vec{r}_{P/OG}$ ; these relations become the basis for subsequent velocity/acceleration expressions.

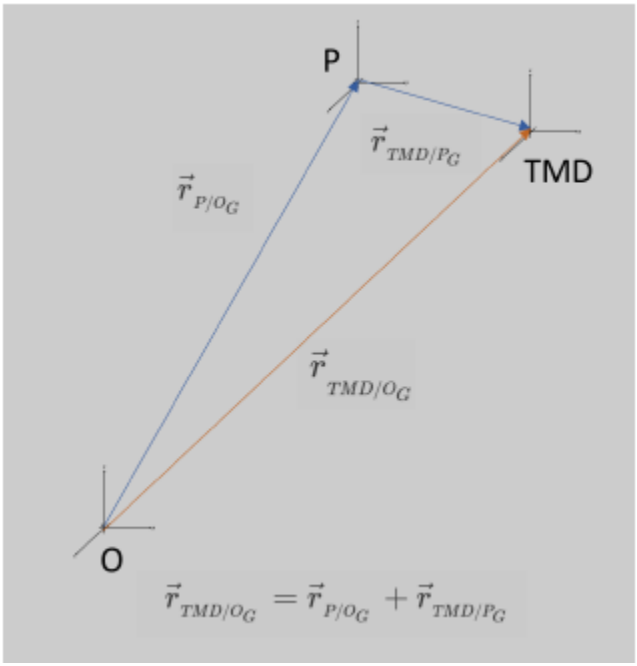


*Figure 9: Diagram of the body-fixed reference frames and position vectors used to define the TMD position in OpenFAST [23].*

Next, we replace the inertial acceleration with a force balance to connect kinematics to dynamics. Substituting $\mathrm{a} = \mathrm{F}/m$ into the acceleration expression yields the working equation for the TMD's acceleration relative to the platform. This formulation includes centripetal, Coriolis, and tangential terms from platform motion, as well as platform translational acceleration—providing a complete local-frame acceleration for the hanging mass that StC will integrate.

With kinematics in hand, we develop the equations of motion by summing forces on the hanging mass (motion restricted to the vertical *z* direction in the basic TMD case). The vertical force vector includes user-specified external force, stop force (to enforce displacement limits), and a preload term that offsets static spring deflection; platform rotation-coupling terms are written explicitly. Together with the earlier acceleration expression, these relations provide the inputs and outputs needed by StC so OpenFAST can

compute and return the TMD-induced forces/moments to the overall turbine model. Detail information for the equation can be found in [23].

### 2.1.5 Tuned-Inerter Damper (TID) Integration

Shown in **Figure 10**, the tuned-inerter damper extends the TMD concept by replacing a portion of moving mass with an inerter element that resists relative acceleration, enabling effective mass amplification without a large physical translator. The mechanical model used here comprises two internal degrees of freedom: the hanging mass displacement $z_d$ and the inerter node displacement $z_b$ , connected to the platform motion $z_p$ through springs $k_1, k_2$ , viscous damper $c_1$ , and inertance $b$. This arrangement is captured in the standard schematic and forms the basis for the governing equations.

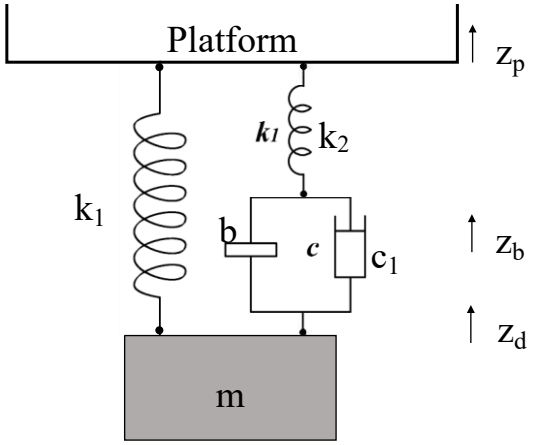


*Figure 10 Diagram of the Tuned Inerter Damper with labeled system parameters: masses, spring stiffness, and damping coefficients.*

Summing forces on the internal coordinates yields coupled expressions that include inerter and damper terms as well as the relative spring loads. Rearrangement provides explicit formulas for $\ddot{z}_d$ and $\ddot{z}_b$ in terms of the device states and platform acceleration, a format directly suited to OpenFAST's state-space implementation. Importantly, this derivation preserves the existing StC terms for stops, external forcing, and preload so that backward compatibility with the TMD pathway is maintained.

Because the goal is to modify the established TMD pathway rather than re-architect StC, the inerter equations are inserted where the TMD acceleration would normally appear, and the added internal state for the inerter node is threaded through initialization and update routines. This strategy leverages the pre-

existing solver structure and facilitates one-to-one comparisons with traditional TMD configurations in identical operating scenarios.

### 2.1.6 State-Space Implementation and Outputs

Consistent with StC conventions, the system is written as $\dot{q} = Aq + Bu$ and $Y = Cq + Du$, where $q$ is the augmented device state, $u$ collects inputs such as platform accelerations and gravity components, and $Y$ contains the global-frame loads to be returned to ServoDyn. The matrices $A$ and $B$ gather, respectively, coefficients on the state variables and the remaining terms from the acceleration-form equations, while $C$ and $D$ define the mapping to force and moment outputs.

The resulting outputs comprise the net forces and moments applied by structural controls to the platform. These are assembled in the component frame and rotated into the global frame using the platform-to-global rotation matrix so that load remains consistent across modules. The output expression inherits the standard StC contributions (including preload, stops, and any user-prescribed excitations), ensuring interoperability with existing analysis workflows.

### 2.1.7 Model Validation and Results

The OpenFAST model was first validated against theory and prior results using the OC4 semisubmersible as the reference configuration and installing one absorber in each of the three outer columns. Because adding TMD/TID hardware changes total mass and inertia, the study offset absorber mass by removing ballast water to keep platform mass comparable—an approach shown to materially affect heave decay predictions if neglected. Model fidelity also depended on solver settings; in particular, the $D_{T,\,UJac}$ parameter (Jacobian update interval) required tuning consistent with guidance for floating systems to avoid spurious pitch settling when structural control is active. With these corrections, as shown in **Figure 11 and Figure 12**, time- and frequency-domain free-decay simulations showed reductions in platform motion consistent with expectations, and the TID slightly outperforming the TMD in pitch for the specific validation case, supporting use of the model for subsequent studies.

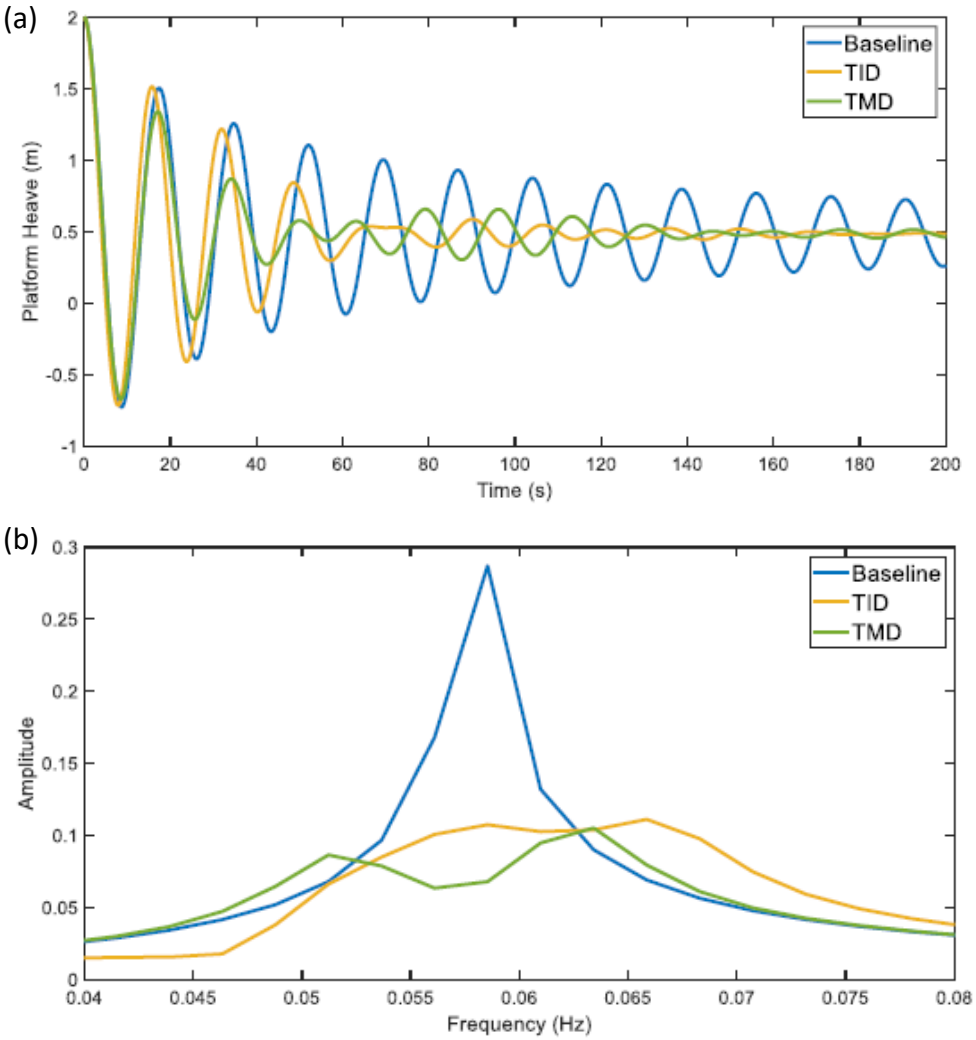


*Figure 11: (a) Time domain results for the heave free decay test at an 8% mass ratio; (b) Frequency domain results for the heave free decay test at an 8% mass ratio [23].*

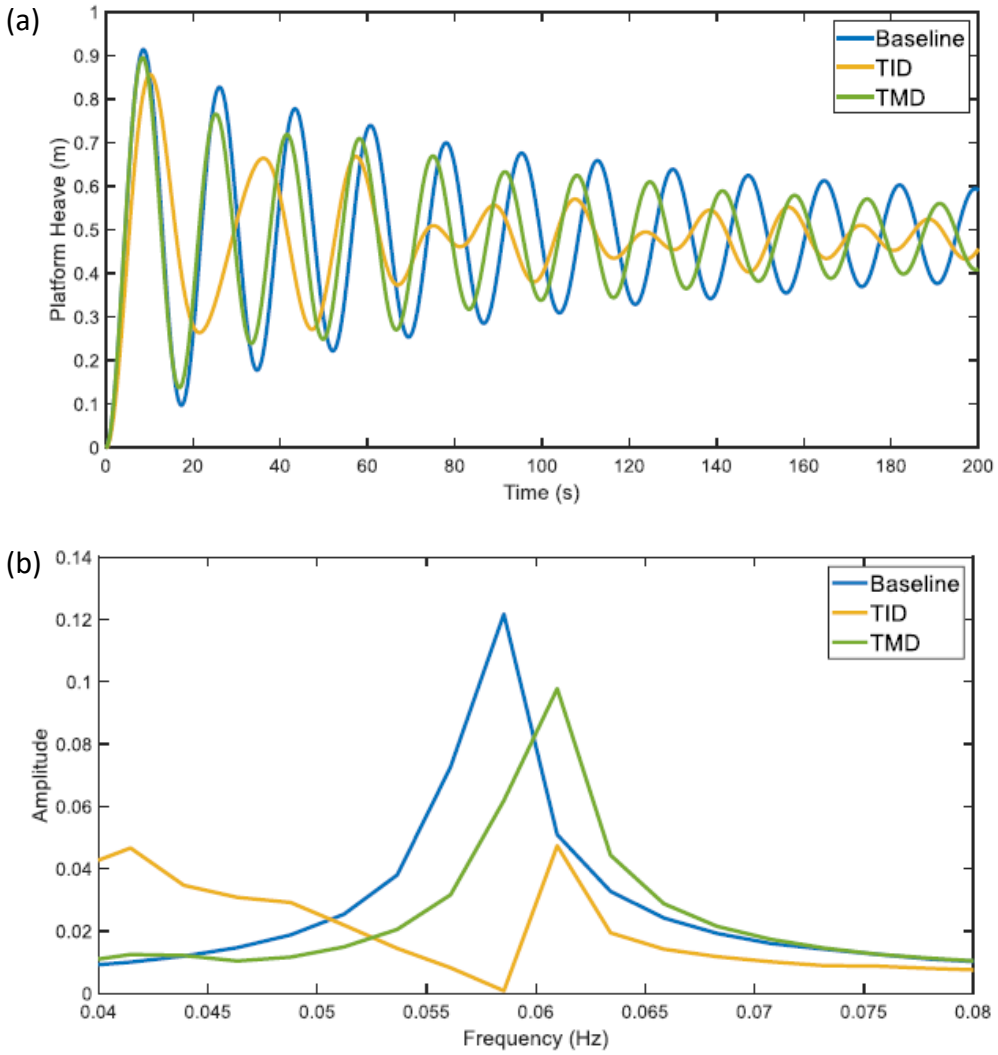


*Figure 12: (a) Time domain results for the pitch free decay test at an 8% mass ratio; (b) Frequency domain results for the pitch free decay test at an 8% mass ratio [23].*

A two-stage parametric study then identified absorber settings that minimize platform pitch. For "natural-frequency" tuning, simulations scanned stiffness and damping to produce optimized parameter sets for several mass ratios ($\mu$ = 2%, 5%, 8%) for both TMD and TID, the optimized parameters are listed in **Table 1**. The primary spring stiffness $k_1$ converged to similar values for the two devices, allowing equal $k_1$ to speed exploration of other parameters; response surfaces of RMS pitch over $(k_1, c_1)$ (TMD) and $(k_1, c_1, k_2, b)$ (TID) confirmed the tabulated optima. A complementary campaign tuned to the dominant input frequency of an irregular sea (JONSWAP, $H_s = 3$ m, $T_p = 10$ s) by examining a practical 3% system mass-ratio solution for both devices to be used in wave and wind cases. The final results from this analysis are presented in **Table 2**.

*Table 1: Optimized values from the parametric study to minimize the impact of pitch motion for the pitch free decay test [23].*

| $\mu$ | m (kg) | $k_1$ (N/m) | $c_1$ (N*s/m) | $k_2$ (N/m) | b (kg) |
|---|---|---|---|---|---|
| TMD | | | | | |
| 0.02 | 93,800 | 5,000 | 1,750 | - | - |
| 0.05 | 234,500 | 12,500 | 7,500 | - | - |
| 0.08 | 375,200 | 19,000 | 15,000 | - | - |
| TID | | | | | |
| 0.02 | 93,800 | 5,500 | 75 | 125 | 2,000 |
| 0.05 | 234,500 | 12,500 | 250 | 350 | 6,000 |
| 0.08 | 375,200 | 20,000 | 250 | 450 | 8,000 |

*Table 2: Optimized values from the parametric study to minimize the impact of pitch motion for the JONSWAP wave spectrum [23].*

| $\mu$ | m (kg) | $k_1$ (N/m) | $c_1$ (N*s/m) | $k_2$ (N/m) | b (kg) |
|---|---|---|---|---|---|
| TMD | | | | | |
| 0.03 | 140,700 | 70,000 | 2,000 | - | - |
| TID | | | | | |
| 0.03 | 140,700 | 65,000 | 3,000 | 20500 | 500 |

Using the natural-frequency-tuned sets, pitch free-decay tests quantified performance across mass ratios. As shown in **Figure 13**, RMS pitch reductions relative to baseline reached ~37–52% for the TMD and ~36–49% for the TID as $\mu$ increased from 2% to 8%, with the TMD slightly better on average in this benchmark. Frequency-domain analyses around the platform's pitch natural frequency (≈0.039 Hz) showed broadly comparable attenuation, with the TID sometimes yielding a smaller peak amplitude at resonance. Looking at the numerical data in **Table 3**, it appears that the performance of the TMD and TID are heavily dependent on the mass ratio and are sensitive to changes in the stiffness and damping values. Thus, the project team noted that a more precise optimization could further shift the balance between devices.

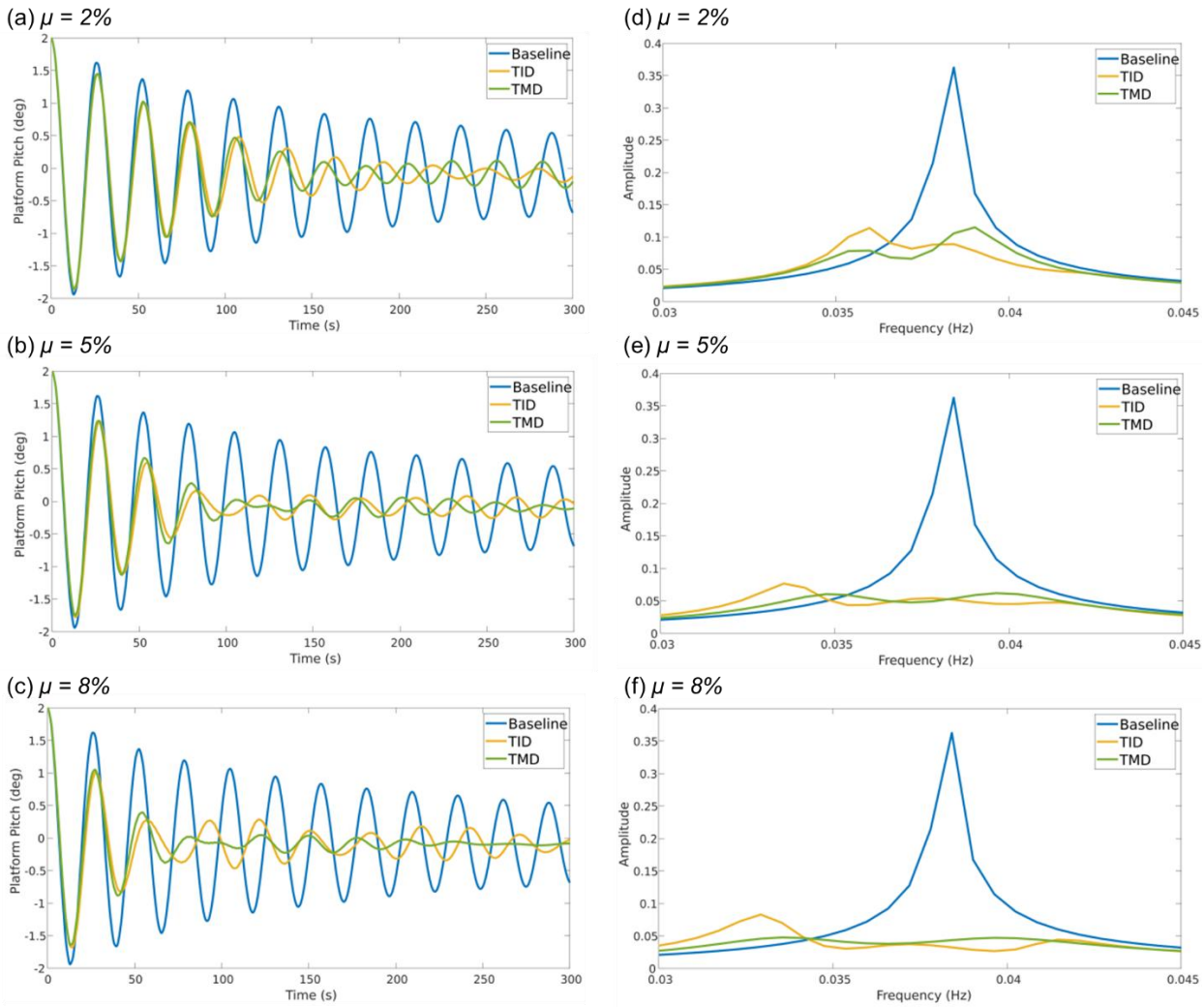


*Figure 13: Time domain results for the (a) 2%; (b) 5%; (c) 8% mass ratio cases for the TMD and TID compared to the baseline pitch free decay test. Frequency domain results for the (d) 2%; (e) 5%; (f) 8% mass ratio cases for the baseline, TMD, and TID pitch free decay test [23].*

*Table 3: Results for pitch free decay test [23].*

| Case | RMS Pitch (Degrees) | Percent Reduction |
|---|---|---|
| Baseline | 0.3996 | - |
| TMD | | |
| $\mu$=0.02 | 0.2525 | 36.805 |
| $\mu$=0.05 | 0.2093 | 47.614 |
| $\mu$=0.08 | 0.1913 | 52.132 |
| TID | | |
| $\mu$=0.02 | 0.2541 | 36.403 |
| $\mu$=0.05 | 0.2131 | 46.671 |
| $\mu$=0.08 | 0.2050 | 48.69 |

For the wave-only simulations, we applied the JONSWAP sea state used in tuning ($H_s = 3$ m, $T_p = 10$ s) and adopted the resulting 3% mass-ratio parameters. As seen in Figure 14, after discarding an initial 800 s to ensure steady response, both TMD and TID clearly reduced pitch in the time domain relative to the baseline. **Figure 15** demonstrated the reduction in the frequency-domain, especially near the primary wave frequency (~0.1 Hz), indicating that either device, when tuned to the sea state, effectively suppresses pitch response. The study anticipates that tighter parameter optimization could increase the observable benefits.

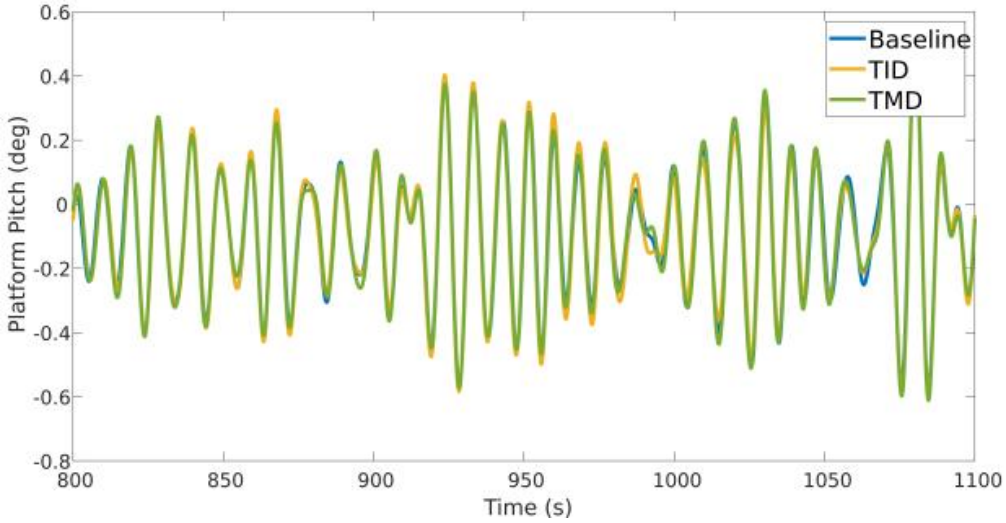


*Figure 14: Time domain results for the baseline, TMD, and TID using a mass ratio of 3% with a JONSWAP wave with a period of 10 seconds and height of 3 meters [23].*

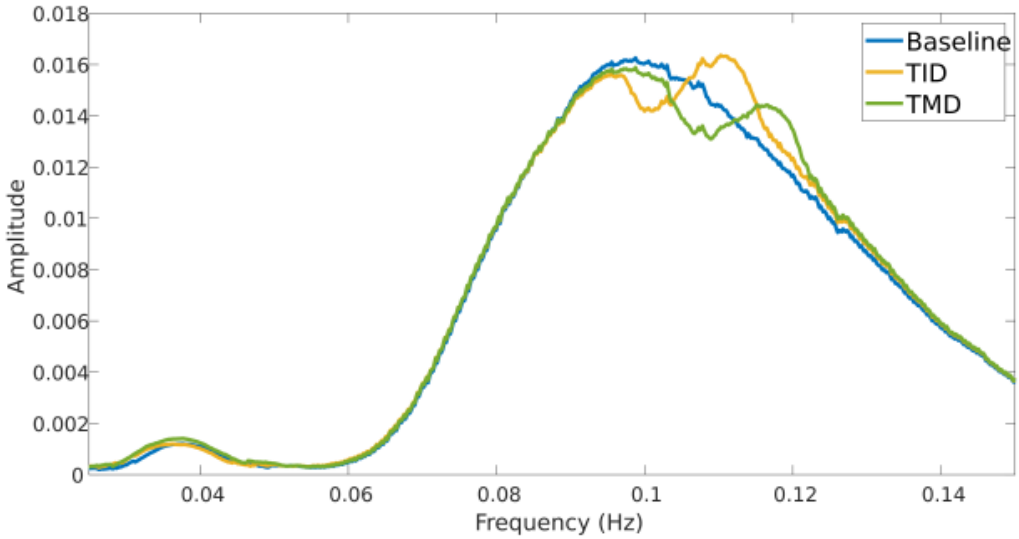


*Figure 15: Frequency domain results for the baseline, TMD, and TID using a mass ratio of 3% with a JONSWAP wave with a period of 10 seconds and height of 3 meters [23].*

## 2.2 Reduced-Order Modeling for Design Optimization

### 2.2.1 Modeling Framework and Scope

Designing and tuning vibration absorbers requires running thousands of simulations while sweeping through many candidate settings. Full-fidelity tools such as OpenFAST are invaluable for final verification, but they are too computationally heavy for early-stage design search. To make optimization practical, we developed a reduced-order model (ROM) that captures the key motions that drive loads and comfort—namely the platform's surge, heave, and pitch—together with the motion of the absorber(s). **Figure 16** shows the baseline platform with no structural platform. This ROM runs quickly and consistently, enabling broad parameter sweeps and automated search. Detail information regarding the ROM can be found in [12].

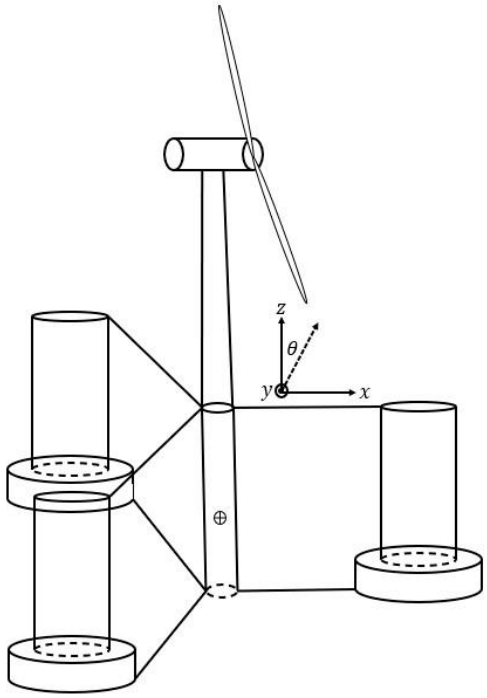


*Figure 16: Baseline platform with no structural control.*

The ROM is built to be faithful to the same physical picture used in high-fidelity models: hydrodynamic forces from the waves, buoyancy, and radiation effects; a realistic platform mass and inertia; and the additional degrees of freedom introduced by tuned mass or tuned inerter dampers installed inside the three outer columns. With these ingredients, the simplified model reproduces the trends that matter for design—how much a given absorber setting shortens the time it takes the platform to settle and how much it cuts the motion under representative sea states—while running in seconds rather than minutes.

This ROM sits alongside our OpenFAST work: OpenFAST remains the 'source of truth' for aero-hydro-servo-elastic behavior and module-level changes, while the ROM is our tool for optimization loops. In practice, the two complement each other; once the ROM narrows the viable region of the design space, we check the best candidates in OpenFAST and refine.

The ROM treats the platform as a rigid body that can move forward/back (surge), up/down (heave), and rotate nose-up/nose-down (pitch). When absorbers are added, as shown in **Figure 17**, the model adds their relative motions: three extra coordinates for a tuned mass damper (one in each column), and three additional internal coordinates for a tuned inerter damper to represent the inerter linkage. This lets the ROM compare a "baseline" system with no absorber against systems equipped with TMDs or TIDs in an apples-to-apples way. For consistency and manufacturability, the three columns use the same absorber settings.

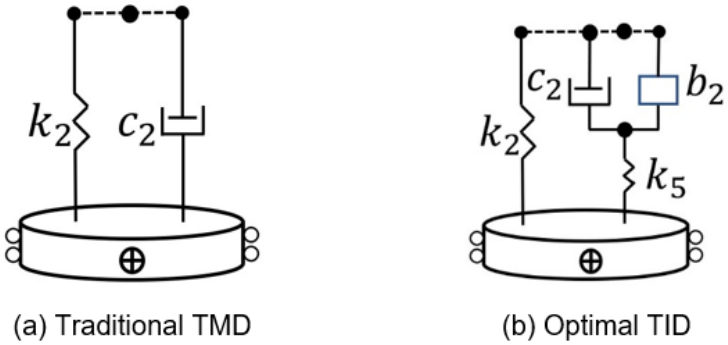


*Figure 17: Diagrams of the structural control methods (absorbers) implemented into the platform.*

Hydrodynamics are described using frequency-dependent coefficients (added mass, radiation damping, and hydrostatic stiffness) generated by a boundary-element solver and tabulated versus wave frequency. To keep the model fast, the ROM selects representative coefficients rather than performing a full convolution at every time step. Extensive checks show this "single-frequency" approach preserves the design-relevant behavior across our test cases and keeps the ranking between configurations (baseline vs. TMD vs. TID) intact. **Figure 18** shows the implementation of different absorbers in the platform. System properties—total mass, platform/tower/nacelle/rotor centers of gravity, and overall inertia—come from established OC4/5-MW references and are condensed into the ROM so that the simplified model carries realistic weights and balance. This ensures that when we compare a change in absorber settings, we are seeing the true platform response rather than an artifact of unrealistic mass distribution.

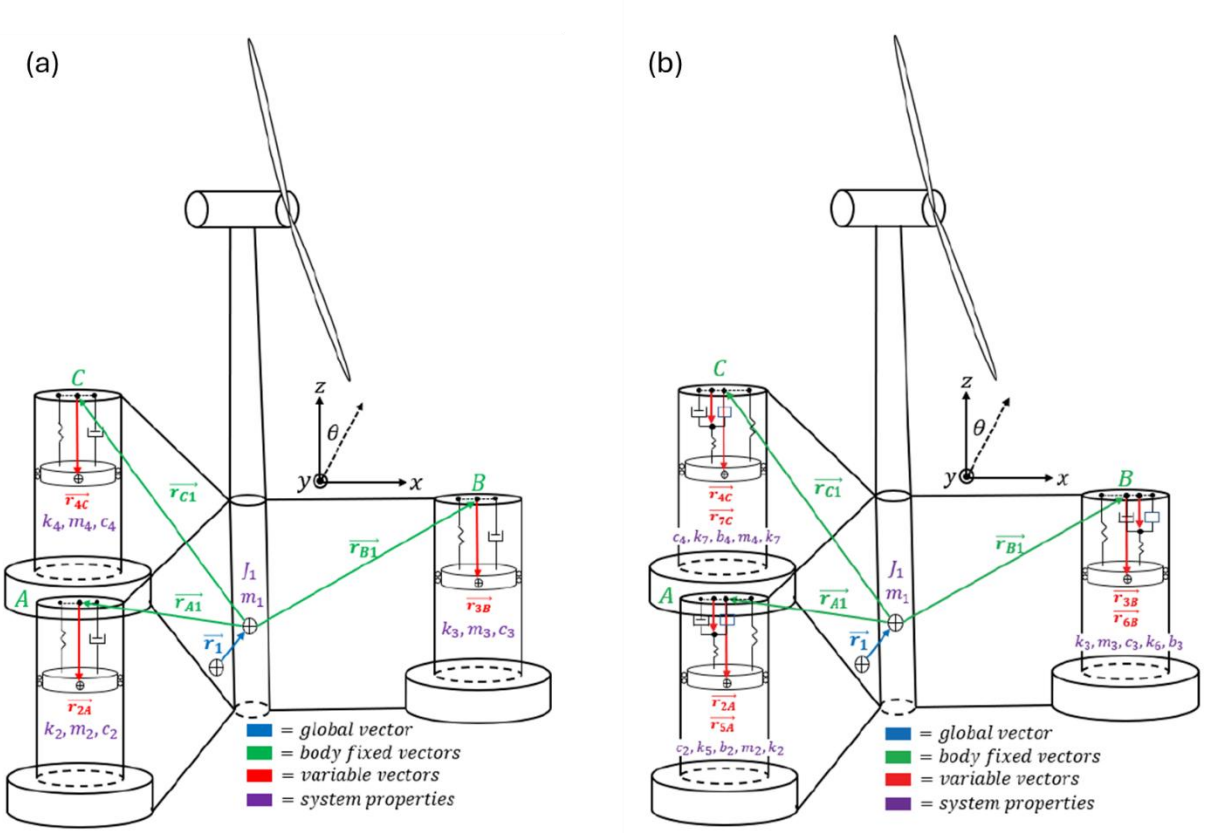


*Figure 18: Diagram of the semisubmersible platform with (a) TMDs; (b) TIDs [12].*

### 2.2.2 Calibrating and Verifying the ROM

Before using the ROM for design, we verified that it behaves like an established wave-structure simulator. We matched free-decay tests (drop in heave and small step in pitch) against WEC-Sim (see **Figure 19**), which uses the same linear wave theory and boundary-element hydrodynamics. The results for the verification of the baseline configuration can be seen in **Figure 20**.

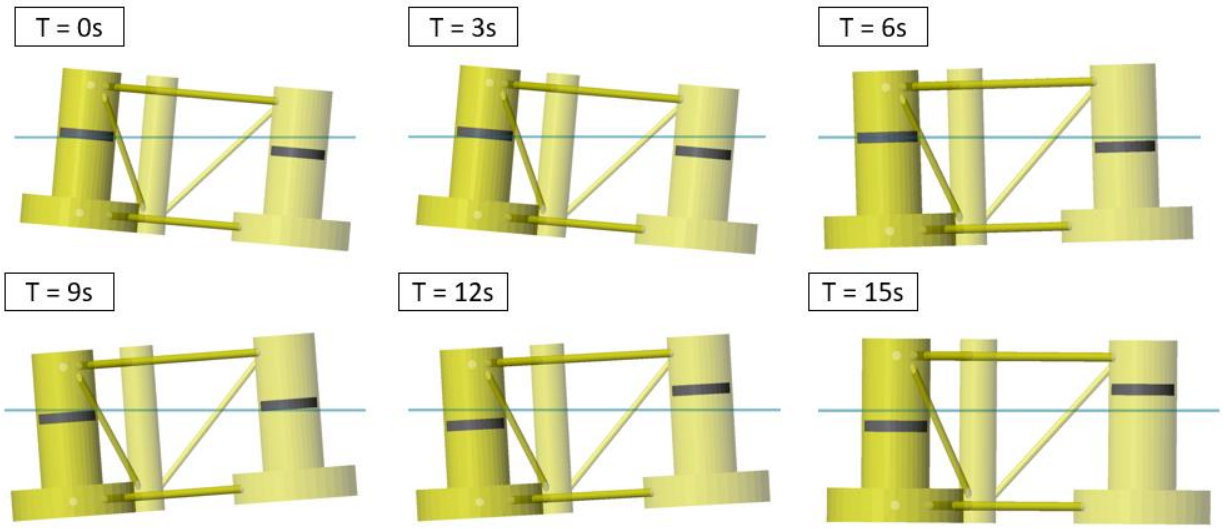


*Figure 19: Snapshots of the WEC-Sim TMD model used to verify the TMD model [12].*

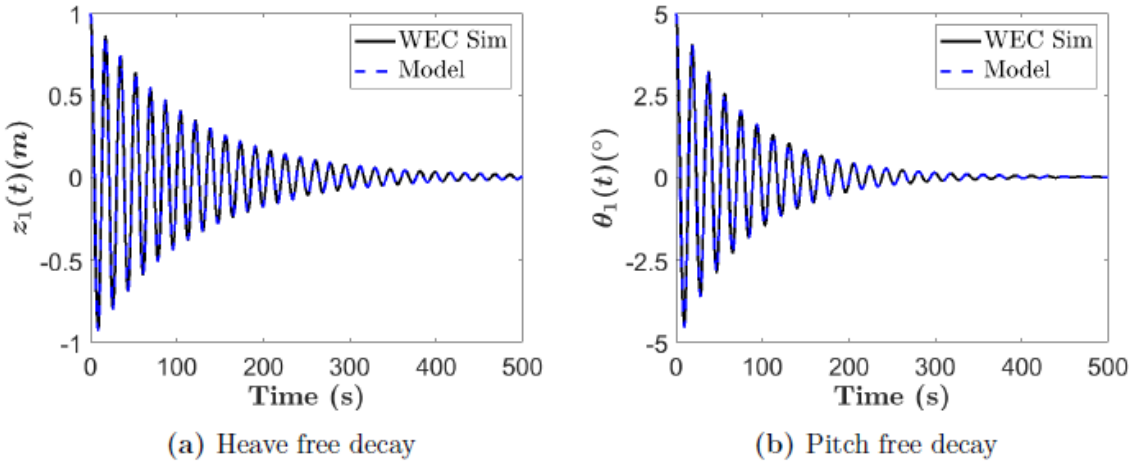


*Figure 20: Free decay test comparison between WEC-Sim and the derived model for the baseline configuration [12].*

Furthermore, the results for the verification of the TMD configuration are shown in **Figure 21**. The time histories and root-mean-square (RMS) values overlay closely for both the baseline platform and the platform with TMDs; the single noticeable gap—about two percent in a pitch decay case—was traced to pretension handling and is well within the uncertainty expected for different implementations.

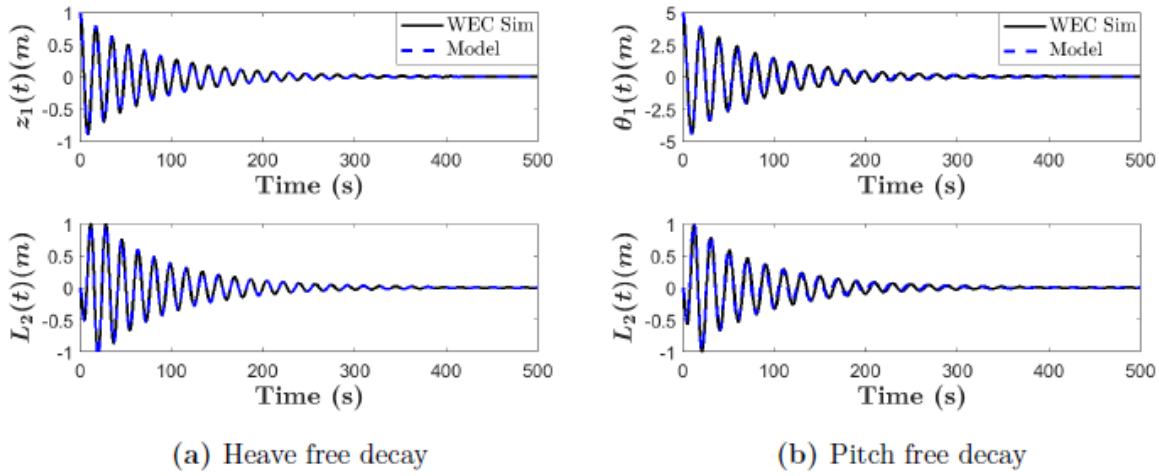


*Figure 21: Free decay test comparison between WEC-Sim and the derived model for the TMD configuration [12].*

These validations give the team a calibrated ROM that behaves like the trusted tools but runs fast enough for optimization. That speed makes it possible to explore wide parameter ranges and discover "good neighborhoods" in the design space before committing to detailed OpenFAST campaigns.

### 2.2.3 Optimization Overview

We set up the ROM to drive an automated search that "dials in" absorber settings. The search varies a small set of design knobs—stiffness and damping for a TMD; stiffness, damping, inerter strength, and an additional spring for a TID—while holding a chosen "mass ratio" (the absorber mass as a share of overall system mass) and the three-column symmetry. For each candidate, we simulate a standard set of scenarios and compute simple metrics that correlate with comfort and loads. The headline metric is the RMS motion of the platform in heave and pitch. Lower RMS equals better control.

The optimization itself uses a robust, derivative-free "pattern search." It is well-suited to our problem because different combinations of stiffness, damping, and inertance can yield similar performance and the landscape has gentle valleys instead of one sharp peak (see **Figure 22**). In practice, the search converges reliably and maps out smooth surfaces of performance versus design knobs; these surfaces make it easy to spot practical designs that sit on wide plateaus (more tolerant to manufacturing and aging) rather than sharp ridges.

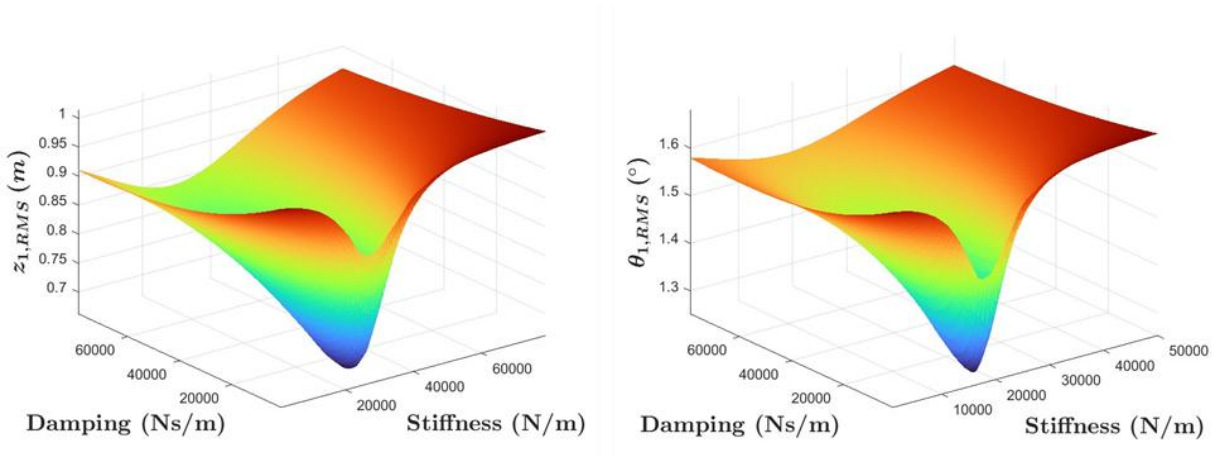


*Figure 22: Surfaces showing the objective function of the free decay optimizations as a function of the design parameters [12].*

### 2.2.4 Free Decay Optimization

Two types of scenarios guide the search. First are free-decay tests, which reveal how quickly the platform settles when disturbed and strongly reflect tuning to the platform's natural motions. Plots of the optimized heave and pitch free decay responses of the platform for a 5% mass ratio are shown in **Figure 23**. This figure visually shows the benefit of adding structural control, with the TMD and optimal TID responses settling much faster than the baseline. **Figure 24** shows the frequency domain response for the heave and pitch free decay tests, respectively. Similar to the time domain response plots, these plots also show the control outperforming the baseline and the TID outperforming the TMD.

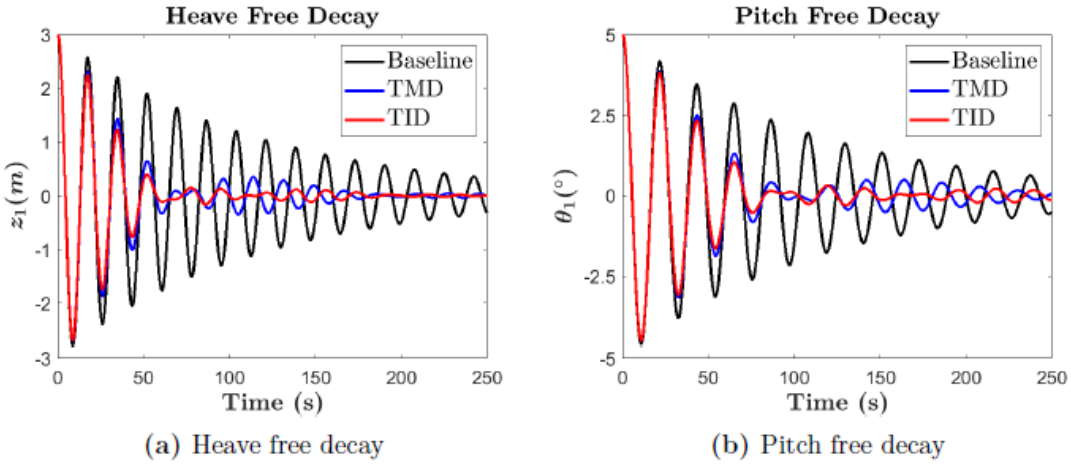


*Figure 23: Optimized free decay time domain response for the overall system with a mass ratio of 5% [12].*

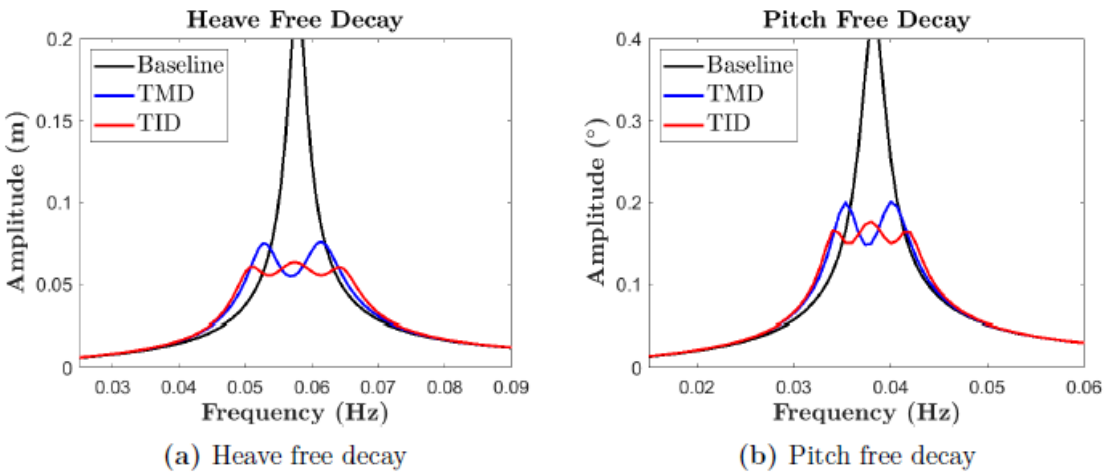


*Figure 24: Optimized free decay frequency domain response for the overall system with a mass ratio of 5% [12].*

The results of the heave and pitch free decay optimizations are shown in **Table 4**. Across mass ratios from 1% to 8% (1% steps), both the traditional TMD and the optimal TID substantially reduced free-decay motions in heave and pitch relative to the baseline. The smallest improvements observed were 18.92% in heave and 13.17% in pitch, and the benefit grew steadily with added control mass: for heave, reductions increased from 18.92% at $\mu$ = 1% to 39.38% at $\mu$ = 8%, nearly a 20-percentage-point drop in motion for only a 7-percentage-point increase in mass. The relationship between percent reduction and mass ratio is further explored in **Figure 25**. It is shown that at every mass ratio and for both degrees of freedom, the TID outperformed the TMD, with the gap widening as mass increased; in heave, the TID's percent-reduction exceeded the TMD's by 1.26 points at $\mu$=1% and by 4.49 points at μ=8%.

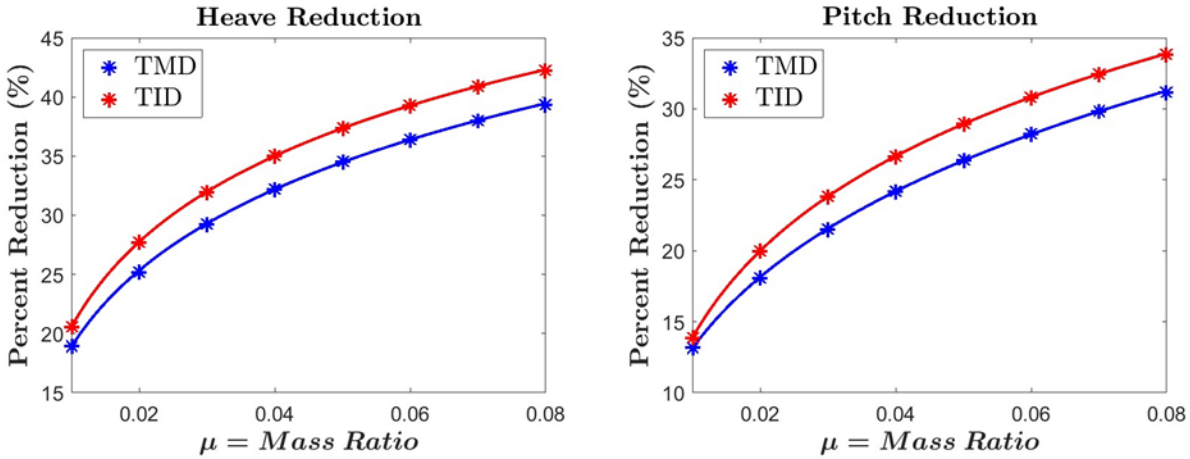


*Figure 25: Percent reduction vs. mass ratio for both heave and pitch free decay optimization studies [12].*

*Table 4: Results of the heave and pitch free decay optimizations for baseline and control configurations [12].*

| | Heave Free Decay | | | | Pitch Free Decay | | | |
|---|---|---|---|---|---|---|---|---|
| | Platform + TMD | | Platform + TID | | Platform + TMD | | Platform + TID | |
| $\mu$ | RMS (m) | % Reduction | RMS | % Reduction | RMS (°) | % Reduction | RMS | % Reduction |
| Baseline | 1.008 | - | 1.008 | - | 1.694 | - | 1.694 | - |
| 0.01 | 0.817 | 18.92% | 0.801 | 20.18% | 1.471 | 13.17% | 1.459 | 13.96% |
| 0.02 | 0.754 | 25.22% | 0.728 | 27.88% | 1.388 | 18.07% | 1.356 | 19.95% |
| 0.03 | 0.713 | 29.29% | 0.686 | 32.51% | 1.330 | 21.53% | 1.291 | 23.82% |
| 0.04 | 0.683 | 32.24% | 0.655 | 35.79% | 1.284 | 24.22% | 1.242 | 26.68% |
| 0.05 | 0.660 | 34.55% | 0.631 | 38.36% | 1.247 | 26.41% | 1.204 | 28.94% |
| 0.06 | 0.641 | 36.43% | 0.612 | 40.45% | 1.216 | 28.25% | 1.172 | 30.84% |
| 0.07 | 0.625 | 38.02% | 0.596 | 42.22% | 1.189 | 29.82% | 1.144 | 32.46% |
| 0.08 | 0.611 | 39.38% | 0.582 | 43.77% | 1.166 | 31.19% | 1.121 | 33.86% |

### 2.2.5 Regular Wave Optimization and Irregular Wave Analysis

The second optimization are representative sea states (regular and irregular waves with 5 second significant wave period) that mimic what the turbine will see most often offshore. **Figure 26** shows the optimized heave and pitch responses of the platform in time domain for a regular wave, while **Figure 27** shows the corresponding frequency domain results. **Figure 28** shows the pitch time domain response for a representative irregular wave case. Across both regular and irregular wave conditions, the trend is consistent: both absorber types reduce motion versus baseline, and the inerter-based design (TID) often achieves the same benefit with less physical mass, making it attractive for integration inside columns.

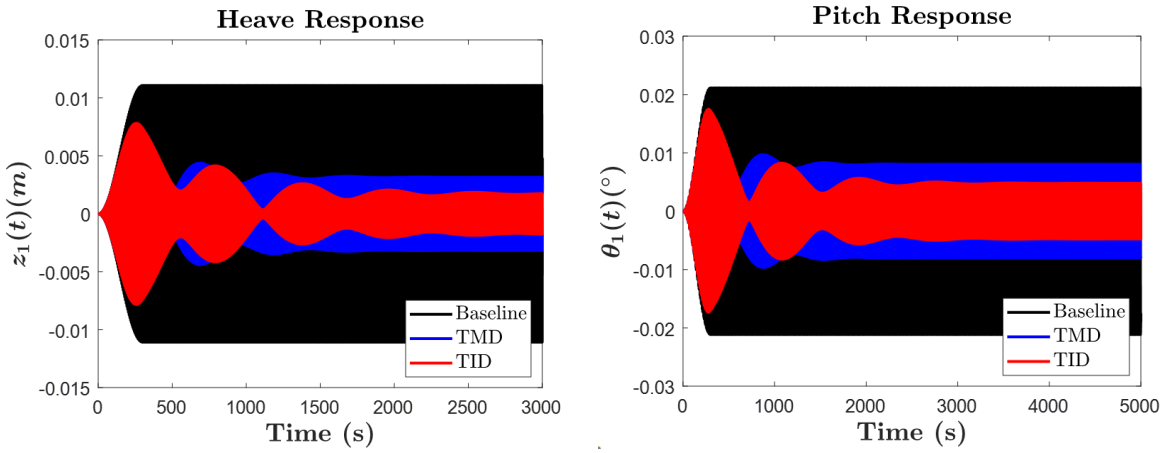


*Figure 26: Optimized heave and pitch time domain response for a representative sea state, using a mass ratio of 3% [12].*

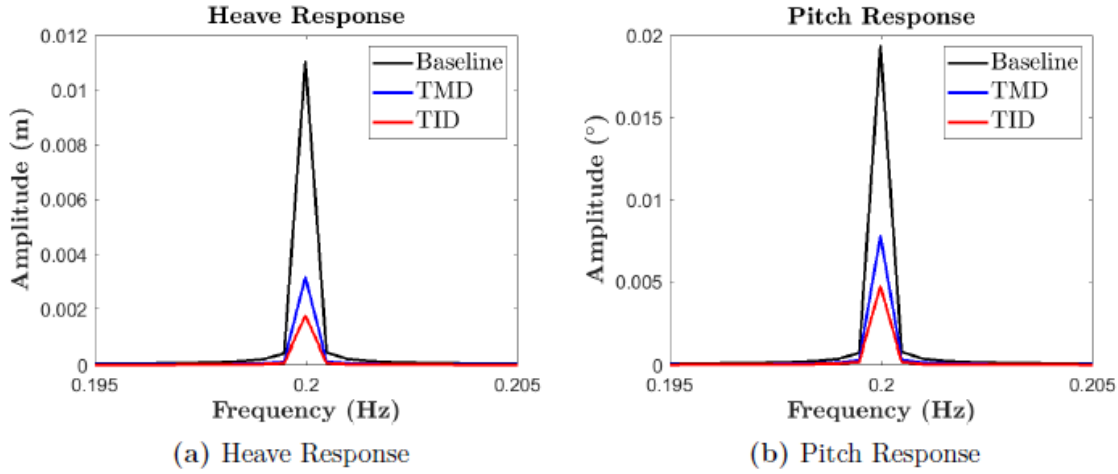


*Figure 27: Optimized heave and pitch frequency domain response for a representative sea state, using a mass ratio of 3% [12].*

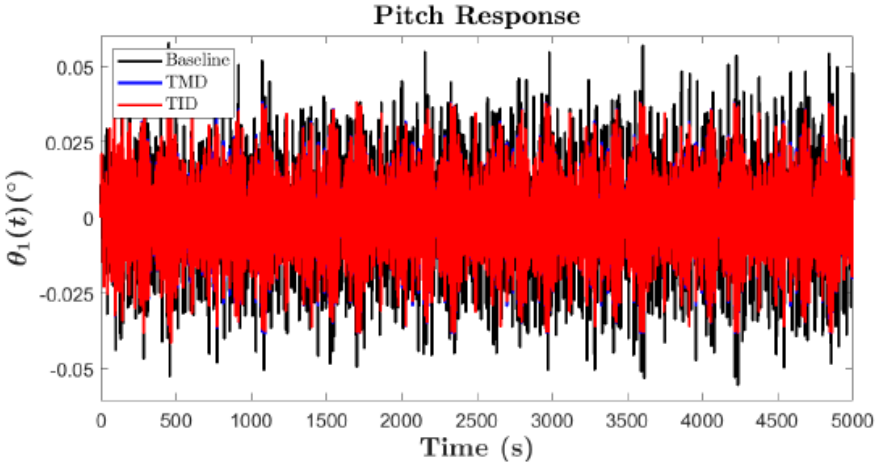


*Figure 28: Pitch time domain response for a representative irregular wave case, using a mass ratio of 3%, ran for an extended period [12].*

# 3 Critical Component Validation and Scaled Prototype Wave Tank Testing

## 3.1 Scaled Semi-submersible Floating Platform

The reference model for this study is the OC4-DeepCwind semi-submersible floating wind turbine concept. The design of the OC4 platform is well-documented and has been the subject of numerous studies, making it an ideal baseline for this research. The platform's properties, including its geometry, mass, and hydrodynamic characteristics, are publicly available through the Offshore Code Comparison Collaboration (OC4) [24]. The OC4-DeepCwind concept features a central turbine column linked to three outer columns by pontoon and cross-brace members, forming a broad water-plane for improved stability. The tested configuration of this scaled platform is shown in **Figure 29**, which captures the final experimental assembly used in this project.

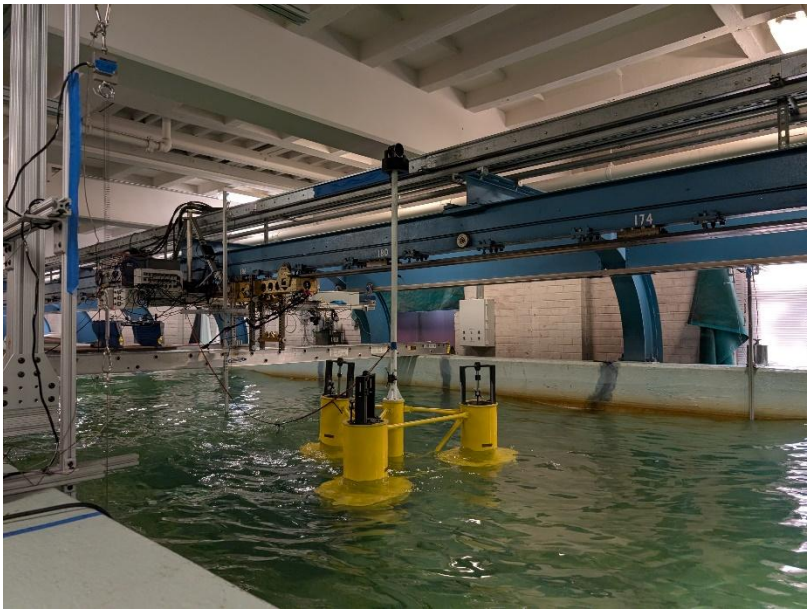

*Figure 29: Tested 1:50 OC4-DeepCwind semi-submersible floating wind turbine.*

## 3.2 Tuned Mass Damper (TMD) System

The TMD system was designed with compliant springs that can be customized by altering their thickness, width, length, and angle. A linear guide constrains the TMD's movement to a single degree of freedom, and the design was optimized for minimal friction. A large mass holder at the top of the TMD allows for easy calibration of its natural frequency. The structural layout and components of the TMD system are

depicted in **Figure 30**, showing the linear guide, compliant springs, and mass holder used to calibrate the natural frequency.

*Figure 30: The Tuned Mass Damper (TMD) module designed for platform stabilization.*

### 3.2.1 Critical Components Validation

For the tuned mass damper (TMD) to deliver reliable motion reduction—and to enable any energy-harvesting add-ons—the **spring** that sets the device's working frequency and the **linear guide** that constrains its motion must behave predictably and with **very low friction**. In practice, excessive sliding friction robs damping authority from the electromagnetic/auxiliary damper and can mask the TMD's tuned response; conversely, a low-friction guidance scheme lets us choose damping deliberately and preserve energy available for conversion. These needs—large stroke, soft and repeatable stiffness near the operating point, and minimal stick–slip in the guide—set the acceptance criteria for the 1:50 prototype and for scaling later.

#### *3.2.1.1 Spring and Linear Guide: Compliant Fixed-Guided Beams*

To meet those criteria, we replace conventional coil springs and sliding bearings with a compliant mechanism built from four inclined fixed-guided beams arranged symmetrically around the moving mass. The beams act as both the spring and the guide, so there are no rolling or sliding joints and the friction level is inherently low. When pre-biased, this architecture can deliver a quasi-constant force over the desired travel, keeping the TMD's effective stiffness low around its tuned frequency while maintaining

vertical-only motion. This concept is the basis of the prototype design and the focus of the critical-component validation work in this section.

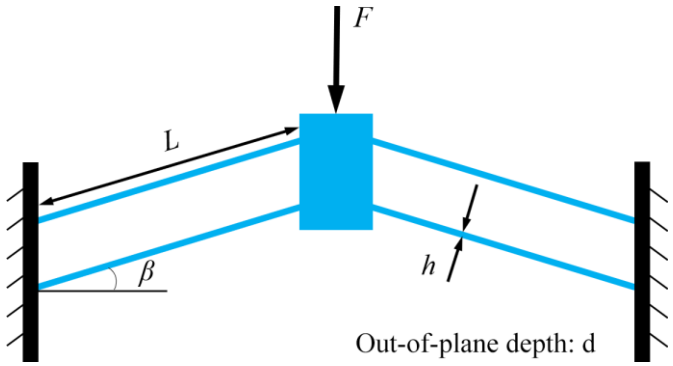


*Figure 31: Compliant mechanism with four inclined fixed-guided beams [25]*

### 3.2.1.2 Modeling Approach for Large-Deflection Springs

Because these slender beams work through large elastic deflections and carry meaningful axial load, we model them with the Chained Beam-Constraint Model (CBCM). CBCM slices each beam into small elements and enforces equilibrium and geometric compatibility across the chain, capturing both bending and axial stretching without resorting to high-friction joints. This approach is efficient enough for design iteration yet accurate in the large-deflection regime relevant to our prototype. The same solver is used to compute tip deflections, reaction forces, and the overall force–displacement curve of the four-beam assembly that the TMD "feels."

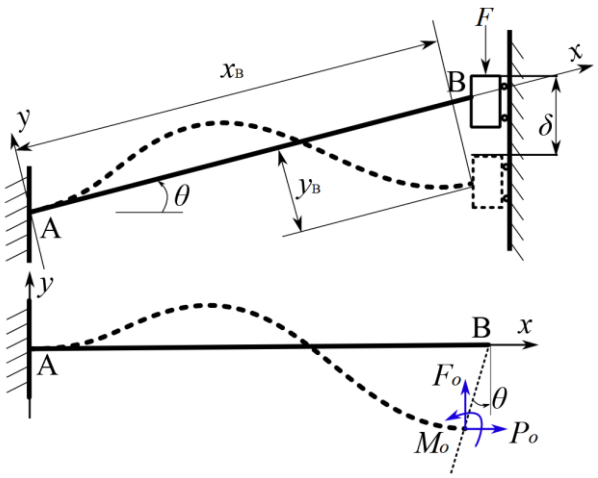

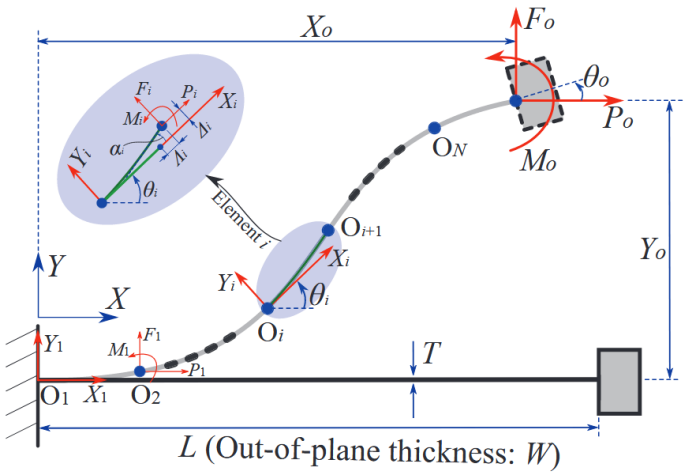


*Figure 32: CBCM divides the beam into N elements at points O2-ON [26], [27]*

### 3.2.1.3 Numerical Verification of the Spring Model

We verified the MATLAB-based CBCM solver against two published fixed-guided beam examples [4], [5], as shown in **Figure 33** and **Figure 35**. For each, we extracted the reported geometry and material properties, ran the solver, and compared the predicted force–displacement curves with the literature plots. As demonstrated in **Figure 34** and **Figure 36**, the overlays match closely, confirming that the solver reproduces the large-deflection response of inclined beams and is suitable for our compliant spring design. This verification step forms the validation of the spring model before hardware build.

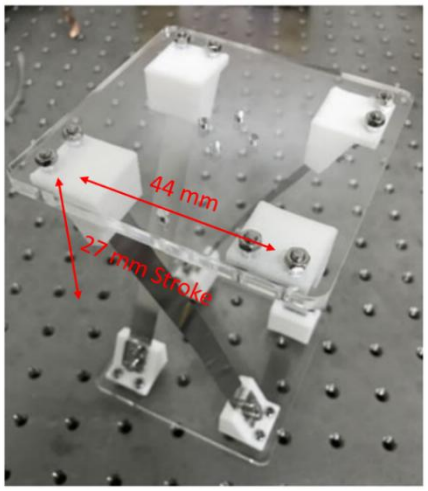


| | |
|---|---|
| **Number of Springs** | 4 |
| **Stroke** | 27 mm |
| **Footprint (width)** | 44 mm |
| **Force Range** | 12.7 N |
| **Length of Beam** | 100 mm |
| **Thickness** | 0.15 mm |
| **Width** | 13 mm |
| **Initial Angle at the Fixed End** | 64° |
| **Material** | Stainless Steel |
| **Young's modulus** | 193 GPa |

*Figure 33: Parameter extraction for compliant fixed-guided beams from literature used for validation of the CBCM solver [28]*

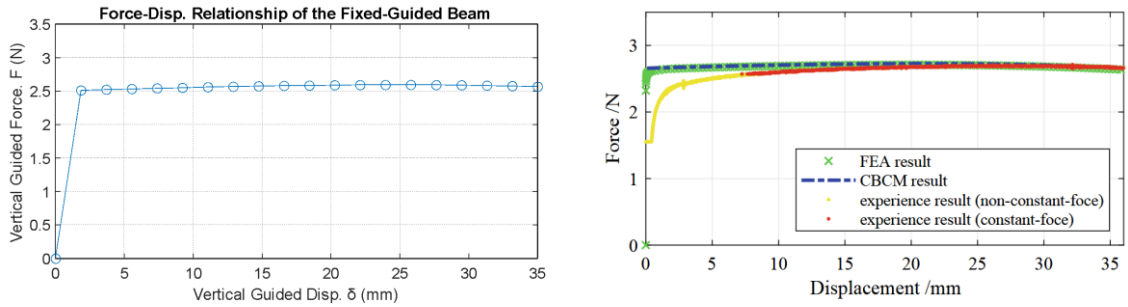


*Figure 34. Comparison of force-displacement results from the CBCM solver against reference literature [28]*

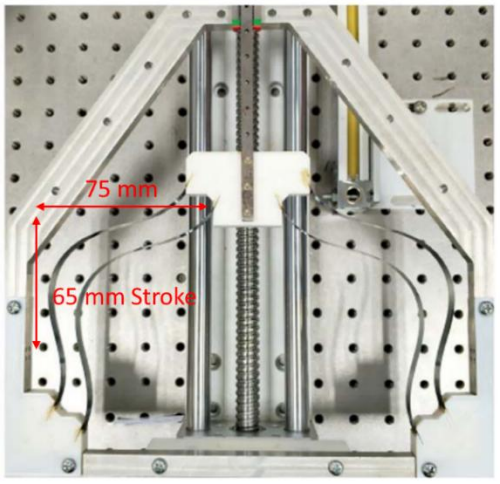


| | |
|---|---|
| **Number of Springs** | 4 |
| **Stroke** | 65 mm |
| **Footprint (Width)** | 75 mm |
| **Force Range** | 12.7 N |
| **Length of Beam** | 173.3 mm |
| **Thickness** | 0.25 mm |
| **Width** | 10 mm |
| **Initial Angle at the Fixed End** | 64.5° |
| **Material** | Steel |
| **Young's modulus** | 200 GPa |

*Figure 35. Summary of extracted beam parameters for the second fixed-guided beam example from literature [29]*

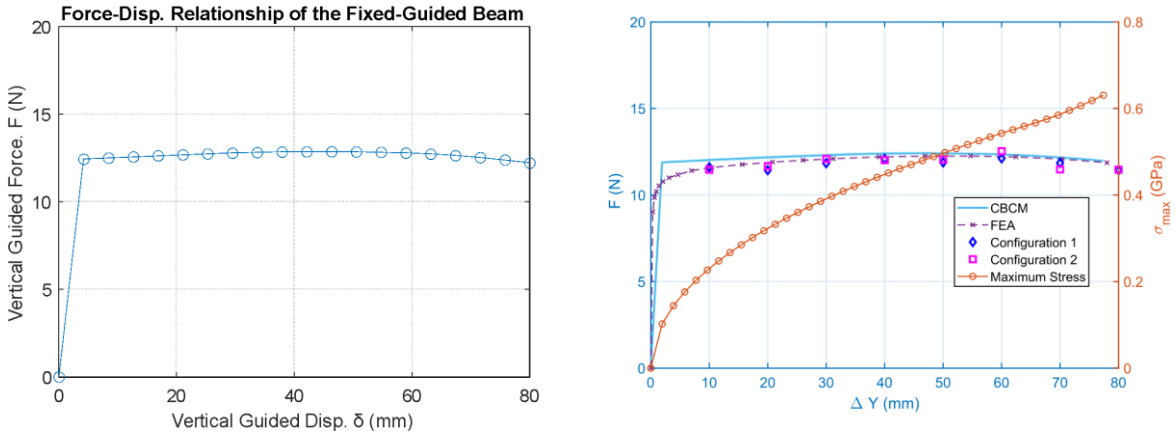


*Figure 36. Validation of CBCM solver against reference literature for the second fixed-guided beam example [29]*

### 3.2.1.4 Optimization to the Target Stiffness and Stroke

With the solver validated, we optimized the beam geometry, including thickness, width, length, number of parallel beams, and initial inclination, to match a target force–displacement curve (see **Figure 37**) that delivers the required stroke and soft effective stiffness around the TMD's operating point. A genetic algorithm drove the search while CBCM evaluated candidates, enforcing footprint limits (to fit within the column) and stress allowables (material strength with margin). The result is a leaf-spring set whose force curve tracks the target across the full motion range, while respecting packaging constraints and keeping peak stress within design limits.

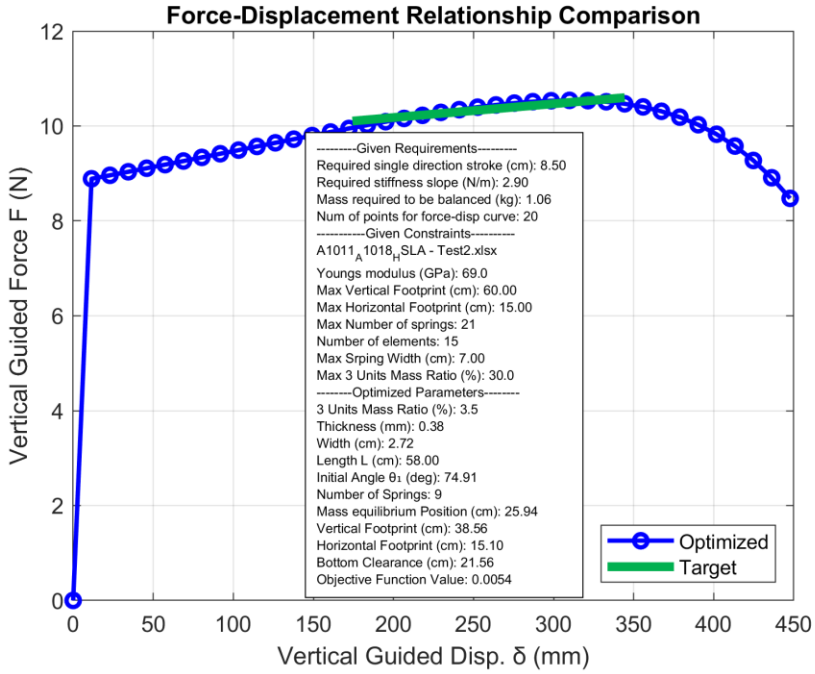


*Figure 37: Optimized force-displacement curve (blue) of the fixed-guided beams compared to the target stiffness curve (green).*

### 3.2.1.5 Deformation Shapes and Stress Distribution Check

To capture large-deflection behavior in the compliant fixed-guided beams, we discretize each beam into **N** elements and resolve the deformation of every element into axial (λ), shear (δ), and rotational (α) contributions. Aggregating the element-level kinematics over the chain gives the overall tip pose of the beam. In compact form:

$$\sum_{i=1}^{N}[(1+\lambda_i)\cos(\theta_i) - \delta_i \sin(\theta_i)] = x_o$$

$$\sum_{i=1}^{N}[(1+\lambda_i)\sin(\theta_i)+\delta_i\cos(\theta_i)] = y_o$$

$$\sum_{i=1}^{N}\alpha_i = \theta_o$$

where $\theta_i$ is the orientation of the $i$-th element's local frame, and $(x_o, y_o, \theta_o)$ is the beam tip's final position and rotation. During design, we visualize the intermediate deformation shapes across the full working stroke as shown in **Figure 38**; this "footprint sweep" is used to verify clearances and to prevent any interference with neighboring parts before hardware is built.

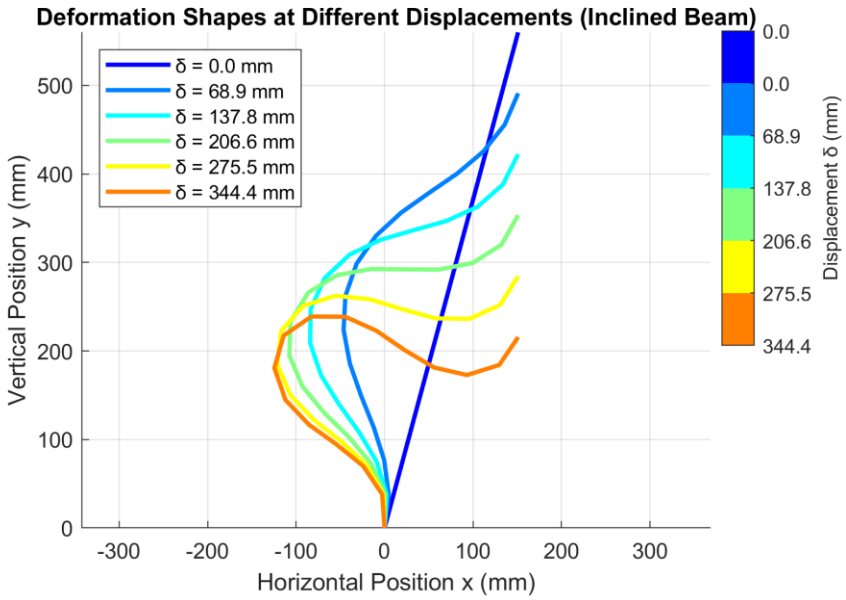


*Figure 38: Deformation shape of the optimized beam at different displacements.*

In parallel with the kinematic check, every iteration of the genetic algorithm (GA) applies a stress constraint at the element level to ensure structural integrity. The total normal stress in each element is taken as the sum of axial and bending components,

$$\sigma = \sigma_{\text{axial}} + \sigma_{\text{bending}} = \frac{P}{A} + \frac{M\,c}{I}$$

with $P$ the axial force, $A$ the cross-sectional area (thickness × width), $M$ the bending moment, $c$ the distance from the neutral axis to the outer fiber (half the thickness), and $I$ the second moment of area of the rectangular section. By embedding this stress model inside the GA's objective/constraints, the search converges only to designs that hit the target stiffness profile without exceeding material allowables over the entire stroke. This keeps the compliant spring gentle in the operating range while preserving a comfortable margin to yield.

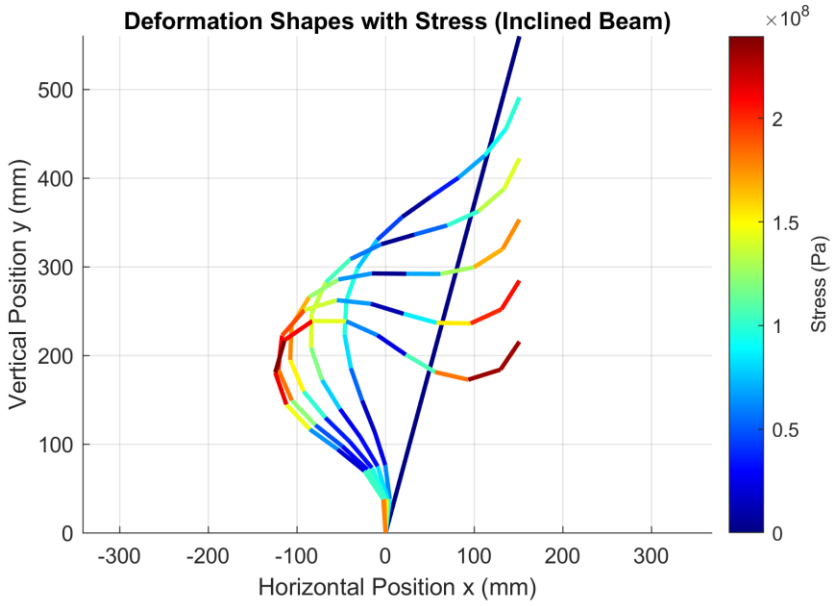


*Figure 39: Deformation profile and elemental stress distribution in the optimized beam.*

## 3.3 Scaled Prototype Tank Test

The experimental campaign was conducted at the Stevens Institute of Technology's Davidson Laboratory, which houses a high-speed towing tank well-suited for this type of hydrodynamic testing. The layout of the Davidson Laboratory's towing tank, used for hydrodynamic testing, is schematically shown in Figure 40, providing a spatial understanding of the testing environment. The facility's capabilities include a programmable wavemaker capable of generating various sea states.

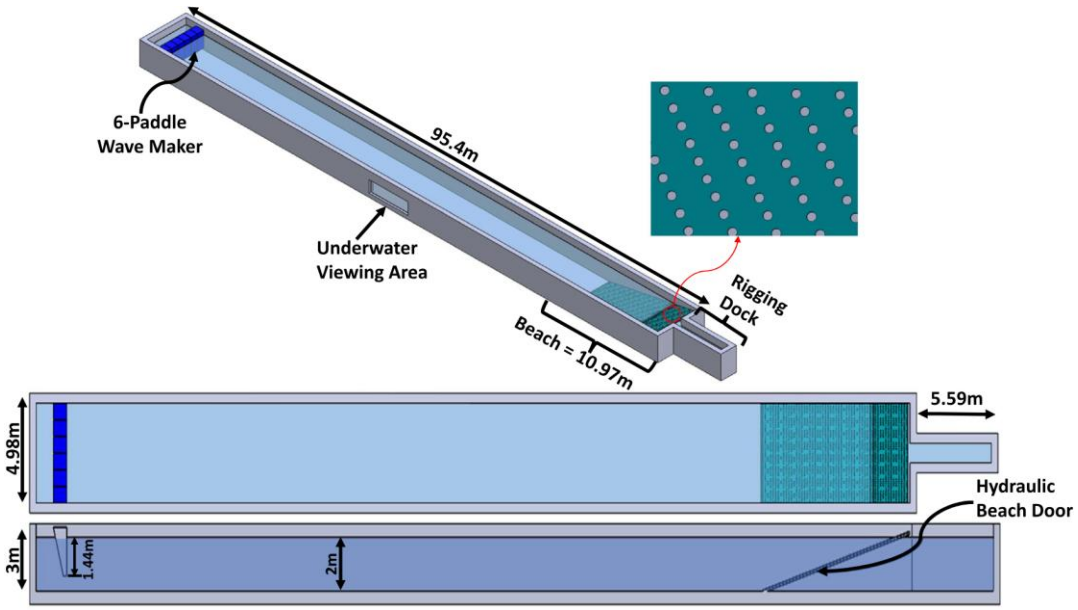


*Figure 40: Schematic for the Davidson laboratory high speed towing tank [30].*

A 1:50 Froude-scaled model of the DeepCWind semi-submersible platform was designed and fabricated. Froude scaling is essential for ensuring that the gravitational and inertial forces are correctly represented at the model scale, which is critical for accurately simulating the platform's motion in waves.

### 3.3.1 Modular Ballasting System

To achieve the precise scaled mass, center of mass, moment of inertia, and natural frequency, a modular ballasting system was developed. The integration of the modular ballasting system, seen in **Figure 41**, enabled fine-tuned adjustments to replicate the dynamic behavior of the full-scale platform, including its center of mass. This system utilizes lead weights that can be easily added or adjusted within the platform's columns. This modularity was crucial for fine-tuning the model's dynamic properties to match the target parameters.

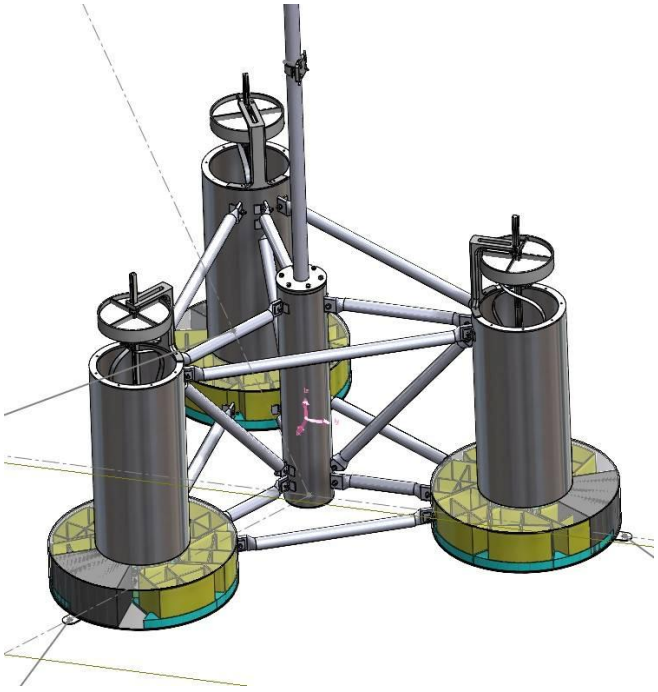

*Figure 41: Modular Ballasting System (yellow) and the tuned mass dampers assembly.*

*Table 5: Key Parameters and Scaling for the 1:50 OC4 Model.*

| ***OC4 Parameter*** | ***Full Scale*** | ***Scaling*** | ***1:50 Model*** |
|---|---|---|---|
| *Platform mass, including ballast* | 14,070,000 kg | $s^3$ | 112.56 kg |
| *CM location below SWL* | 9.89 m | $s^1$ | 0.20 m |
| *Still Water Level (SWL)* | 20 m | $s^1$ | 0.40 m |
| *Platform pitch inertia about CM* | 10,110,000,000 kg-$m^2$ | $s^5$ | 32.35 kg-$m^2$ |

### 3.3.2 Turbine Simulation

A ducted fan was integrated into the model to simulate the aerodynamic loads of the rotating turbine blades. The calibration data for the ducted fan is presented in **Figure 42**, which relates thrust output to the pulse width modulation signal, ensuring accurate representation of aerodynamic loads. This is important for capturing the coupled dynamic behavior of the entire wind turbine system.

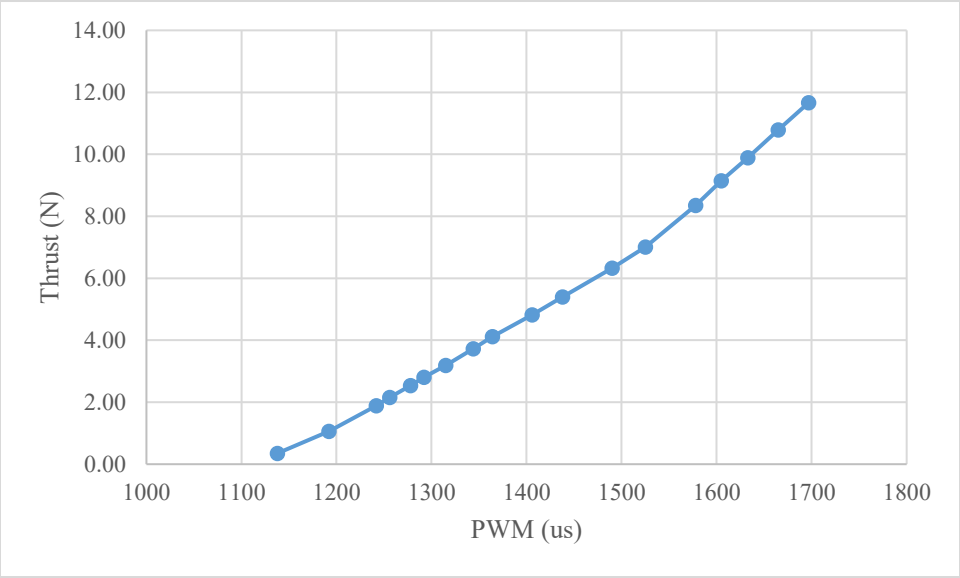


*Figure 42: Calibrated electric duct fan thrust with respect to the pulse width modulation input.*

### 3.3.3 Mooring System Design

A critical aspect of this study was the development of a mooring system that could accurately replicate the behavior of a full-scale catenary mooring system.

A helical spring system was designed to simulate the force-displacement characteristics of a catenary mooring line. A load cell was used to calibrate the mooring force, and a turnbuckle allowed for fine-tuning of the tension. The graph below shows the successful matching of the optimized spring's force-displacement curve to the target curve. **Figure 43** shows the equivalent stiffness curve and mooring angles evaluated at the platform's static equilibrium. Additionally, the pulley-guided mooring mechanism with a helical spring, shown in **Figure 44**, emulates the stiffness behavior of catenary mooring systems effectively.

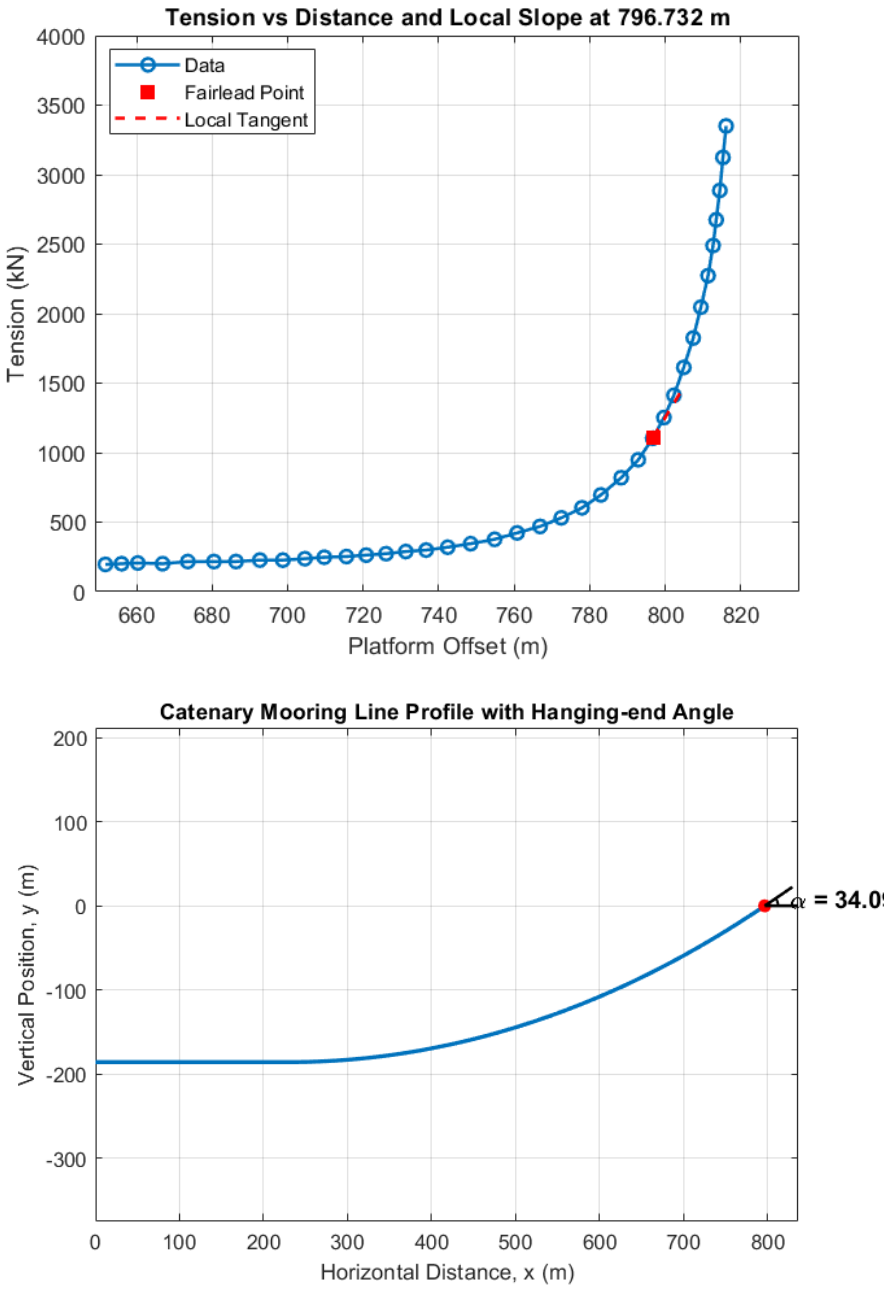


*Figure 43: Evaluation of equivalent mooring line stiffness and mooring angles at the platform's static equilibrium position.*


*Figure 44: Mechanism of the pulley-guided taut mooring setup with helical spring, used to simulate catenary mooring stiffness behavior [31].*

### 3.3.4 Instrumentation

- 4 OptiTrack PRIME 41-camera system (180 Hz) for 6-DOF rigid-body tracking.
- Three CALT S Type Load Cells DYLY-103 for mooring tension measurement
- ToughSonic TS-30S1-IV ultrasonic wave probe for free-surface elevation
- PWM-controlled electrical duct fan.
- National Instruments USB-6453 multifunction Data Acquisition (DAQ) device.

The placement and coverage of the OptiTrack PRIME 41 camera system are illustrated in **Figure 45**, demonstrating the 3D motion tracking capability used to monitor the platform and TMD motion.

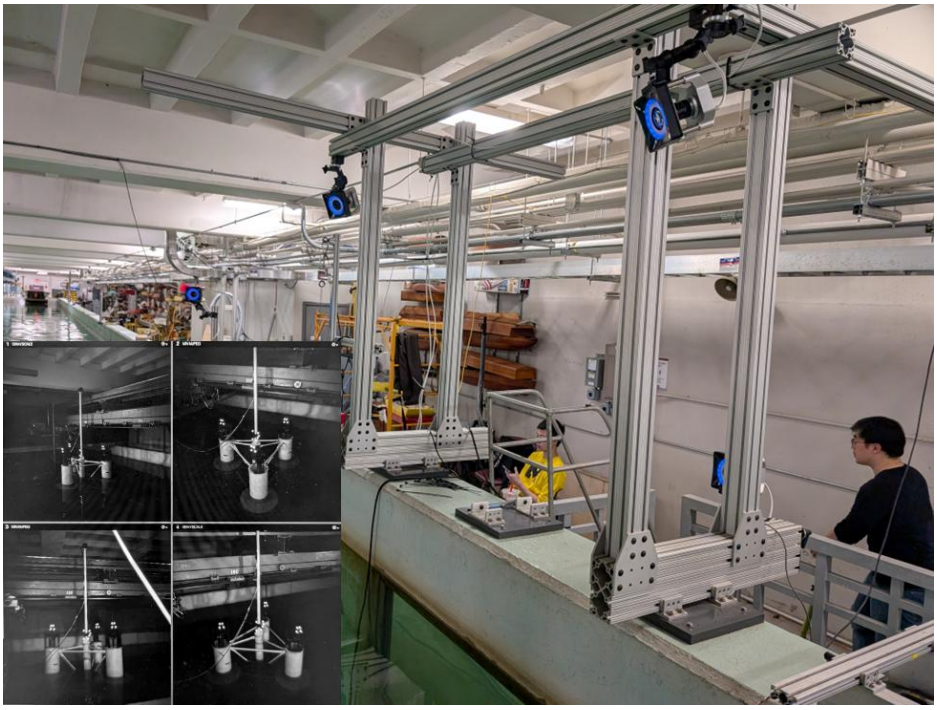

*Figure 45: 4 OptiTrack motion tracking camera and their corresponding camera view.*

### 3.3.5 Test Matrix

The scaled model was tested in the Davidson Laboratory's towing tank under various regular wave conditions. Multiple data sets were collected for a range of wave frequencies and amplitudes. This allows for a comprehensive analysis of the platform's response across different sea states.

*Table 6: Overview of wave conditions: regular waves for RAO analysis and irregular waves for design and operational load cases.*

| Number | Wave Type | Significant Wave Period (sec) | Other Parameters | Significant Wave Freq. (Hz) | Significant Wave Amplitude (m) |
|---|---|---|---|---|---|
| #1 | Regular Waves | 5.00 | | 0.2000 | 0.04 |
| #2 | | 4.31 | | 0.2319 | |
| #3 | | **3.79** | | **0.26380** | |
| #4 | | 3.33 | | 0.3000 | |
| #5 | | 2.97 | | 0.3363 | |
| #6 | | 2.68 | | 0.3725 | |
| #7 | | **2.45** | | **0.40870** | |
| #8 | | 2.25 | | 0.4438 | |
| #9 | | 2.09 | | 0.4790 | |
| #10 | | 1.95 | | 0.5141 | |
| #11 | | 1.82 | | 0.5493 | |
| #12 | | **1.71** | | **0.58440** | |
| #13 | | 1.62 | | 0.6166 | |
| #14 | | ***1.54*** | | ***0.64870*** | |
| #15 | | 1.47 | | 0.6809 | |
| #16 | | 1.40 | | 0.7130 | |
| #17 | Irregular Waves, Fan Off | **3.79** | Gamma=3.0 | **0.2638** | 0.07 |
| #18 | | **2.45** | Gamma=3.0 | **0.4087** | |
| #19 | | **1.71** | Gamma=2.2 | **0.5844** | |
| #20 | | **2.02** | Gamma=3.0 | **0.4950** | 0.105 |
| #21 | Irregular Waves, Fan On | **3.79** | Gamma=3.0 | **0.2638** | 0.07 |
| #22 | | **2.45** | Gamma=3.0 | **0.4087** | |
| #23 | | **1.71** | Gamma=2.2 | **0.5844** | |
| #24 | | **2.02** | Gamma=3.0 | **0.4950** | 0.07 |

### 3.3.6 Wave Tank Test Results

The collected data was analyzed to evaluate the performance of the TMD-enhanced platform.

#### *3.3.6.1 Platform Natural Frequency*

A key objective of the model design was to match the scaled natural frequency of the platform. The achieved natural frequency of 0.265 Hz was in excellent agreement with the desired frequency of 0.263 Hz. The Fast Fourier Transform of the platform's pitch motion is shown in **Figure 46**, confirming a sharp resonance at the target natural frequency of 0.265 Hz.

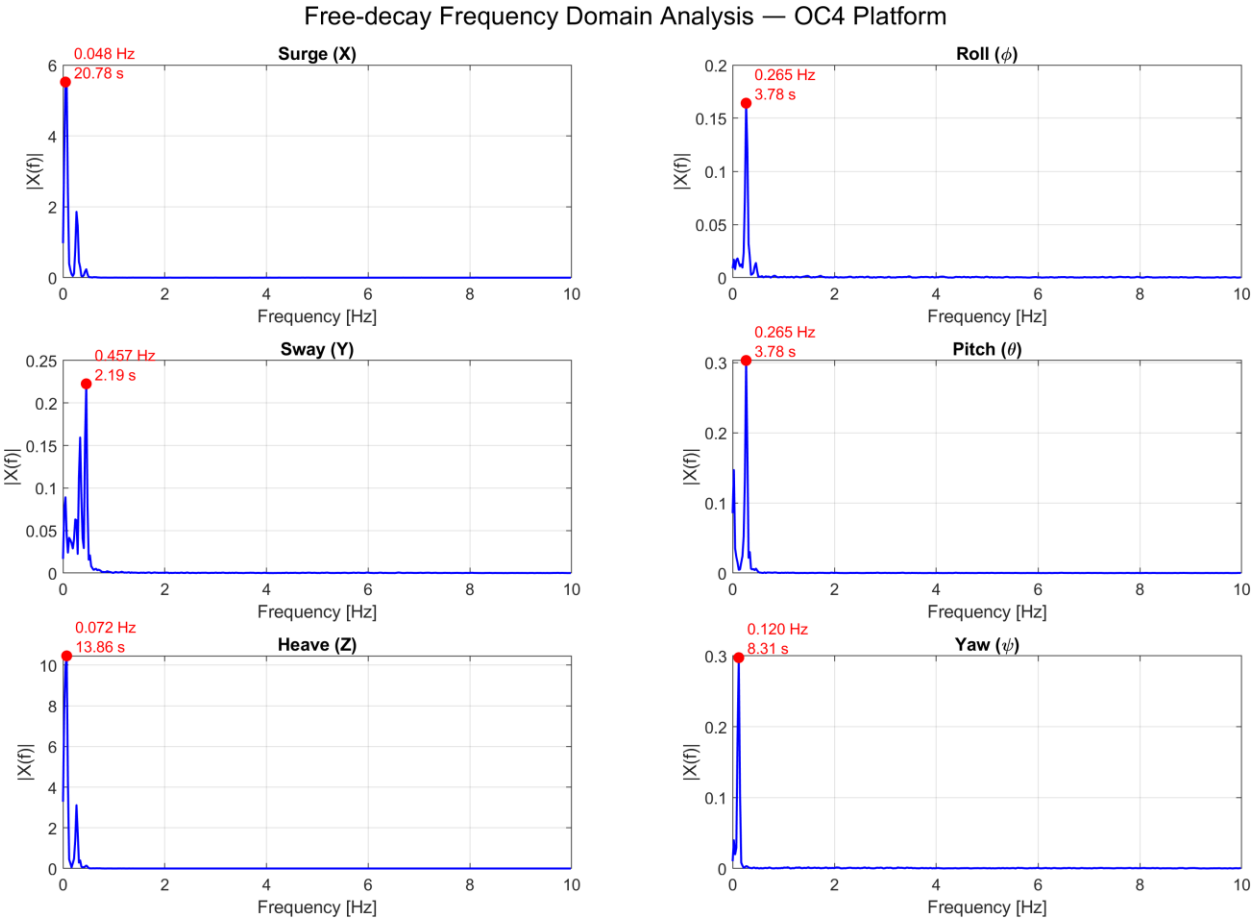


*Figure 46: Fast Fourier transform of the platform pitch free decay.*

### 3.3.6.2 Tuned Mass Dampers Configurations

To verify performance under different tuning strategies, we built two sets of three TMDs each (six total), targeting (i) the platform's heave natural frequency and (ii) the dominant wave frequency from the test matrix. This side-by-side approach lets us compare how "structure-tuned" and "sea-state-tuned" devices influence motion and loads under identical operating conditions.

All units share the same moving mass and envelope; they differ in the compliant spring stack-up to meet frequency targets and packaging constraints in the pontoon bays. Achieving the lower target (~0.3922 Hz) requires a softer effective stiffness, so we use three compliant layers in series to reduce stiffness while keeping 1095 spring steel within allowable stress and fitting the available space. Hitting the higher target (~0.6487 Hz) is possible with a single compliant layer, which provides the needed stiffness without exceeding the footprint or material limits.

**Figure 47** shows the two sets installed (three "wave-frequency–tuned" units and three "natural-frequency–tuned" units). The optimized force–displacement, apparent stiffness, and tuned-frequency-versus-stroke curves for each set are given in **Figure 48** and **Figure 49**. These curves confirm that both designs meet their frequency targets across the working stroke while respecting stress and space constraints—providing a clean A/B comparison of tuning philosophies in subsequent tests.

*Figure 47: Two TMD sets to be installed in the pontoon bays: *left, 3 units tuned to the dominant wave frequency (~0.6487 Hz) with a single compliant layer; right, 3 units tuned to the heave natural frequency (~0.3922 Hz) using three compliant layers in series.*

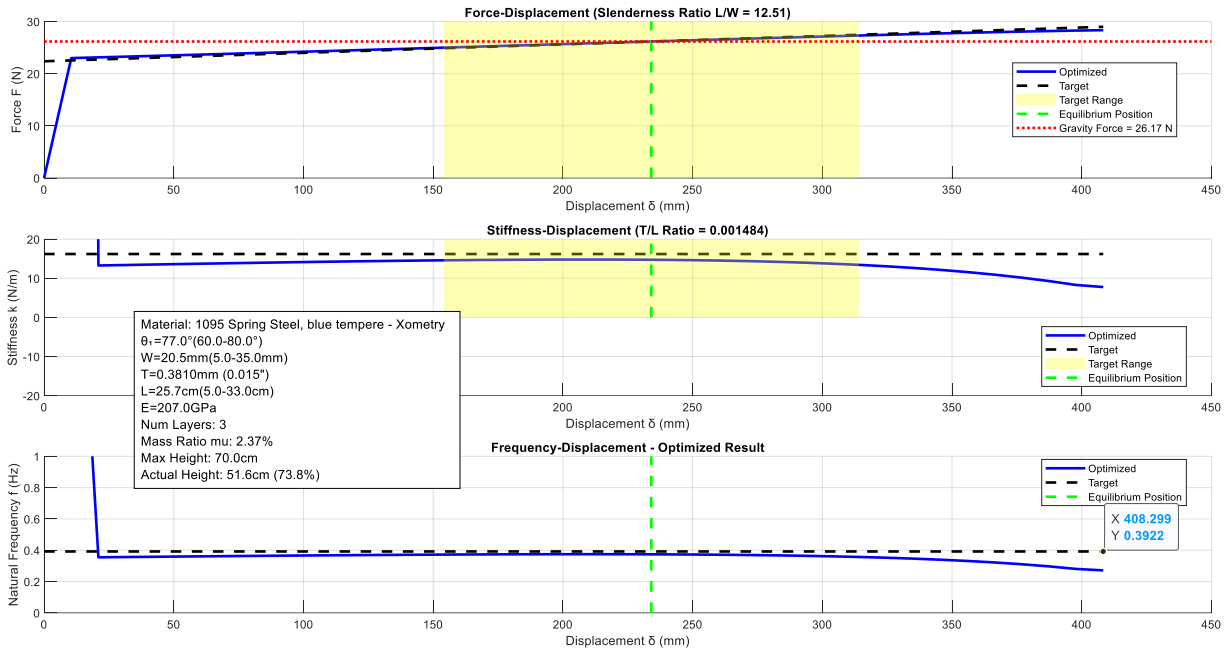


*Figure 48: Natural-frequency–tuned TMDs (~0.3922 Hz): optimized force–displacement, apparent stiffness, and inferred tuned frequency vs. stroke, achieved with three compliant spring layers to meet low-frequency, stress, and envelope constraints.*

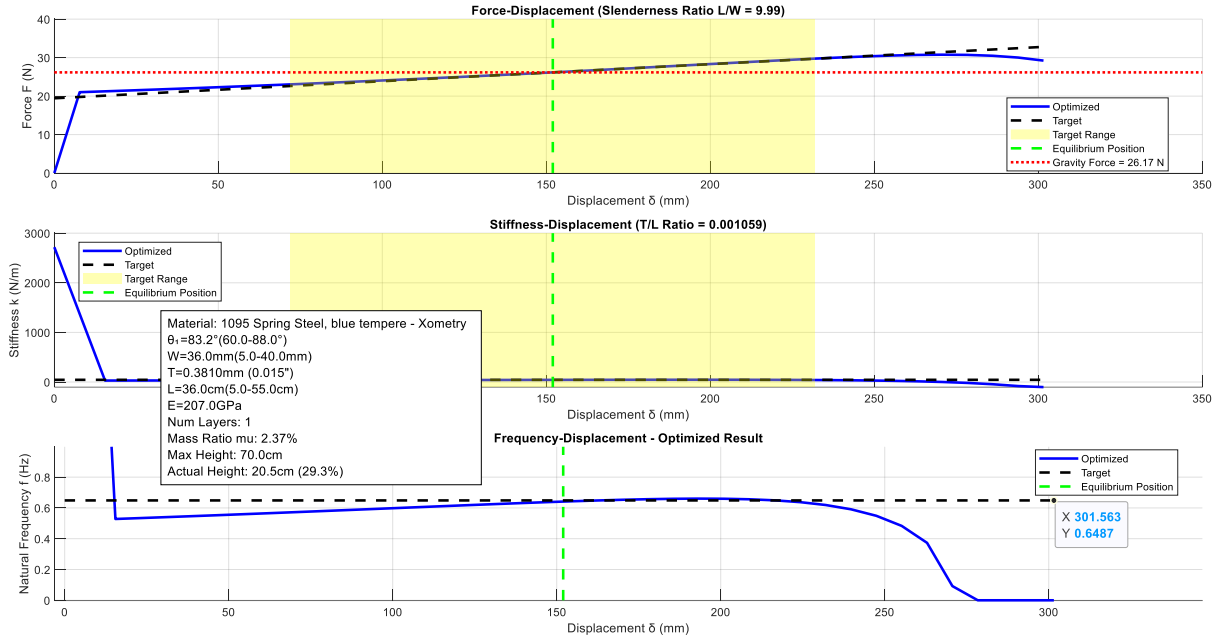


*Figure 49: Wave-frequency–tuned TMDs (~0.6487 Hz): optimized force–displacement, apparent stiffness, and inferred tuned frequency vs. stroke, achieved with a single compliant spring layer within the same envelope.*

### 3.3.6.3 Steady-State Amplitude Response Under Regular Waves

We quantified the platform's steady-state response to regular waves by sweeping the excitation frequency and extracting amplitude after transients decayed. As expected, the pitch response peaks near the platform's pitch natural frequency (0.2638 Hz). Figure 49 presents the pitch response amplitude operator (RAO) for the baseline and the two TMD configurations, making the damping effect of the absorbers apparent across the frequency range.

The natural-frequency–tuned set reduces pitch amplitude most noticeably in a band centered on 0.2638 Hz, while the wave-frequency–tuned set delivers its strongest reduction around 0.6487 Hz. In both cases, the response converges toward the baseline away from the tuned bands. Representative reductions are ≈10–30% near 0.2638 Hz for the natural-frequency–tuned set and ≈20–30% near 0.6487 Hz for the wave-frequency–tuned set, confirming effective energy absorption and damping where it matters most.

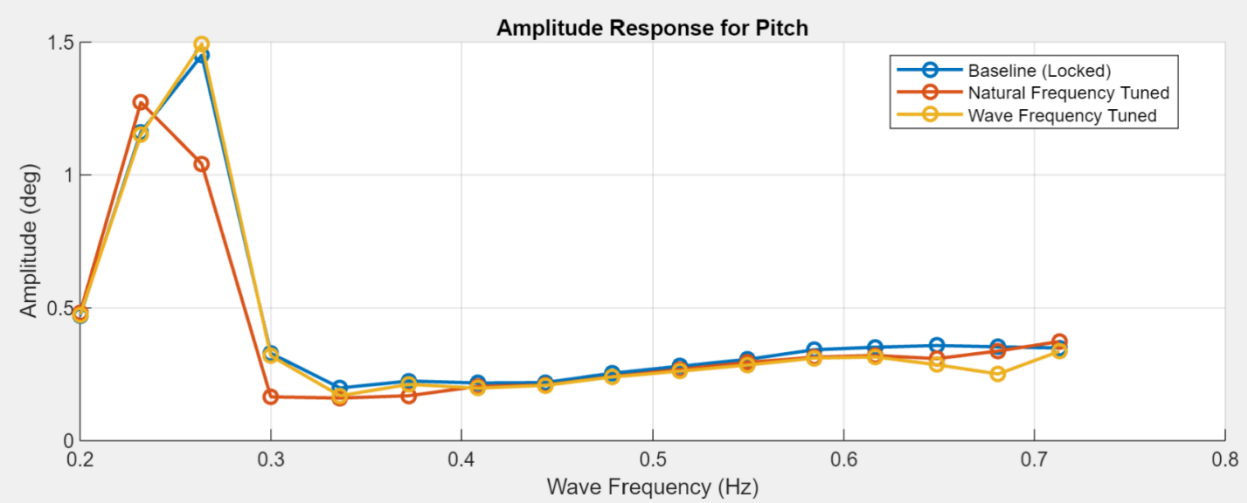


*Figure 50: Platform pitch RAO under regular waves—baseline vs. TMD configurations. The natural-frequency–tuned set yields ≈10–30% amplitude reduction near 0.2638 Hz; the wave-frequency–tuned set yields ≈20–30% reduction near ~0.6487 Hz.*

To examine how energy is exchanged between the platform and the devices, **Figure 50** and **Figure 51** plot the platform pitch amplitude together with the stroke amplitudes of the three TMDs (front, left, right). With the natural-frequency–tuned configuration (**Figure 51**), the stroke rises sharply near 0.2638 Hz, coincident with the platform's peak and the largest attenuation band. With the wave-frequency–tuned configuration (**Figure 52**), the stroke peaks shift to ~0.6487 Hz, aligning with the second reduction band in the platform RAO.

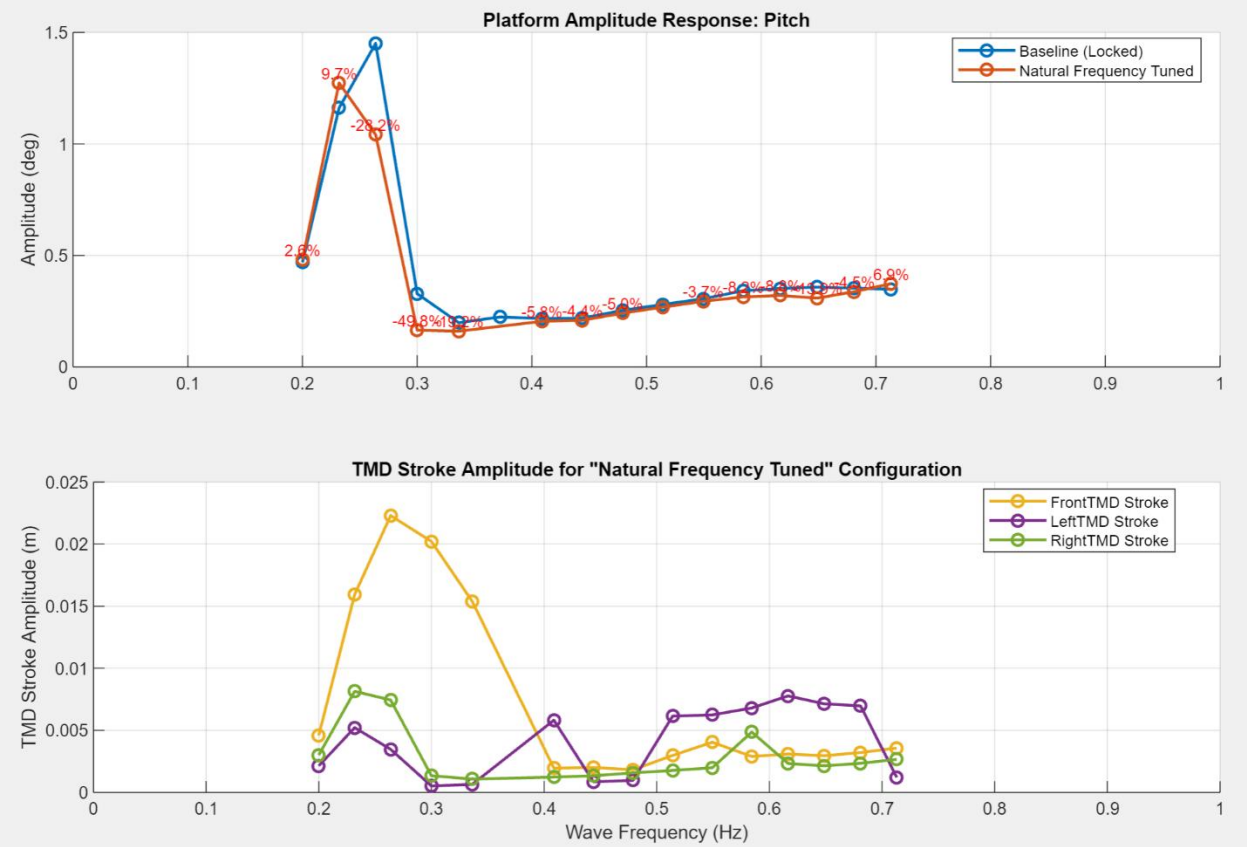


*Figure 51: Natural-frequency–tuned configuration: platform pitch amplitude and TMD stroke amplitudes vs. excitation frequency. Device strokes peak near 0.2638 Hz, coincident with the primary attenuation band.*

For the "Wave  frequency tuned" configuration (**Figure 52**), the steady-state amplitude of the front, left, and right TMD strokes escalates around  0.6487 Hz, where the OC4 platform pitch response mitigated most (around 20-30%).

Phase relations between the incoming waves and the platform motion produce asymmetries in individual device strokes across frequency. At lower frequencies, the front TMD tends to exhibit larger stroke; at higher frequencies, the left and right units often exceed the front. This behavior is consistent with the evolving phase between wave crest passage and platform pitch state and does not affect the overall reduction trends.

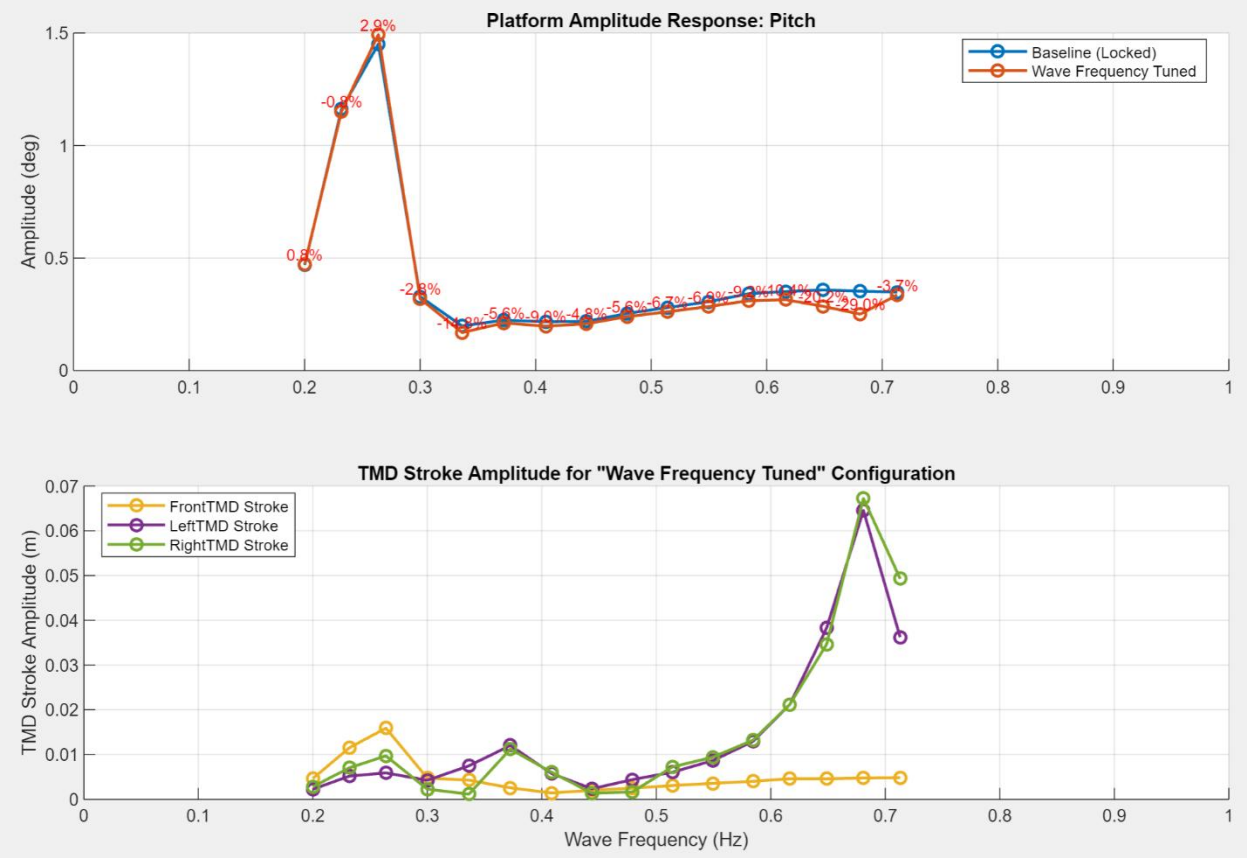


*Figure 52: Wave-frequency–tuned configuration: platform pitch amplitude and TMD stroke amplitudes vs. excitation frequency. Device strokes peak near ~0.6487 Hz, coincident with the secondary attenuation band.*

### *3.3.6.4 Irregular Wave Response*

**Figure 53** compares platform pitch in an extreme sea state for three cases: the baseline with the TMD locked, a TMD tuned to the platform's pitch natural frequency, and a TMD tuned to the dominant wave frequency. Both tuned cases reduce RMS pitch relative to the baseline (0.310°): the natural-frequency tune yields 0.307° (≈1% lower), while the wave-frequency tune achieves 0.290° (≈6% lower). The pattern holds in an operational sea state (**Figure 54**): RMS pitch drops from 0.208° (baseline) to 0.207° with natural-frequency tuning and to 0.197° with wave-frequency tuning (≈5% lower than baseline). Overall, tuning the TMD to the prevailing wave energy provides the most noticeable reduction in pitch across both conditions.

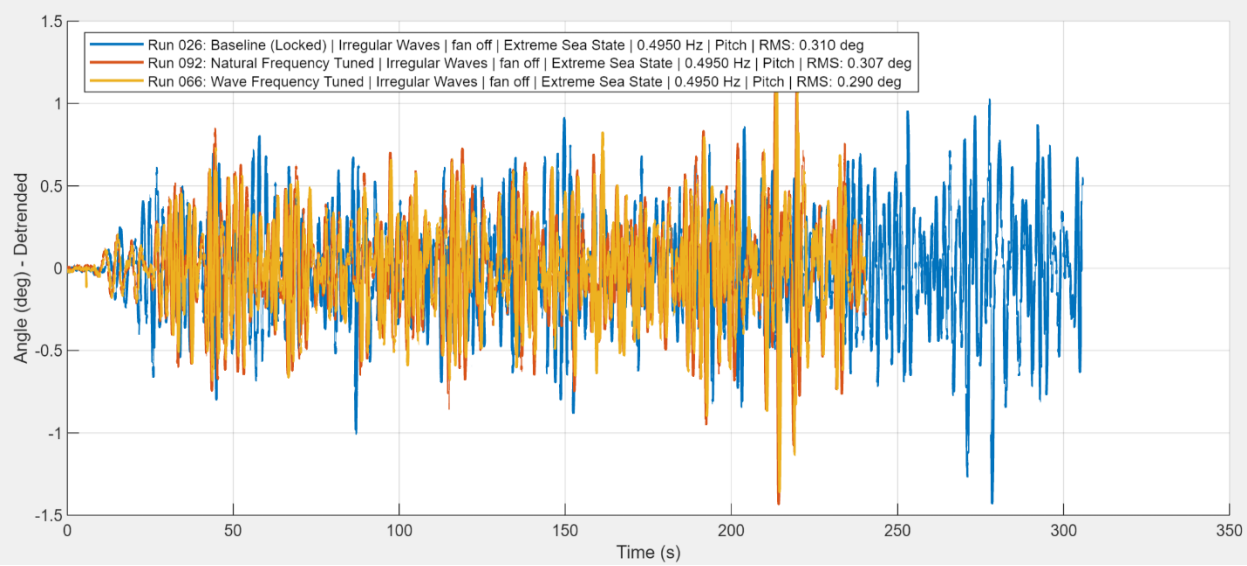


*Figure 53: Platform pitch—time-domain response in an extreme sea state. Comparison of baseline (TMD locked), TMD tuned to platform pitch natural frequency, and TMD tuned to dominant wave frequency.*

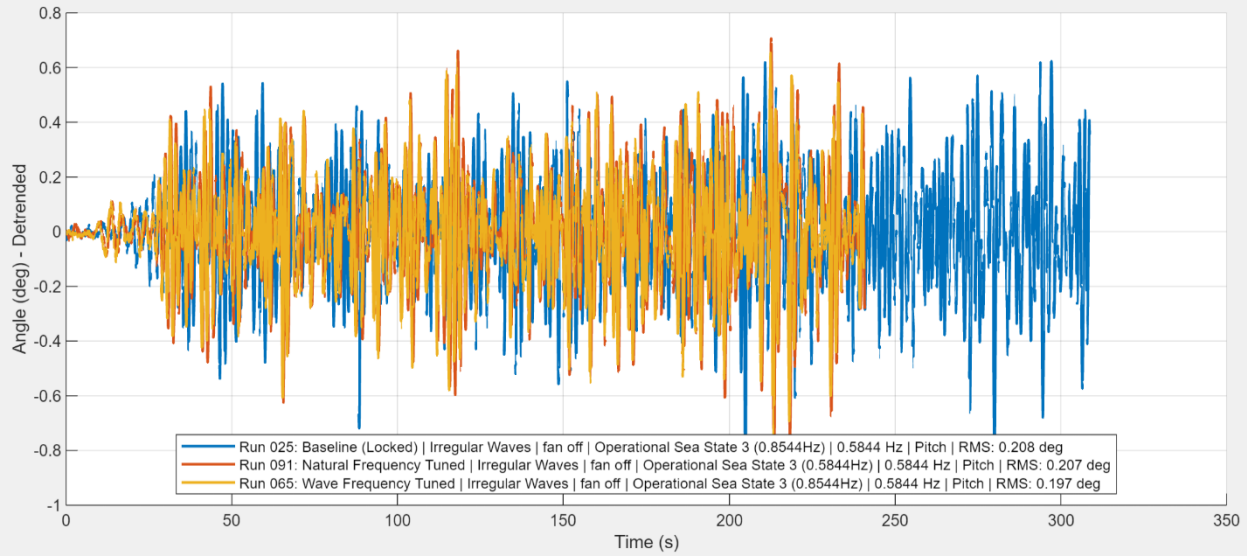


*Figure 54: Platform pitch—time-domain response in an operational sea state. Comparison of baseline (TMD locked), TMD tuned to platform pitch natural frequency, and TMD tuned to dominant wave frequency.*

### 3.3.7 Power Output Considerations of TIDs

Direct electrical measurement at 1:50 scale was not feasible: the expected output is at the milliwatt level and below the sensitivity of the tank setup. To address this, we rely on prior full-scale numerical simulations of an OC4 semi-submersible with a TID in each column. Under irregular waves with a 10 s peak period and 1% mass ratio per TID, the average total power from the three units is 5.15 kW (linear) and 6.59 kW (nonlinear), as shown in **Figure 55.**

Using Froude scaling, power scales with $\lambda^{3.5}$, so the model-scale power is

$$P_{1:50} = \frac{P_{\text{full}}}{\lambda^{3.5}}, \lambda = 50$$

Applying this to the 6.59 kW nonlinear result yields ≈ 7.5 mW at 1:50, which is consistent with our measurement limit. In the present campaign the physical TMD mass ratio is ≈ 2.7% (vs. 1% in the simulation). Even if one assumes a proportional increase in full-scale power (order-of-magnitude ~18 kW), the Froude power law still drives the model-scale signal down to 10–20 mW; readily masked by mechanical losses, sensor noise, and parasitic damping in a wave-tank environment. Consequently, electrical power measurement is omitted, and simulated power is reported to document expected levels.

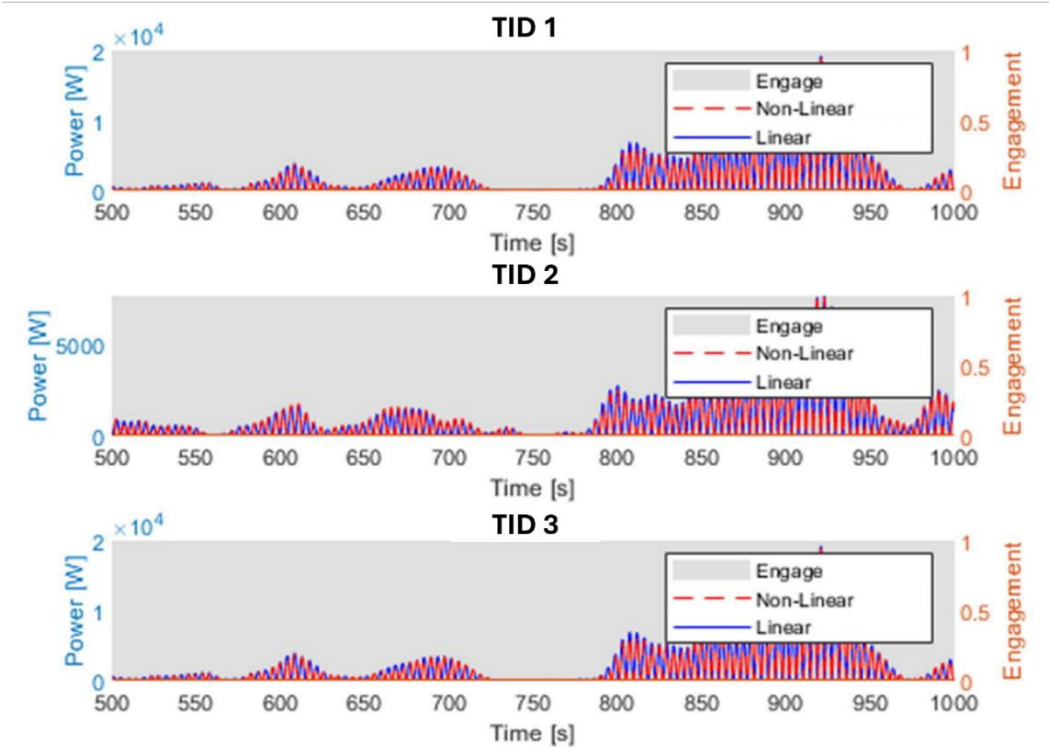


*Figure 55: Power generation of TIDs in a full-scale OC4 semi-submersible platform under 10 s period of irregular wave excitation.*

# 4 Techno-Economic Analysis and New Technology Introduction Plan

## 4.1 Techno-Economic Analysis

### 4.1.1 Scope and Baseline

This analysis evaluates how installing three tuned inerter dampers (TIDs)—one in each outer column of a semisubmersible—affects levelized cost of energy (LCOE) for a 15 MW GE Vernova Haliade-X–class floating turbine. The TIDs are tuned to suppress platform motions that drive loads and curtail energy capture; the same hardware can also harvest small amounts of wave-induced energy. The refined work here builds on the preliminary LCOE flowdown and updates all key assumptions based on technology progress and recent market context.

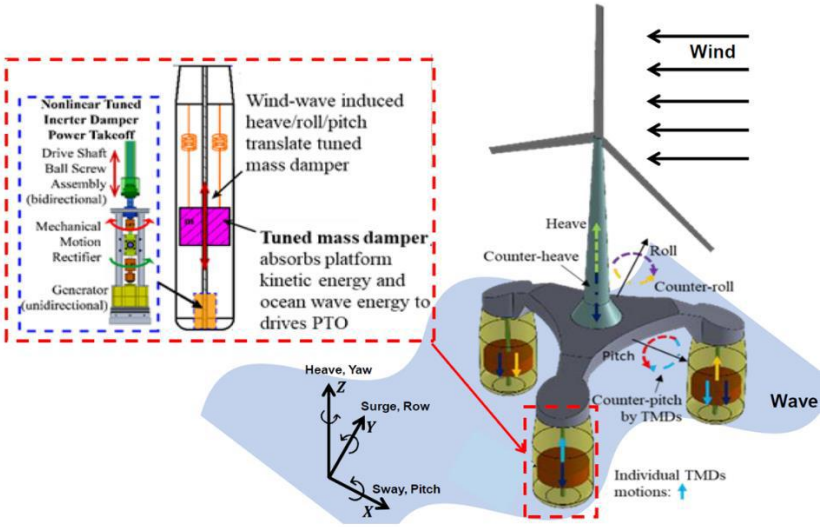


*Figure 56: Applying TID to a semi-submersible floating wind turbine.*

### 4.1.2 Market Benchmark and LCOE Target

Industry benchmarks indicate today's (2024) floating LCOE around **$181/MWh**, with wide uncertainty in the out-year trajectory. Looking ahead to 2035, the range expected by public benchmarks is $62–$122/MWh depending on policy, supply-chain maturity, and deployment speed. To stay conservative—and in light of recent project headwinds—we target the upper bound **($122/MWh**) as the 2035 baseline for this study.

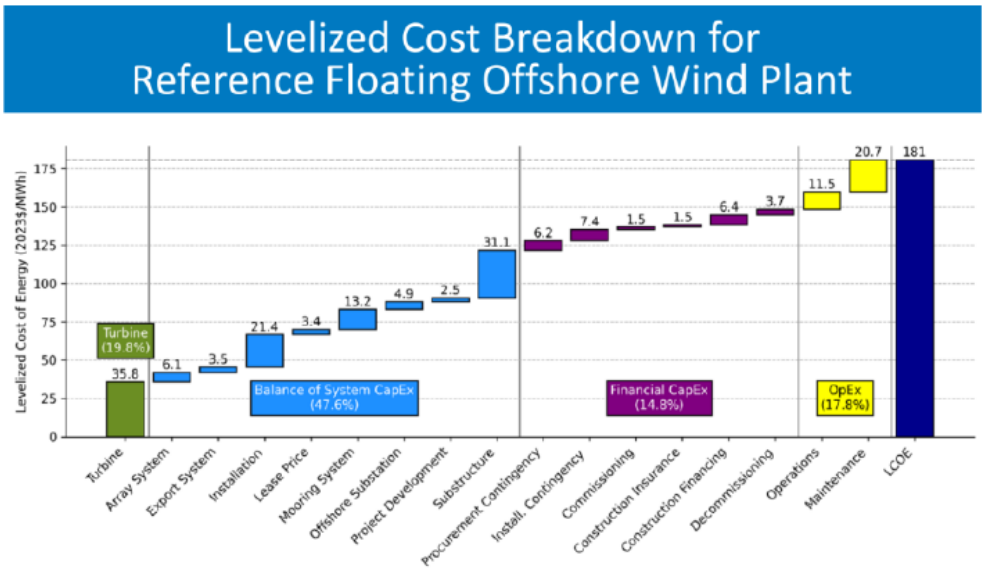


*Figure 57: LCOE breakdown reported by NREL [32].*

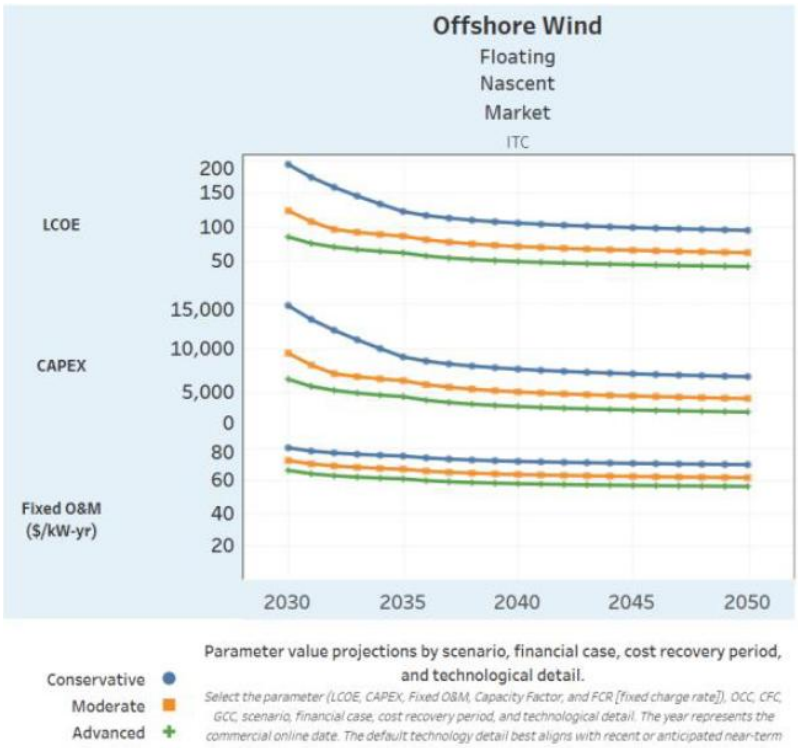


*Figure 58: Floating wind cost reported in [33].*

### 4.1.3 Impact on Annual Energy Production (AEP)

1. Capacity factor

   Because floating farm data are still limited for 15 MW-class turbines, we adopt a 56% capacity factor (CF) as a prudent planning value (noting that early floating projects have reported higher CFs in specific conditions).

2. TID generator power prediction

   Using time-series simulations scaled from an OC4-5 MW reference (see **Figure 55**), the average electrical output from the three TIDs is ~27 kW for the 15 MW turbine—small compared with the main generator and strongly limited by very low wave frequencies. This keeps expectations realistic: the TIDs' primary value is motion suppression, with energy harvest as a minor bonus.

3. Motion-to-energy linkage

   Platform pitch is the key driver of energy loss around rated wind speed: static tilt reduces effective rotor area, while dynamic pitch forces the controller off optimal operating points. Published performance maps indicate up to ~14% energy loss from pitch effects (combined static and dynamic) for large turbines on floating foundations [34]. With properly tuned TIDs, pitch energy near the platform's natural frequency can be substantially reduced; adopting a ≥30% reduction in pitch spectral energy yields an AEP gain of ~4.2% for the primary turbine.

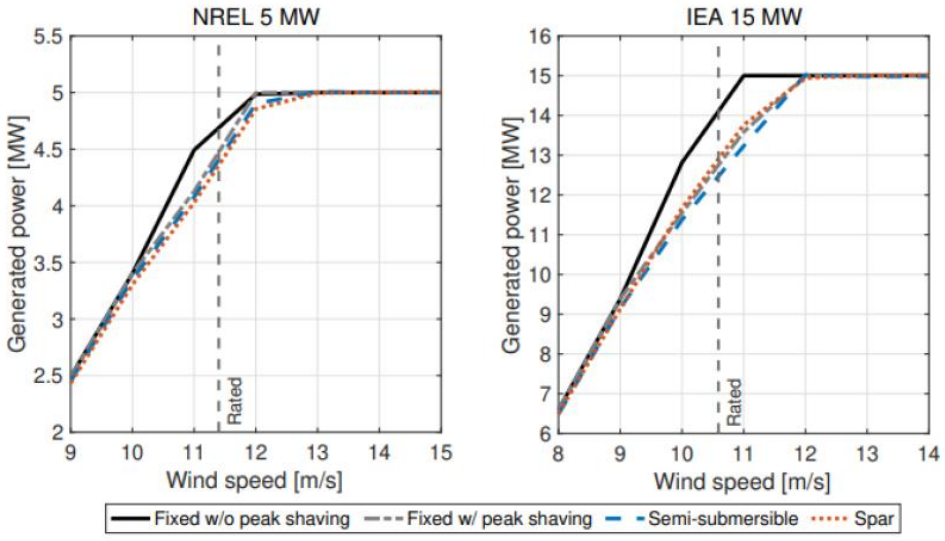


*Figure 59: Impact of Floating Platform on Power Curves in [34].*

### 4.1.4 Impact on Capital and Operating Costs

1. Capital Expenditure (CapEX)

   Floating platforms experience elevated fatigue relative to fixed-bottom designs (see **Figure 4**), therefore reducing motion helps. Based on the project's motion-reduction results, we carry a ~10% decrease in damage-equivalent loads (DEL) on average across load-critical locations. Because not every component is fatigue-limited, we conservatively realize ~5% turbine CapEX reduction. For the balance of plant, we include a ~3% CapEX increase to account for TID mass/integration and added installation tasks, which keeps the net capital impact modest and traceable.

2. Operation Expenditure (OpEX)

   As shown in **Figure 57,** OpEX consists of costs of operation and maintenance. We will keep the operation cost intact. Following the same 10% DEL reduction, we will calculate the implication of the DEL reduction to the component lives.

   For most metal components, we will have the following equation,

   $$DEL^m \; Cycles = const.$$

   Where m is a material parameter derived from S-N curve and is related to the material fatigue strength. For most of steels, m ranges from 3 to 5, we will use $m = 4$ in the calculation. Based on DEL reduction, we calculated the component life increase by 52%. Again, not all component designs are driven by the fatigue. We will assume 26% of the life increase, therefore corresponding reduction in maintenance requirement.

### 4.1.5 LCOE Outcome

**Figure 60:** showed refined LCOE calculation based on updated power generation, AEP calculation, CapEX update and OpEX estimation. The technology can potentially reduce LCOE by 7.8%.

Compared to the preliminary LCOE analysis, the percentage of the impact is lower. Our baseline LCOE prediction of year 2035 has been shifted to the more pessimistic end, from $63/MWh to $122 /MWh. This reflects recent slowdown in the US offshore wind market, the challenge in suppler chain, and change of government policy. The main benefit of the technology is in the AEP increase by suppressing vibration of

the platform, which is reflected in the LCOE calculation. The benefit of the OpEX is also substantially, potentially even more that what we estimated here. The additional power generation from the TID technology is significantly less compared what we expected in the preliminary study. Overall, the benefit of employing the technology is still a substantial step toward making floating offshore wind technology to the parity of the fixed bottom turbines.

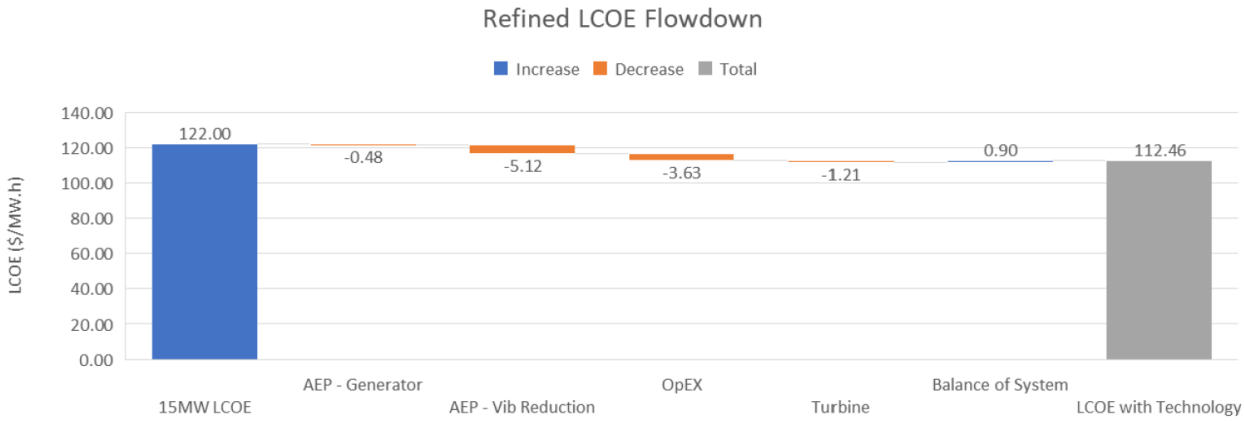


*Figure 60: Refined LCOE Flowdown.*

## 4.2 New Technology Introduction Plan

### 4.2.1 Overview of NTI Process

New Technology Introduction is an internal process deployed by GE Vernova to mitigate the technical and commercial risks. In general, it consists of 4 steps:

NTI-1 determines whether the team is ready to go develop this technology: boundaries and requirements known and expectations realistic

NTI-2 demonstrates feasibility and is ready to proceed to development and down select.

NTI-3 verifies the down select and the maturing of the technology

NTI-4 verifies the readiness for handoff to NPI.

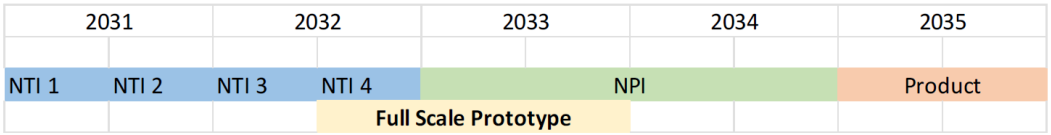


*Figure 61: NTI Timeline and Key Milestones*

We anticipate minimum 2 years of NTI period, toward the end, a full-scale prototype will be deployed, which will serve as a milestone for risk mitigation.

### 4.2.2 Technology Evaluation

We will evaluate key mechanical components in the nonlinear TID design, focusing on cost and reliability. The details of the nonlinear TID design can be found in the Appendix.

#### *4.2.2.1 Generator*

At system level, the TIDs deliver ~27 kW average on a 15 MW turbine; we size the drivetrain as 3 × 10 kW modules (sensitivity 7.5–25 kW per column). For each module we track torque, mass, and cost using established scaling relations to compare direct-drive and geared concepts. **Table 7** summarizes the resulting torque and power for the chosen range.

*Table 7: TID Power and Torque*

| | | |
|---|---|---|
| Vertical Movement | 10 | m |
| Wave Period | 10 | s |
| Wave Frequency | 0.1 | Hz |
| Wave Height | 3 | m |
| | | |
| Linear Speed | 1 | m/s |
| | | |
| Rotation Shaft OD | 76.2 | mm |
| Shaft RPM | 250.6377 | RPM |
| Shaft Rotation omega | 26.24672 | Rad/sec |
| | | |
| Total Power | 30 | Kw |
| Power /per Column | 10 | Kw |
| Max Power/per Column | 20 | Kw |
| Rate Torque/Per Column | 381 | N.m |
| Max Torque/per Column | 762 | N.m |

#### 4.2.2.2 Mechanical Motion Rectifier (MMR)

MMR converts bidirectional vibration motion into one direction rotation. The device has been designed and analyzed by the VT team for wave energy harvest [12]. MMR used two opposing direction one-way clutches and a bevel gear (as shown in **Figure 62**) to engage and disengage the generator, so the generator will use previous stored energy when the input energy is low.

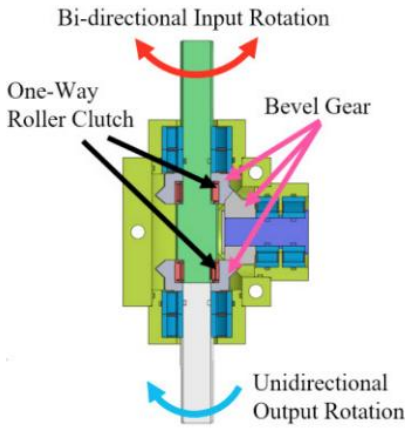


*Figure 62: Passive MMR [35].*

While MMR is effective in converting motion induced by wave energy, the design did introduce a level of complexity. For a 10KW system, VT reported cost of $7k. We anticipated the cost to be at least halved when moving to large quantity production. In the study, we will use $3.5K for the production cost.

#### 4.2.2.3 Gearbox

A potential low gear ratio gearbox combined with the generator may be needed to increase the efficiency of the generator. As seen in **Table 7**, without gearbox, the shaft rotates at about 250 RPM, which is low for the generator. We expect a low gear ratio gearbox, for example, gear ratio at 3, will enhance the generator performance and provide a cost benefit as the gearbox will reduce the torque in the generator.

A preliminary planetary gear system has been conceptualized, as shown in **Figure 63**, with following pitch radii:

(1) Ring gear, Rr = 101.6 mm (stationary gear)
(2) Planetary gear, Rp = 76.2 mm (with a carrier connecting all 3 gears, low speed shaft)
(3) Sun gear, Rs = 50.8 mm (high speed shaft)
(4) Gear width = 12.7 mm

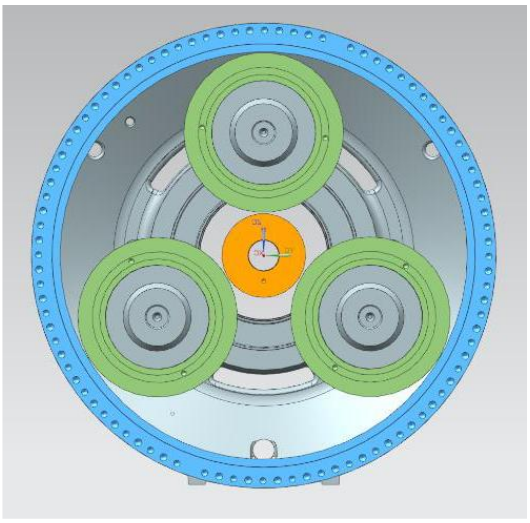

*Figure 63: Schematic of a planetary gear.*

Gearboxes are typically made from high-strength, wear-resistant alloy steels. Common choices include 42CrMo4 (EN 10083) and 34CrNiMo6 (EN 10083), or their equivalents like AISI 4140 and 4340, respectively. These steels are selected for their ability to withstand high torque, cyclic fatigue, and harsh environmental conditions. Heat treatment processes like carburizing or nitriding are often applied to enhance surface hardness and wear resistance. In this study, we will assume 4140 steel with tensile strength = 700 MPa and yield stress = 450 MPa.

We are targeting numbers of teeth for each gear,

(1) Nr = 20
(2) Np = 15
(3) Ns = 10

Therefore, the gear ratio can be determined based on follow equation (assuming fixed ring gear):

Gear Ratio = (Nr+Ns)/Ns = 3

When considering moment equilibrium, note how the fact that there are three planets engaging with the sun gear means that the total tooth force that each planet gear exerts on the sun gear (and vice versa) has effectively been split in three. The total sun-planet tooth forces for a three-planet planetary gear set turn out to be as follows:

$$F_{ps} = \frac{T_i}{3 * 0.5 * Ns * m * cos\emptyset} = 5.3\ KN$$

Where $m$ is the module of the sun gear and defined as $m = 2*R_s/N_s$; $cos\emptyset$ is the cosine of the pressure angle of the contact point on the tooth profile, usually between 14.5 and 20 degrees. Ti is the max torque anticipated in the design, 762 N.m as shown in **Table 7**.

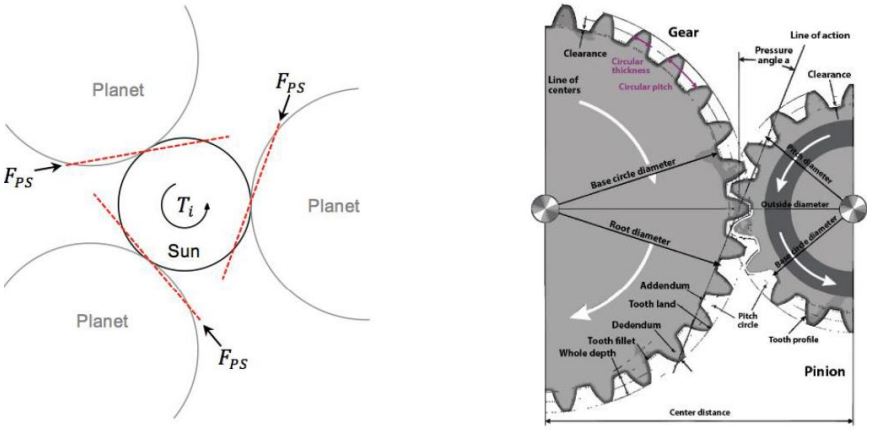


*Figure 64: Schematic of force acting on sun gear/planetary gear.*

We then calculated the max bending stress of the tooth based on Lewis formula:

$$\sigma_t = \frac{F_{ps} * cos\emptyset * P_d}{w * Y}$$

Where $P_d$ is the diametral pitch (1/inch); w is the bearing width (inch); and $Y$ is the Lewis form factor which is dimensionless.

We calculated the max bending stress to be around 30 MPa, which is a very conversative design. A more detailed stress analysis including Hertzian contact pressure is needed for further design. We expect no repair or maintenance for the gearbox design.

We can then estimate the total mass and cost of the gearbox:

| | Mass | |
|---|---|---|
| Sun gear | $0.78 | kg |
| Planetary | $5.27 | kg |
| Ring Gear | $0.78 | kg |
| Carrier | $0.20 | kg |
| | | |
| **Total mass** | **$7.03** | **kg** |
| **Total cost** | **$140.58** | **$** |
| **Torque Density** | **$54.20** | **Nm/kg** |

#### *4.2.2.4 Drivetrain Down-Select and Cost Result*

We will examine three drivetrain configurations:

(1) Geared MMR + Generator

(2) Direct Drive Generator

(3) Planetary Gear + Generator

All three configurations will require a linear to rotatory motion gear system, either a rack and pinion or a ball screw, both of which are mature, highly reliable and very cost effective. For the full-scale system, rack and pinion may be better for longer travel, more rugged and heavy loads. However, since this system will be appliable to all three configurations, we will not include it in the comparison.

**Table 8** listed mass and cost of all three options. It is evident that the Option 1 (MMR) is the most expensive and the Option III (Gearbox + Generator) is the most cost effective. Please note that the table lists mass and cost per column. The total needs to be multiplied by three. The table also compares options with varying rated power, as shown in **Figure 65**. The cost difference appears to be even bigger as the rated power increases.

*Table 8: Drivetrain Mass and Cost Comparison*

| | Rated P | W | 7500 | 10000 | 12500 | 15000 | 17500 | 20000 | 22500 | 25000 |
|---|---|---|---|---|---|---|---|---|---|---|
| | Mass/ per kg | W/kg | 240.91 | 240.99 | 241.08 | 241.17 | 241.26 | 241.35 | 241.44 | 241.53 |
| | Cost coefficient | $/W | 0.03 | 0.03 | 0.03 | 0.03 | 0.03 | 0.03 | 0.03 | 0.03 |
| | Mass | kg | 31.13 | 41.49 | 51.85 | 62.20 | 72.54 | 82.87 | 93.19 | 103.51 |
| Geared Generator | Cost | $ | 262.20 | 349.47 | 436.67 | 523.81 | 610.88 | 697.88 | 784.82 | 871.69 |
| MMR | Cost | $ | $2,625.00 | $3,500.00 | $4,375.00 | $5,250.00 | $6,125.00 | $7,000.00 | $7,875.00 | $8,750.00 |
| **Total** | **Cost** | **$** | **$2,887.20** | **$3,849.47** | **$4,811.67** | **$5,773.81** | **$6,735.88** | **$7,697.88** | **$8,659.82** | **$9,621.69** |
| | | | | | | | | | | |
| Direct Drive Generator | Torque | N.m | 247.47 | 381.00 | 532.46 | 699.94 | 882.03 | 1077.63 | 1285.88 | 1506.03 |
| | Mass | kg | 49.49 | 76.20 | 106.49 | 139.99 | 176.41 | 215.53 | 257.18 | 301.21 |
| | **Cost** | **$** | **$613.72** | **$944.88** | **$1,320.51** | **$1,735.86** | **$2,187.43** | **$2,672.52** | **$3,188.97** | **$3,734.97** |
| | | | | | | | | | | |
| | Torque | N.m | 82.49 | 127.00 | 177.49 | 233.31 | 294.01 | 359.21 | 428.63 | 502.01 |
| Direct Drive with 1:3 Gear Generator | Mass | kg | 16.50 | 25.40 | 35.50 | 46.66 | 58.80 | 71.84 | 85.73 | 100.40 |
| | Cost | $ | $204.57 | $314.96 | $440.17 | $578.62 | $729.14 | $890.84 | $1,062.99 | $1,244.99 |
| 1:3 Gear box | Mass | kg | 4.57 | 7.03 | 9.82 | 12.91 | 16.27 | 19.88 | 23.72 | 27.79 |
| | Cost | $ | 136.97 | 210.89 | 294.72 | 387.42 | 488.21 | 596.47 | 711.74 | 833.60 |
| Total | **Cost** | **$** | **$341.55** | **$525.85** | **$734.89** | **$966.04** | **$1,217.35** | **$1,487.32** | **$1,774.73** | **$2,078.59** |

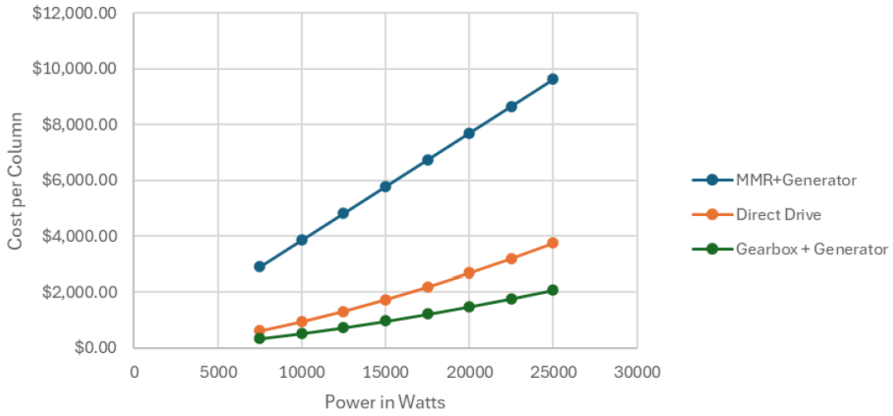


*Figure 65: Cost Comparison for Each Column*

## 4.2.3 Risks and Mitigation

### *4.2.3.1 Springs (Risk level: high)*

The wave induced motion has very low frequency, typically in the range of 0.1-0.3 Hz. This required TMD springs to be very soft. In the 1/50 scale wave tank test, the design employed two thin buckled spring, as shown in **Figure 66**. The design parameters for the wave tank design are:

- Material: 1095 Spring Steel, blue temper – Xometry
- Elastic Modulus (E): 207 GPa
- $\theta_1$: 83.1688°
- Width: 36.0129 mm
- Thickness: 0.3810 mm
- Length: 35.9858 cm

- Mass Ratio: 0.0237
- Number of Layers: 1
- Slenderness Ratio: 9.9925
- Thickness-to-Length Ratio: 0.0011
- Material stress during deformation: 330 - 633 MPa

For the full scale, if we use the single layer design instead of stacking of multiple parallel layers, we can use the scaling law to estimate the dimensions:

- To maintain dynamic similarity under Froude scaling, the total spring stiffness should follow: $k_{total} \propto \lambda^2$, with $\lambda = 50$.
- For a leaf-type compliant spring: $k \propto E \times b \times t^3 / L^3$
- If length L and width b scale geometrically with $\lambda$, then thickness must scale slightly faster: $t \propto \lambda^{(4/3)}$

This means the full-size dimensions will be:

- Length ~ 18m
- Width ~ 1.80m
- Thickness ~ 66 mm
- Materials: same (1095 spring steel)
- Angles and ratios: retain original angles and ratios.

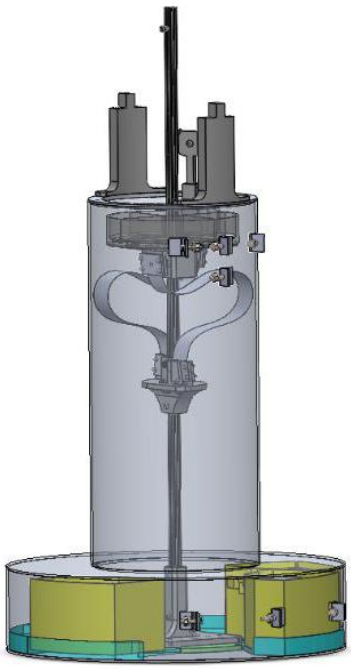

*Figure 66: TMD design for 1:50 OC4 semisubmersible floating platform.*

The above scaling keeps the stiffness. However, the stress will in increased as stress grows as λ^1/3. Therefore, the stress at full-size will be in the order of 1.2-2.3 GPa. Most likely, this level of stress requires a new multi-layer design. There is also uncertainty in the constant spring range as the design requires the spring stiffness to be relatively constant across the movement range. Finally, the material corrosion behavior needs to be studied for long term oceanic environment.

Analysis, testing, and long-term environment exposure will be needed to further the spring design during the NTI.

#### *4.2.3.2 Sliding Mechanism (Risk level: high)*

With limited space and existing ballast water inside the column, there are limited mechanical options for the TMD mass to move freely without much friction. In the wave tank test, a linear ball bearing was used as the guiding system for the mass to move vertically, as shown in **Figure 67**. We spent a lot of time to design the system which is well balance therefore minimizing the friction. We also selected the correct bearing beads for the right friction.

*Figure 67: TMD mass and guiding system in wave tank test.*

However, this sliding mechanism may not work with the full-size system. One of the challenges is the high risk of corrosion which may drastically alter the friction characteristics of the materials. The other risk involves the reliability of the linear bearing system. For 25–30-year design life, a secondary lubrication system may to be needed, which potentially requires lubrication pump and maintenance.

#### *4.2.3.3 Installation (Risk level: medium)*

Depending on the ballasting sequence, the TMD mass and spring system can be potentially pre-installed. However, the electric converter, generator and cabling may need on-site assembly and installation. The generator and converter (if the converter is positioned inside) cables will need penetration to the column. The installation procedure needs to be carefully crafted and documented in the NTI.

#### *4.2.3.4 Electric Connection (Risk level: medium)*

The power from TID generator will be converted and combined with main turbine electric system. The TID generator may have different voltage from the main turbine generator. A new AC-DC bus system may be needed to combine powers. The electric system is NOT in the scope of the current study and needs to be addressed during the NTI.

### 4.2.4 Sustainability

One of the main activities in the NTI is to assess sustainability impact and carbon footprint of the new technology. There are many factors to address when it comes to sustainability, there factors are listed below:

1. Manufacturing

- In 4.1.3, we estimated the AEP increase due to vibration suppression is about 4%. For an equivalent turbine producing about same amount of energy, the manufacturing cost of the system can potentially be lowered by at least same percentage.
- The DEL decrease can potentially reduced turbine cost by about 5%, as estimated in 4.1.4
- The balance of system will be more expensive, by 3% of additional mass from TMDs.
- TID main component costs are very low, much less than 0.5%, as shown in **Table 8**. Many can be procured with standard components.
- Overall, for an equivalent turbine, the manufacturing cost can be reduced by more than 5%.

2. Logistics

- Again, for an equivalent turbine, the transport cost is reduced by 5%.

3. Installation

- Installation cost will be more when the TIDs are added to the system. A more detailed installation procedure needs to be developed. We estimated the additional installation is about 1%.

4. Operation and Maintenance

- Operation cost is about same as reference unit
- Maintenance cost can potentially be reduced by 26% as shown in 4.1.4.

5. Decommissioning

- Decommissioning is essentially a reversed installation, therefore the TIDs will likely cost more to remove.

6. Recycling

- Not much difference from a standard offshore turbine.

### 4.2.5 NTI Focus

During the NTI, the focus will be

1. Addressing and mitigating main risks identified in the study.

2. Design a full-size prototype. The installation of prototype is a critical step to mitigate risks and move the technology toward the NPI.
3. Suppliers need to be identified and qualified for TIDs and structure components.

Overall, from the LCOE and sustainability analysis, the impact of the technology is very positive. LCOE and sustainability should be further verified during the prototype installation and operation.

# 5 Concluding Remarks

This work demonstrates that column-integrated passive absorbers—TMDs and inerter-augmented TIDs—can materially reduce the motions that drive loads and energy losses in semisubmersible floating wind turbines. Using a coordinated modeling and testing campaign, we showed that tuning to the platform's natural pitch band yields the largest reduction at resonance, while tuning to the prevailing wave frequency provides complementary attenuation where incident-sea energy is concentrated. In both simulation and scaled testing, steady-state amplitude reductions on the order of 10–30% were observed near the targeted bands, and time-domain responses settled significantly faster than the baseline following a disturbance. When mass efficiency is a constraint, TIDs offer a practical path to TMD-level (or better) performance with less physical mass by leveraging inertance.

Methodologically, the combination of a reduced-order model for optimization and OpenFAST for verification proved effective. The ROM accelerated convergence on viable designs and consistently preserved the ordering of alternatives, while OpenFAST provided high-fidelity confirmation and clarified model sensitivities (e.g., mass/ballast accounting and Jacobian refresh cadence). On the hardware side, we validated a low-friction compliant spring-and-guide concept based on inclined fixed-guided beams. Large-deflection modeling (CBCM), literature-based verification, and optimization produced force–displacement characteristics matching the very low target frequencies within realistic stress and packaging limits—an essential enabler for column-integrated absorbers.

From a system perspective, the techno-economic analysis indicates that the principal value of these devices is motion suppression that improves turbine operation (AEP) and extends fatigue life (maintenance savings). While TIDs can generate electrical power, the magnitude at platform frequencies is small relative to the main turbine and should be treated as a secondary benefit. Under conservative 2035 cost assumptions, the integrated package delivers a ~7.8% reduction in LCOE, strengthening the business case for further development.

There are important limitations and priorities for follow-on work. The wave-tank campaign focused on TMDs; full-scale-relevant demonstrations of TIDs (including drivetrain and power electronics) remain to be executed. Compliant springs and linear guidance are critical-risk components at scale, requiring materials selection, corrosion mitigation, and lifetime testing. Electrical integration (bus architecture, protection, and controls) and installation procedures must be matured for offshore deployment. Finally, broader operating envelopes—combined wind-wave loading, misalignment, and controller co-design—

should be exercised against the IEC design load cases to quantify lifetime benefits and refine the economic picture.

The proposed NTI plan addresses these gaps through gated maturation, supplier engagement, and a full-scale prototype as the capstone risk-reduction step. With those actions, tuned absorbers—particularly inerter-enabled variants—offer a practical, low-complexity pathway to calmer platforms, higher energy yield, and lower lifecycle cost for floating offshore wind.

# 6 References


[1] W. Musial *et al.*, "Offshore Wind Market Report: 2022 Edition," 2022.

[2] C. Draxl, A. Clifton, B.-M. Hodge, and J. McCaa, "The Wind Integration National Dataset (WIND) Toolkit," *Appl. Energy*, vol. 151, pp. 355–366, Aug. 2015, doi: 10.1016/j.apenergy.2015.03.121.

[3] "Overview of Floating Offshore Wind (Text Version) | NREL." Accessed: Sep. 07, 2025. [Online]. Available: https://www.nrel.gov/news/video/overview-of-floating-offshore-wind-text

[4] A. Robertson and J. Jonkman, "Loads Analysis of Several Offshore Floating Wind Turbine Concepts".

[5] H. Frahm, "Device for damping vibrations of bodies," US989958A, Apr. 18, 1911 Accessed: Oct. 09, 2024. [Online]. Available: https://patents.google.com/patent/US989958A/en

[6] S. Elias and V. Matsagar, "Research developments in vibration control of structures using passive tuned mass dampers," *Annu. Rev. Control*, vol. 44, pp. 129–156, 2017, doi: 10.1016/j.arcontrol.2017.09.015.

[7] M. Gutierrez Soto and H. Adeli, "Tuned Mass Dampers," *Arch. Comput. Methods Eng.*, vol. 20, no. 4, pp. 419–431, Dec. 2013, doi: 10.1007/s11831-013-9091-7.

[8] M. C. Smith, "Synthesis of mechanical networks: the inerter," *IEEE Trans. Autom. Control*, vol. 47, no. 10, pp. 1648–1662, Oct. 2002, doi: 10.1109/TAC.2002.803532.

[9] I. F. Lazar, S. A. Neild, and D. J. Wagg, "Inerter-based vibration suppression systems for laterally and base-excited structures," 2014.

[10] L. Marian and A. Giaralis, "Optimal design of a novel tuned mass-damper–inerter (TMDI) passive vibration control configuration for stochastically support-excited structural systems," *Probabilistic Eng. Mech.*, vol. 38, pp. 156–164, Oct. 2014, doi: 10.1016/j.probengmech.2014.03.007.

[11] Y. Hu and M. Z. Q. Chen, "Performance evaluation for inerter-based dynamic vibration absorbers," *Int. J. Mech. Sci.*, vol. 99, pp. 297–307, Aug. 2015, doi: 10.1016/j.ijmecsci.2015.06.003.

[12] D. Lambert, "Vibration Reduction of a Semisubmersible Floating Wind Turbine using Optimized Tuned Mass and Tuned Inerter Dampers".

[13] "Passive structural control of offshore wind turbines", doi: 10.1002/we.426.

[14] Y. Si, H. R. Karimi, and H. Gao, "Modelling and optimization of a passive structural control design for a spar-type floating wind turbine," *Eng. Struct.*, vol. 69, pp. 168–182, Jun. 2014, doi: 10.1016/j.engstruct.2014.03.011.

[15] A. Ahmad, "Load Reduction of Floating Wind Turbines Using Tuned Mass Dampers," *Int. J. Res. Appl. Sci. Eng. Technol.*, vol. 9, no. 9, pp. 1298–1303, Sep. 2021, doi: 10.22214/ijraset.2021.38178.

[16] T. Li, Z. Liu, S. Liu, Y. Fan, Q. Yang, and H. Xiao, "Numerical study on passive structural control of semi-submersible floating wind turbine considering non-collinear wind and waves," *Ocean Eng.*, vol. 266, p. 112745, Dec. 2022, doi: 10.1016/j.oceaneng.2022.112745.

[17] D. Han, W. Wang, X. Li, and X. Su, "Optimization design of multiple tuned mass dampers for semi-submersible floating wind turbine," *Ocean Eng.*, vol. 264, p. 112536, Nov. 2022, doi: 10.1016/j.oceaneng.2022.112536.

[18] "OpenFAST Documentation — OpenFAST v4.1.2 documentation." Accessed: Sep. 07, 2025. [Online]. Available: https://openfast.readthedocs.io/en/main/index.html

[19] J. Jonkman and P. Sclavounos, "Development of Fully Coupled Aeroelastic and Hydrodynamic Models for Offshore Wind Turbines," in *44th AIAA Aerospace Sciences Meeting and Exhibit*, Reno, Nevada: American Institute of Aeronautics and Astronautics, Jan. 2006. doi: 10.2514/6.2006-995.

[20] J. M. Jonkman, "Dynamics of offshore floating wind turbines—model development and verification," *Wind Energy*, vol. 12, no. 5, pp. 459–492, 2009, doi: 10.1002/we.347.

[21] M. A. Lackner and M. A. Rotea, "Structural control of floating wind turbines," *Mechatronics*, vol. 21, no. 4, pp. 704–719, Jun. 2011, doi: 10.1016/j.mechatronics.2010.11.007.

[22] A. Robertson *et al.*, "Definition of the Semisubmersible Floating System for Phase II of OC4," NREL/TP-5000-60601, 1155123, Sep. 2014. doi: 10.2172/1155123.

[23] R. Okuda, "Modeling a Semi-Submersible Floating Offshore Wind Turbine With Tuned Inerter Dampers Within the Platform".

[24] A. J. Goupee, M. J. Fowler, R. W. Kimball, J. Helder, and E.-J. de Ridder, "Additional Wind/Wave Basin Testing of the DeepCwind Semi-Submersible With a Performance-Matched Wind Turbine," doi: 10.1115/OMAE2014-24172.
[25] Z. Zhou, Y. Gao, L. Sun, W. Dong, and Z. Du, "A bistable mechanism with linear negative stiffness and large in-plane lateral stiffness: design, modeling and case studies," *Mech. Sci.*, vol. 11, no. 1, pp. 75–89, Mar. 2020, doi: 10.5194/ms-11-75-2020.
[26] M. Fulei and G. Chen, *Chained Beam-Constraint-Model: One-Page Version*. 2017. doi: 10.13140/RG.2.2.34184.21760.
[27] F. Ma and G. Chen, "Modeling Large Planar Deflections of Flexible Beams in Compliant Mechanisms Using Chained Beam-Constraint-Model1," *J. Mech. Robot.*, vol. 8, no. 021018, Nov. 2015, doi: 10.1115/1.4031028.
[28] N. Wang, J. Zhang, and X. Zhang, "Design of Passive Compliant Constant-Force Mechanism," in *Mechanism and Machine Science*, D. Sen, S. Mohan, and G. K. Ananthasuresh, Eds., Singapore: Springer, 2021, pp. 471–481. doi: 10.1007/978-981-15-4477-4_33.
[29] F. Ma, G. Chen, and H. Wang, "Large-Stroke Constant-Force Mechanisms Utilizing Second Buckling Mode of Flexible Beams: Evaluation Metrics and Design Approach," *J. Mech. Des.*, vol. 142, no. 103303, Apr. 2020, doi: 10.1115/1.4046242.
[30] A. Ahmed *et al.*, "Power capture and power take-off load of a self-balanced dual-flap oscillating surge wave energy converter," *Energy*, vol. 291, p. 130431, Mar. 2024, doi: 10.1016/j.energy.2024.130431.
[31] A. N. Robertson, E. E. Bachynski, S. Gueydon, F. Wendt, P. Schünemann, and J. Jonkman, "Assessment of Experimental Uncertainty for a Floating Wind Semisubmersible Under Hydrodynamic Loading," in *Volume 10: Ocean Renewable Energy*, Madrid, Spain: American Society of Mechanical Engineers, Jun. 2018, p. V010T09A076. doi: 10.1115/OMAE2018-77703.
[32] T. Stehly, P. Duffy, and D. M. Hernando, "Cost of Wind Energy Review: 2024 Edition".
[33] "2024 Cost Components," Tableau Software. Accessed: Sep. 07, 2025. [Online]. Available: https://public.tableau.com/views/2024CostComponents/CostComponents?:embed=y&:toolbar=no&Technology=OffShoreWind&:embed=y&:showVizHome=n&:bootstrapWhenNotified=y&:apiID=handler5
[34] A. Fontanella, G. Colpani, M. De Pascali, S. Muggiasca, and M. Belloli, "Assessing the impact of waves and platform dynamics on floating wind-turbine energy production," *Wind Energy Sci.*, vol. 9, no. 6, pp. 1393–1417, Jun. 2024, doi: 10.5194/wes-9-1393-2024.
[35] X. Li, C. Liang, C.-A. Chen, Q. Xiong, R. G. Parker, and L. Zuo, "Optimum power analysis of a self-reactive wave energy point absorber with mechanically-driven power take-offs," *Energy*, vol. 195, p. 116927, Mar. 2020, doi: 10.1016/j.energy.2020.116927.
[36] L. E. Hall, "Vibration Reduction and Energy Harvesting using Motion-Rectified Tuned Mass-Damper-Inerters in Semi-Submersible Offshore Wind Platforms," Virginia Tech, 2024. Accessed: Sep. 07, 2025. [Online]. Available: https://hdl.handle.net/10919/121076

# 7 Appendix A

## 7.1 Nonlinear Tuned Inerter Damper (TID)

This appendix documents a nonlinear TID concept that combines a tuned secondary mass, damping, and an inerter with a mechanical motion rectifier (MMR) [36]. The MMR converts the absorber's back-and-forth stroke into one-direction shaft rotation so a generator and flywheel can stay spun up between wave cycles, improving the effectiveness of energy harvesting while still providing vibration control. At a high level, the nonlinearity enters through engagement / disengagement logic: the drivetrain connects when the absorber's kinematics can add energy to the shaft and disconnects when it would otherwise sap momentum.

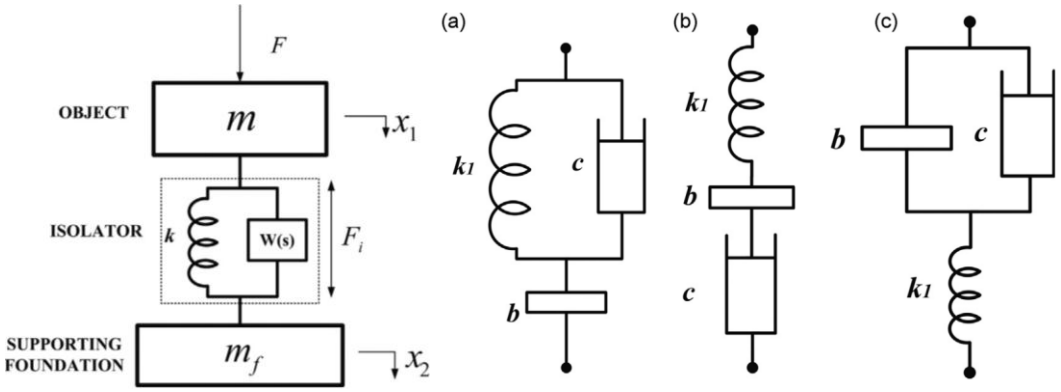


*Figure 68: Mechanism of nonlinear TID with alternative types of inerter-spring-damper (W(s)) layout shown in (a) – (c) [36].*

In the context of a semi-submersible floating wind platform, the nonlinear TID is evaluated against a conventional TMD and a linear TID. The results show that the nonlinear approach yields comparable vibration reduction and energy output to the linear TID for most tuned cases, and that its main advantage may emerge when the "ideal" linear parameters (very soft springs, large stroke) are not physically attainable—for example, due to space limits inside a column or material limits on ultra-low stiffness.

## 7.2 MMR Mechanism and Engagement

The MMR (see **Figure 62**: ) is a passive gearbox (e.g., two opposing one-way clutches driving a bevel-gear train) that rectifies oscillatory input into unidirectional output. In a TID, it allows the generator to maintain rotational speed when the absorber reverses direction, addressing the common loss of kinetic

energy in conventional linear linkages. The study [36] outlines how the MMR can be augmented with engagement criteria so the generator connects only when the instantaneous absorber motion will increase shaft speed; otherwise it disengages to avoid back-driving losses. The same drivetrain can host a flywheel to boost effective inertance and alter damping via electrical loading.

A central—and somewhat counter-intuitive—finding is that when the vibration-reduction objective is optimized, the nonlinear TID tends to be engaged nearly all the time (≈ 93–100% engagement in optimized runs). This implies that, under ideal tuning, the nonlinear device behaves much like a linear TID in practice. The nonlinear pathway therefore becomes most attractive when sub-optimal hardware must be used (e.g., limited stroke or stiffness), because selective engagement can recover some performance that would otherwise be lost.

## 7.3 Models

The full semi-submersible model with three nonlinear TIDs (one per outer column) is developed for frequency- and time-domain evaluations. Irregular wave spectra (JONSWAP) is used to probe behavior across relevant bands; optimization tools include particle swarm and pattern search to minimize heave/pitch response metrics.

The engagement logic is implemented as a piecewise controller that monitors the absorber states and generator speed to determine when coupling the generator increases net rotational energy. The model tracks generator speed, damping force, and electrical power so motion-reduction and energy-harvesting trade-offs are explicit in both the simplified and full systems.

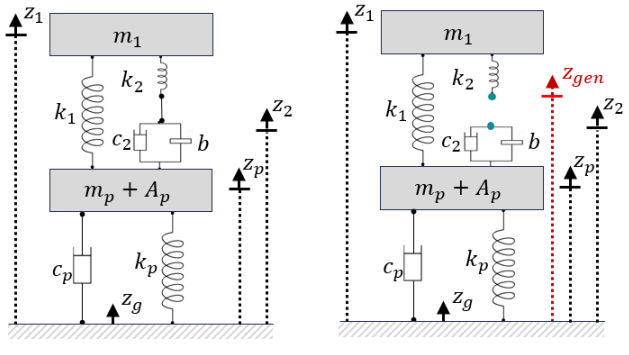


*Figure 69: 2-D concept diagram of a) Linear TID and Engaged Nonlinear TID and b) Disengaged Nonlinear TID within Center Column of Semi-Submersible[36].*

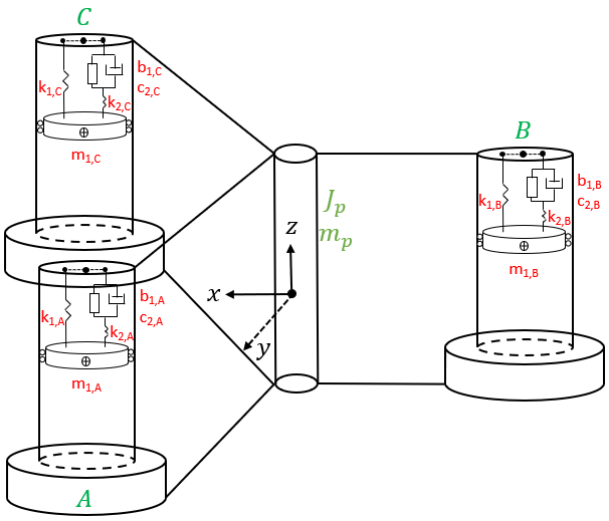


*Figure 70: Full semi-submersible model with three nonlinear TIDs [36].*

## 7.4 Wave Excitation

Irregular sea states in this work are represented with standard ocean wave spectra. Two forms are widely used: the Bretschneider (a modified Pierson–Moskowitz "fully developed sea" spectrum) and JONSWAP (Joint North Sea Wave Project, suited to fetch-limited seas). JONSWAP is typically narrower and more sharply peaked; Bretschneider is broader-band, which is useful when a platform's natural motions span a range around the dominant wave period. For the U.S. Atlantic and Gulf contexts considered here—and to better reflect storm conditions with wider energy spread—we use the Bretschneider spectrum for irregular-wave simulations.

The Bretschneider spectral density $S(\omega)$ is defined by the significant wave height $H_s$ and the peak (or modal) frequency $\omega_m$ (equivalently $T_p = 2\pi/\omega_m$ ). In compact form:

$$S(w) = \frac{5}{16} {H_s}^2 \omega_m{}^4 \omega^{-5} e^{-\frac{5}{4}(\frac{\omega}{\omega_m})^{-4}}$$

where $\omega$ is the radian frequency. This two-parameter model lets us match measured or design sea states with only $H_s$ and $T_p$ while retaining a realistic bandwidth around the spectral peak.

The total excitation force vector from an irregular wave spectrum can be defined as follows:

$$F_{exc} = \Re[R_f(t)\sum_{j=1}^{N} F_{exc}(\omega_j)e^{i(\omega_j t+\phi_j)}\sqrt{2S(\omega_j)d\omega_j}],$$

Where $S(\omega_j)$ is the Bretschneider spectrum corresponding to the chosen frequency range, $F_{exc}(\omega_j)$ represents the wave excitation at a particular frequency, and $\phi_j$ represents a randomized phase.

## 7.5 Key Results

On the full platform with three nonlinear TIDs (mass ratio example $\mu \approx$ 3% total), optimization has been conducted directly using the irregular wave excitation model. **Figure 71**: shows the frequency domain results from a heave-reduction focused optimization run with genetic algorithm, where both pitch and heave were slightly reduced from their baseline state using the linear and nonlinear TID. The optimized parameters are shown in **Table 8**. Optimization directly on this dataset resulted in tuning of the three vibration absorbers to the wave frequency rather than the natural frequency of the platform.

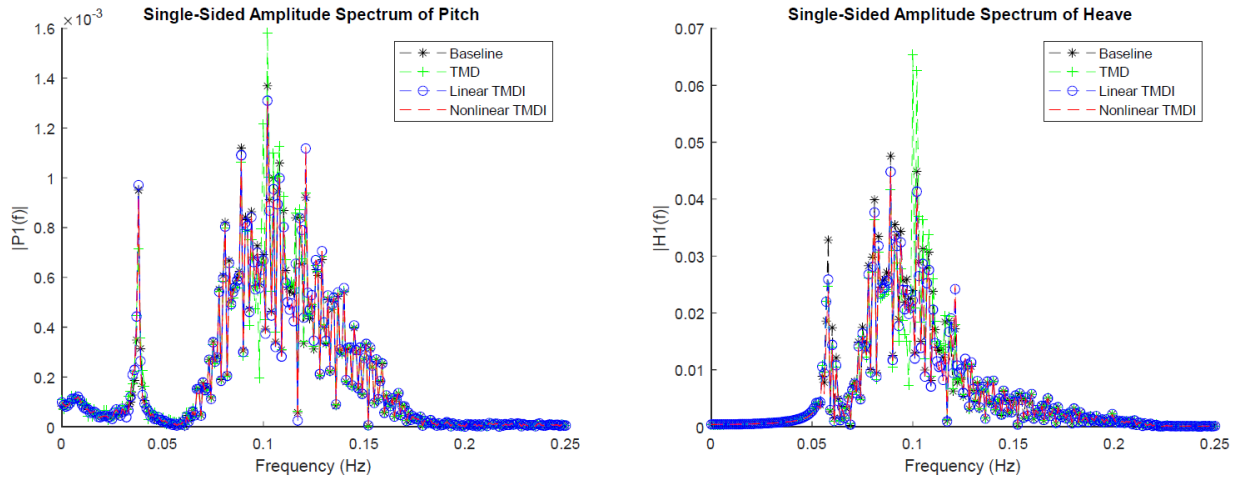


*Figure 71: Frequency domain plot for irregular wave (10 s period) with vibration damper tuned to wave frequency [36].*

*Table 8: Final optimized parameters of full model optimized using irregular wave and mass ratio = 3% [36].*

| | | $\alpha_1$ | $\alpha_2$ | $\xi$ | $\mu_2$ | $f_1$ (Hz) | $f_2$ (Hz) | $H_2$ % Reduction | | $H_{inf}$ % Reduction | |
|---|---|---|---|---|---|---|---|---|---|---|---|
| | | | | | | | | Pitch | Heave | Pitch | Heave |
| *Optimized for Heave* | TMD | 1.76 | - | 0% | 0% | 0.099 | - | 0% | 0% | -15% | -37% |
| | TMDI without MMR | 1.76 | 6.62 | 2053% | 3% | 0.099 | 0.371 | 1% | 5% | 4% | 6% |
| | TMDI with MMR | 1.76 | 6.62 | 2190% | 3% | 0.099 | 0.371 | 1% | 6% | 4% | 5% |

**Figure 55** depicts the change in power with time for each of the three TIDs. The average total power between the three TIDs at the optimized conditions is 5.15 kW for the linear system and 6.59 kW for the nonlinear system. This does show an improvement between the linear and nonlinear design, but also indicates that power production from the TID systems may be very minimal compared to that of the turbine itself at the optimized parameters for motion reduction and much less than that from a similarly sized point absorber.